

DARK SPOT DETECTION FOR CHARACTERIZATION OF OIL SPILLS USING POLSAR REMOTE SENSING

ANURAG KULSHRESTHA

March, 2018

SUPERVISORS:

Mr. Shashi Kumar

Dr. ir. Wietske Bijker



DARK SPOT DETECTION FOR CHARACTERIZATION OF OIL SPILLS USING POLSAR REMOTE SENSING

ANURAG KULSHRESTHA

Enschede, The Netherlands, March, 2018

Thesis submitted to the Faculty of Geo-Information Science and Earth Observation of the University of Twente in partial fulfilment of the requirements for the degree of Master of Science in Geo-information Science and Earth Observation.

Specialization: Geoinformatics

SUPERVISORS:

Mr. Shashi Kumar

Dr. ir. Wietske Bijker

THESIS ASSESSMENT BOARD:

Dr. ir. R.A. de By (Chair)

Prof. Dr. ir. A. Stein (ITC Professor)

Dr. Anup Das (External Examiner, Space Application Centre (SAC), Ahmedabad)

DISCLAIMER

This document describes work undertaken as part of a programme of study at the Faculty of Geo-Information Science and Earth Observation of the University of Twente. All views and opinions expressed therein remain the sole responsibility of the author, and do not necessarily represent those of the Faculty.

ABSTRACT

Oil spills have been a cause of concern for environmental agencies, governments and coastal habitats. Accurate and fast knowledge about the location and characteristics of oil spills is extremely useful for oil spill containment and clean-up operations. In this research, the potential of polarimetric SAR data in detecting and characterizing oil spills is studied. The study is conducted using quad-polarized UAVSAR data, hybrid polarized RISAT-1 data and dual-polarized TerraSAR-X data of an experimental oil spill exercise (NORSE-2015) in North Sea, Norway conducted on 10th June, 2015. The environmental conditions during the oil spill exercise were rough with wind speed being consistently above 10 m/s. In this exercise, four different type of oils were spilled into the sea: a simulated plant oil (PO), and three emulsions of mineral oil with 40% oil (E40), 60% oil (E60), and 80% oil (E80) respectively with water making up the remaining volume in each emulsion. Distinguishing between different type of oil slicks and from similar look-alikes is difficult due to the similarity of their radar backscatter signals. To overcome this challenge, polarimetric SAR data is used to derive the polarimetric parameters which relate to the physical properties of the scatterers on the sea surface. Some of these features are used to detect oil spills using Expectation Maximization of Gaussian Mixture Models. The parameters of the algorithm are optimized using the UAVSAR dataset and hence the method is tested on all available datasets. The method is found to show better performance for RISAT-1 dataset as compared to TerraSAR-X dataset. The strongest factor for incorrect results is found to be the high sea waves caused due to high wind speeds. The shadows created by the high surface gravity waves act as look alikes. The slick areas extracted using this process help in realizing that the stretching of the mineral oil slicks is in the direction of wind and its extent is also proportional to the amount of oil in the slicks. The extracted slick areas are then used to compare the polarimetric features on the basis of their potential to separate oil slicks from water and from other oil slicks. The determinant of the covariance matrix is found to be the most effective feature for oil-water and oil-oil class separabilities. Therefore, a covariance matrix based Wishart-maximum likelihood classifier (W-MLC) is chosen for oil spill classification. The results of this classification are found to be much better than Gaussian based MLC, with no misclassification in the near range and a gain in overall classification accuracy of 16-34%. The oil probability output from this classification is then used to model oil spills as Gaussian probability surface models. Some of the probability surfaces models are found to correctly estimate the orientation and areal extent of the spill. Moreover, this method is also able to probabilistically separate E40 from E60 from each other by correctly estimating relative peak probability for E60 as compared to E40. This method gave higher probability for PO, thereby indicating low mixing of PO with the sea water. It is concluded that probabilistic surface modelling is useful in oil spill categorization and therefore, can be optimised to include other ancillary information to further improve the quality of oil spill classification.

Keywords: Synthetic Aperture Radar, Image Classification, UAVSAR, Gaussian Mixture Model, Wishart Classification, Probability Surface

ACKNOWLEDGEMENTS

I would like to take this opportunity to thank my parents for their greatest gift of life to me. They have been, and always will be a constant source of inspiration for me throughout my life. I would like to thank my whole family who have supported me emotionally and financially during the course of this M.Sc. I thank all my friends who helped me with their insights and were always there for me whenever I needed them.

According to famous proverb in Hinduism: “Matha Pitha Guru Deivam”, the Guru or teacher, is the next most important person in an individual’s life, more notably, even more important than God. I want to thank all my teachers, right from my childhood, who have given the incredible gift of knowledge to me. During this M.Sc., it has been an honour for me to be guided by such amazing teachers as Dr. Wietske Bijker and Mr. Shashi Kumar. Dr. Wietske has been instrumental in helping me inculcate the habit of scientifically analysing the results from my experiments. Her opinion on every aspect of this M.Sc. research was vital for me. She has also encouraged me to never give up the will to learn something new and useful. It was indeed very lucky for me to have her as my supervisor. I would like to thank Dr. Wietske for her guidance during my M.Sc. Research. Mr. Shashi Kumar brought a calming influence during the course of my M.Sc. His motivation to keep trying new experiments with the datasets was extremely helpful. Moreover, his insights on the results were very useful. His push towards hard work was vital for this research. Therefore, I would like to thank him for being a guiding light in my M.Sc.

I want to extend my gratitude to the M.Sc. course co-ordinators, Dr. Sameer Saran and Dr. Valentyn Tolpekin for their constant help throughout this period. Moreover, I would like to thank the organizers and teachers both at IIRS and ITC involved in this amazing programme. It was an honour for me to have reaped the benefits of such an old partnership between the two reputed institutes, IIRS and ITC, and the two countries: India and Netherlands.

A very special vote of thanks goes to DLR, NASA-JPL and KSAT for providing TerraSAR-X, UAVSAR, and RISAT-1 datasets for this M.Sc. Research work.

I would like to acknowledge the open source community which has been responsible for developing free open source softwares, programming languages and libraries. I would especially like to thank everyone responsible for the development of Ubuntu, Linux Foundation, Python, R, Mendeley, PolSAR-Pro, SNAP, QGIS and LibreOffice.

TABLE OF CONTENTS

List of Figures.....	iv
List of Table.....	v
1. Introduction.....	1
1.1. Motivation and Problem Statement.....	1
1.2. Research Identification.....	4
1.3. Project Workflow.....	5
1.4. Thesis Outline.....	6
2. Literature Review on SAR for Oil Spill Detection.....	7
2.1. Nature of surface waves on water surface.....	7
2.2. Oil spills over the sea surface.....	8
2.3. Interaction of radar waves with ocean surface.....	9
2.4. Oil spill detection and characterization using SAR images.....	13
3. Study Area and Datasets.....	17
3.1. NORSE-2015.....	17
3.2. SAR dataset Description.....	20
4. Methodology.....	25
4.1. Data Extraction.....	26
4.2. Scattering mechanism of sea surface.....	27
4.3. Preprocessing.....	28
4.4. Feature Extraction.....	29
4.5. Dark Spot detection.....	31
4.6. Slick analysis and Feature Comparison.....	32
4.7. Oil Spill Classification.....	33
4.8. Probability Surface Modelling.....	35
5. Results And Analysis.....	37
5.1. Scattering mechanism of sea surface.....	37
5.2. Preprocessing.....	39
5.3. Feature Extraction.....	40
5.4. Dark Spot detection.....	40
5.5. Slick analysis and Feature Comparison.....	44
5.6. Oil Spill Classification.....	48
5.7. Probability Surface Modelling.....	49
6. Discussion.....	53
7. Conclusion And Recommendations.....	57
List Of References.....	61
Appendix-A.....	67
Appendix-B.....	69
Appendix-C.....	75

LIST OF FIGURES

Figure 1: Phase velocity of gravity and capillary waves over sea and ocean surfaces.....	8
Figure 2: Geometry of Radar waves and sea surface.....	11
Figure 3: Location of the study area: Frigg oil Field in North Sea.....	17
Figure 4: Depiction of flight acquisition geometry.....	18
Figure 5: Intensity VV images of UAVSAR.....	21
Figure 6: Histograms showing data distribution of UAVSAR, TerraSAR-X and RISAT-1.....	23
Figure 7: Methodological Flow Diagram.....	25
Figure 8: VV intensity images of multi-looked and single-look images of study area.....	26
Figure 9: Training data for classes: Oil and Water.....	33
Figure 10: Pauli Decomposition: RGB composite	38
Figure 11: Freeman decomposition of UAVSAR dataset.....	38
Figure 12: RGB composites from m-chi (a), m-alpha (b), m-delta (c) decomposition of RISAT-1.....	39
Figure 13: Incidence angle normalization.....	40
Figure 14: Histogram of UAVSAR polarimetric features.....	41
Figure 15: Segmented outputs for number of classes = 2 (left column) and classes = 3.....	42
Figure 16: Slick segmentation: The results of slick segmentation on the UAVSAR features (λ_3 and PD).....	44
Figure 17: Oil slicks and 3 other water regions used for comparison and feature selection.....	45
Figure 18: Mean and variance of features for oil slicks.....	46
Figure 19: Class separability between oil slicks and open water regions.....	47
Figure 20: Jeffries-Matusita distance between W_{mid} and (a) PO, (b) E40, (c) E60 and (d) E80	47
Figure 21: Gaussian-MLC (1st row) and Wishart MLC (2nd row).....	48
Figure 22: Probability Surface of probability for oil class from W-MLC classification.....	49
Figure 23: Oil slick masks and oil probability used to used for Gaussian surface Fitting (window size:.....	49
Figure 24: Contour plots depicting the regions of Gaussian models.....	51

LIST OF TABLES

Table 1: Brief details about a few of currently operational space-borne and air-borne SAR sensor platforms...	3
Table 2: Description of the experimental oil spills in NORSE2015.....	19
Table 3: List of SAR datasets acquired during NORSE-2015.....	19
Table 4: Relevant physical properties of components used in oil emulsions.....	19
Table 5: MetOcean data of Frigg Oil Field on 10th June, 2015.....	20
Table 6: Metadata of UAVSAR, RISAT-1 and TerraSAR-X datasets.....	22
Table 7: Fully Polarimetric Features extracted from UAVSAR data.	30
Table 8: Hybrid polarimetric features extracted using RISAT-1 data.....	31
Table 9: Input parameters for EPFS segmentation of UAVSAR, RISAT-1 and TerraSAR-X datasets.....	32
Table 10: Input parameter values for Wishart Classification of UAVSAR dataset.....	35
Table 11: UAVSAR, RISAT-1 and TerraSAR-X polarimetric features with contrast between and water.....	40
Table 12: Results from Shapiro-Wilk test of normality for the linear UAVSAR polarimetric features.....	41
Table 13: Shape, drift, size and extent of slicks.....	45
Table 14: Parameters of Gaussian surface fitting.....	50

1. INTRODUCTION

1.1. Motivation and Problem Statement

Oil spill is an accidental release of mineral oil in a water body from offshore drilling rigs, oil tankers or underwater oil pipelines. After getting introduced into the water, oil usually forms a thin film over the water surface which is referred to as oil spill, marine surface slick or oil slick. However, oil slicks can also be present as thick layers on the water surface as oil-water emulsions which seldom sink down to the sea bed (Dell'Amore, 2015). The oil slicks move both horizontally over the water surface and vertically inside the water. Wind and surface water current are the two major factors responsible for the spread of oil over the water surface. There are several factors which influence the oil spill impact on the environment. Amongst all of them, the crucial ones are its rate of motion, its direction of movement, its location relative to human and marine species habitats, its type and its extent over the ocean surface.

Oil spills cause many harmful consequences for the marine and coastal ecosystems (Chang, Stone, Demes, & Piscitelli, 2014). One of the most well-known oil spill event in recent history was the Deepwater Horizon oil spill in 2010. It resulted in 4.9 million barrels of oil getting spilt in the Gulf of Mexico over a period of 5 months (Weber, 2010). It caused a huge impact on the living flora and fauna of the gulf (Beyer, Trannum, Bakke, Hodson, & Collier, 2016). Many animals, including birds, sea turtles, mammals and fishes died as a result of this oil spill (CNN, 2010). It also impacted on the lives of people living along the coast by hampering tourism and fishing industries of the region. Therefore, it is necessary to anticipate and prepare for oil spills to limit their adverse consequences on the environment. To curtail the impact of an oil spill, it is important to identify its location and to characterize it (i.e. to distinguish it from similar look-alike features, e.g. marine algae) as accurately as possible. Early and accurate detection ensures quick and targeted response to the affected location. It also helps in efficient allocation of relief efforts and resources. Moreover, having knowledge about the type of spilled oil assists decision makers in choosing the appropriate method for oil spill clean-up. Therefore, there is a demand of efficient and reliable methods for accurate detection and characterization of oil spills.

Remote Sensing is one of the most efficient and widely used methods in oil spill detection (Fingas & Brown, 2014). Passive Remote Sensing methods exploit the optical properties of oil such as relative reflectance and relative absorbance to distinguish it from water. In the electromagnetic spectrum, there are various bands in which oil spill remote sensing can be performed: visible range (Wang, Pan, Zhan, & Zhu, 2010), infrared (IR) range (Pinel & Bourlier, 2009), near infrared (NIR) range (Bulgarelli & Djavidnia, 2012), and ultraviolet (UV) range. However, reflectance based passive remote sensing methods are limited due to atmospheric conditions (e.g. clouds) and their requirement of an external source of illumination. In case of emittance based thermal IR remote sensing, only thick oil spills which accumulate more heat can be detected.

Active Remote Sensing sensors such as Synthetic Aperture Radar (SAR) provide an alternate to passive remote sensors and overcome their limitations. SAR sensors are independent of the sun to collect imagery, and hence also work during night. Moreover, SAR can provide images in all-weather conditions because of the capability of radar waves to penetrate through clouds. Therefore, SAR remote sensing is one of the most commonly used methods for detecting and characterizing oil spills (Fingas & Brown, 2014). SAR remote sensing is based on the interaction of electromagnetic radar waves with sea surface matter waves. Ocean or sea surfaces are characterized by two types of waves: capillary waves and gravity waves. Capillary

waves, also termed as ripples, are short wavelength waves which are formed due to the interaction of water surface and wind. These waves are sensitive to the surface tension and density of the fluid surface. Gravity waves are longer in wavelength and are mostly influenced by the effects of fluid inertia and gravity. A slick cover causes damping of small capillary waves due a reduction in surface tension and decrease in wind friction. This causes a suppression in wave growth and an increase in wave dissipation (Minchew, Jones, & Holt, 2012). Therefore, oil slicks mostly appear darker than the wind-roughened surrounding ocean in the acquired SAR imagery.

In spite of all the advantages which SAR remote sensing offers in detecting oil spills, there are various limitations associated with this technique. These limitations include false target detections such as low wind areas, marine biogenic slicks, rainfall footprints (Alpers, Zhang, Mouche, Zeng, & Wai, 2016), and ship wakes. Marine biogenic slicks behave in a very similar way as mineral oil spills. They also cause damping of capillary waves resulting in reduction of radar backscatter. These natural slicks are mostly caused due to the presence of algae, biogenic oils, glacial flour, and fish sperms (Gens, 2008). Therefore, detection of mineral oil spills using radar is difficult in areas where the probability of occurrence of aforementioned false targets is high (Liu, Zhao, Li, He, & Pichel, 2010). Polarimetric SAR (Pol-SAR) data has been reported to aid in accurate oil slick detection and in distinguishing between biogenic and mineral oil spills (Gade, Alpers, Hühnerfuss, Masuko, & Kobayashi, 1998).

A linear multi-polarized SAR dataset contains data in multiple transmitted-received combinations or channels. For instance a dual polarized (dual-pol.) dataset contains a co-polarized channel (either vertically transmitted and vertically received (VV) or horizontally transmitted and horizontally received (HH)) and a cross-polarized channel (VH or HV). Similarly, a quad-polarized (quad-pol) dataset contains four channels i.e. two co-polarized channels VV, HH, and two cross polarized channels VH and HV (Van Zyl & Kim, 2011). Most airborne and space-borne radar sensors, operating at a particular frequency, are either dual-pol or quad-pol. However, compact polarimetric or hybrid polarimetric channels are also used in SAR remote sensing. These sensors transmit circularly polarized light and receive linear component of the received signal (Raney, 2007). Table 1 summarizes 5 of many radar sensors which are currently used for remote sensing. An increase in the number of polarization channels (e.g. from dual-pol to quad-pol) or variation between linear and circularly polarized channels of SAR datasets increases the number of polarimetric features which can be extracted from the datasets. Use of polarimetric data in ocean monitoring is based on Bragg's scattering theory (Valenzuela, 1978). The backscatter response from the sea surface waves depends upon the local incidence angle, wavelength of radar waves, wavelength of surface waves, the dielectric constant of the surface material and nature of polarization of incident electromagnetic radar wave. Polarimetric data is used to extract certain polarimetric features which are related to the factors in Bragg scattering theory. Some of the polarimetric features which have been reported to be very useful in improving oil spill detection (Espeseth et al., 2017) are co and cross polarization ratio which helps in estimating the orientation of a sea surface waves (Minchew et al., 2012), determinant of sample covariance matrix, entropy (H), anisotropy (A) and angle (α) between the eigenvectors of coherency matrix. Polarimetric target decompositions such as H/A/ α decomposition make use of quad-pol data and have been reported to be useful in detecting oil spills (Skrunes, Brekke, Jones, & Holt, 2016).

Table 1: Brief details about a few of currently operational space-borne and air-borne SAR sensor platforms

Name	Type	Frequency band	Polarization
RADARSAT-2	Spacebourne	C band	Quad-pol.
Sentinel-1	Spacebourne	C band	Dual-pol.
RISAT-1	Spacebourne	C band	Hybrid Polarized (RH, RV)
TerraSAR-X	Spacebourne	X-band	Dual-pol., Quad-pol.
UAVSAR	Airbourne	L-band	Quad-pol.

Speckle noise is a common phenomenon in SAR datasets where coherent waves from scatterers from the same resolution cell interact constructively or destructively (Goodman, 1976). This results in extremely high or low magnitude of radar backscatter in each of the respective cases. Sea surface waves over the oil slick are dampened due to the presence of oil. The reduced backscatter from the scatterers over the slick would result in reduced incidents of constructive and destructive interference. Therefore, more speckle would be observed over open water as compared to oil slicks. Generally, for most applications, speckle noise is filtered out using adaptive or non adaptive speckle filtering algorithms. However, speckle noise could be used as a source of information to characterize oil spills.

There are various segmentation and classification algorithms which make use of polarimetric and contextual features to detect oil spills. Segmentation of oil slicks has been reported using a threshold based approach in Migliaccio, Gambardella, & Tranfaglia (2007). The choice of the threshold value is dependent upon the nature of surface films and the state of the sea at the time of data acquisition. More complex multi-stage unsupervised segmentation algorithms have also been reported to delineate oil spills (Espeseth et al., 2017). There are many classification methods which can be used to classify oil spills. They include Maximum Likelihood Classification (MLC), Support Vector Machine (SVM), and Markov Random Fields (MRF) based classifications. Moreover, PolSAR classification methods, such as Wishart classification have also been used in detecting oil spills (Kumar, Kattamuri, & Agarwal, 2016). MRF based soft classification methods can also be used to classify oil-slicks. The probability of true oil spill detection from SAR data is affected by multiple factors, such as wind speed range, presence of algae in the region, proximity to shipping routes and oil rigs and shape of the slick. These effects are usually represented in a set of different hard classified maps. As an alternative, the factors stated above can be captured by modelling of oil spills as probability surfaces over the 2 dimensional sea surface.

This research uses polarimetric features derived from quad-polarized Uninhabited Aerial Vehicle Synthetic Aperture Radar (UAVSAR), dual polarized TerraSAR-X and hybrid polarized RISAT-1 data from an experimental oil spill exercise called NORSE-2015, to detect and characterize oil spills. For this purpose, this research uses MLC and Wishart classification methods and compare their performance of the basis their accuracy in classifying oil spills. Furthermore, this research models oil spills as probability surfaces using 2-D Gaussian models.

1.2. Research Identification

The overall focus of this research is to detect different categories of oil from open water by using polarimetric features derived from quad-polarized, dual-polarized and hybrid polarized SAR data, to assess the separability of slicks from water, characterize oil slicks, and model them as probability surfaces.

1.2.1. Research Objectives

The main objective of this work is to investigate contextual and multi-polarimetric information for the detection and characterization of oil spills from near co-incident quad-polarized L-band UAVSAR data, hybrid polarized C-band RISAT-1 data and dual polarized X-band TerraSAR-X data and model oil spills as probability surfaces. This objective can be subdivided into 4 further specific-objectives. They are,

- 1) Review and study contextual features, polarimetric features, Pol-SAR segmentation and classification methods used to detect and classify oil spills.
- 2) Segment oil slicks regions of interest (ROI) from water.
- 3) Analyse slicks and compare polarimetric features on the basis of their capability to distinguish oil spills from water, and also distinguish between different oil spills.
- 4) Apply image classification methods to characterize oil slicks and hence, use 2D Gaussian models to model oil slicks as probability surfaces.

1.2.2. Research Questions

Referring to the research objectives, the following research questions are addressed.

1. Specific objective 1:
 - a. Which contextual and polarimetric features derived from quad-pol datasets have been used in the identification of oil spills?
 - b. Which segmentation and classification methods have been used to detect and classify oil spills?
 - c. What limitations are imposed on oil-spill detection using SAR due to sensor characteristics and environmental conditions?
2. Specific objective 2:
 - a. How can contextual and polarimetric features be used to segment oil spills?
 - b. How can SAR speckle be used in the identification of oil spills?
3. Specific objective 3:
 - a. Which measure of separability is most appropriate for comparing the ability of polarimetric and contextual features to distinguish oil spills?
 - b. Which polarimetric and contextual features are best suited for detecting oil spills?
4. Specific objective 4:
 - a. What are the statistical characteristics of polarimetric features?
 - b. What are the limitations on the type of classification algorithms that can be applied to the features?
 - c. How can oil spills be modelled as probability surfaces?

1.2.3. Innovation

This research attempts to use polarimetric information from SAR data to detect and improve characterization of oil slicks from open water by using Wishart classification. Moreover, the effect of wind on the movement of slicks is studied and found to be in agreement with an existing hypothesis that mineral oils move more rapidly in the direction of wind as compared to natural biogenic oils (Alpers, Holt, & Zeng, 2017). Their extent of movement from the source of the oil spill is also found to be in proportion to the amount of oil in the oil emulsions. Shadows in radar backscatter are identified as false look-alikes in the study area, where the environmental conditions were rough and the wind speed was consistently high. This research also attempts to model oil spills using two dimensional Gaussian surface models. This method was an application of the method used by Ardila (2012), who used this method for modelling the extent of tree crowns in urban areas.

1.3. Project Workflow

This research focuses on using quad-polarized L band UAVSAR, C-band RISAT-1 and X-band TerraSAR-X dataset to detect and characterize marine surface slicks. A thorough literature review precedes the data processing steps. Knowledge about relevant algorithms for feature extraction, feature selection and data classification are acquired through this review. Moreover, the met-ocean data about the prevailing environmental conditions is used for the analysis (Jones et al., 2016). All the methods have been applied on the UAVSAR dataset and few of the methods are tested on RISAT-1 and TerraSAR-X datasets. UAVSAR multi look complex (MLC) dataset, which contains the elements of the covariance matrix, has been used for the analysis, whereas single look complex (SLC) datasets of RISAT-1 and TerraSAR-X have been used.. The unit of the UAVSAR pixel values is linear amplitude. The dataset is preprocessed to correct for the incidence angle effect in the elements of the covariance matrix (Espeseth et al., 2017).

The contextual features are extracted using grey-level covariance matrix GLCM method (Lopez & Moctezuma, 2005). Polarimetric features, as reported in Espeseth et al. (2017) and Kumar et al. (2016), are extracted from the datasets using the SAR polarimetric channels. Some of the extracted features are co-polarization power ratio, cross polarization ratio, geometric intensity, entropy, mean angle of eigenvectors from coherency matrix, and anisotropy. Image segmentation is applied in order to delineate the oil-water boundary. Oil slicks are segmented using “extended polarimetric feature space” (EPFS) unsupervised segmentation method (Espeseth et al., 2017). The segmented results from this procedure are used to select the suitable features using the feature selection method. The segmented ROI also serve as a sources of training data to the classifiers. Furthermore, this method is used in understanding the evolution of oil spills using the 22 multi-temporal UAVSAR datasets.

The extracted contextual and polarimetric features are compared on the basis of their ability to distinguish between the segmented oil slicks and water. The comparison is based on a class separability measure called Jeffries-Matusita (JM) distance. The JM class separability measure assumes data to be normally distributed. The features which provide the best separability between oil slicks and water regions are chosen for further analysis. The best chosen features are used for classifying four oil spill classes and open water using pixel based classification methods. The soft classification output contains the probabilities of each of the classes for each pixel.

After a satisfactory classification is achieved, probability surface modelling of oil spills is performed using Gaussian surface fitting of oil probability result from best chosen classification method after accuracy assessment. This output is used to create two dimensional probability surfaces by using oil class probabilities for each pixel. This final output serves as a more feasible way of visualizing oil spills as compared to hard classified outputs. This method captures the variation in oil probabilities of four oil slicks.

1.4. Thesis Outline

This thesis consists of six chapters. Chapter 1 introduces the motivation, problem statement, research objective, and research questions. Chapter 2 provides the theoretical background of the research. Chapter 3 gives a detailed description of the study area and datasets used in this study. Chapter 4 states the methodology used to achieve the research objectives. Chapter 5 describes and analyses the results achieved after executing the methods described in the previous chapter. Chapter 6 presents a discussion on the results from the previous chapter. Chapter 7 concludes the research with answers to research questions, a note on the novelty of the research, and further recommendations.

2. LITERATURE REVIEW ON SAR FOR OIL SPILL DETECTION

This chapter summarises the theoretical background on the use of radar for monitoring the ocean surface for detecting oil spills. It starts with a discussion on the nature of sea surface waves and the impact of oil on the sea surface waves. The next section discusses the interaction of radar waves with the sea surface and how radar data able to capture the change in the sea surface properties due to the presence of oil. The next section focuses on the radar data analysis and methods for oil spill detection and classification.

2.1. Nature of surface waves on water surface

The ocean surface is characterised by two types of waves. The long wavelength gravity waves and superimposed capillary waves (Minchew et al., 2012). These waves are caused due to the roughness caused by the air-sea interaction. The friction between the wind and the sea surface causes a transfer of energy from the wind waves to the sea surface waves. This results in the formation of short waves on the sea surface of the order of centimetres (Kanevsky, 2009). Some part of this transferred energy is transmitted to the longer gravity waves. The formation of larger waves keeps going on until a balance is reached between the energy imparted by winds and the energy dissipated due to wave breaking, turbulence and viscosity (Phillips, 1957).

The general expression for the dispersion relation for the surface waves at the interface of two fluids is described by Equation (2.1); where ω is the angular frequency, g is the acceleration due to gravity, k is the wavenumber of surface waves, ρ and ρ' ($\rho > \rho'$) are the mass densities of the heavier and lighter fluid respectively and σ is the surface tension (Longuet-Higgins, 1963). In case of air-sea surface interaction, where ($\rho \gg \rho'$), where ρ is the density of sea water, Equation (2.1) reduces to Equation (2.2) which is the general expression for the dispersion relation of gravity-capillary waves.

$$\omega^2 = |k| \left(\frac{\rho - \rho'}{\rho + \rho'} g + \frac{\sigma}{\rho + \rho'} k^2 \right) \quad (2.1)$$

$$\omega^2 = gk + \frac{\sigma}{\rho} k^3 \quad (2.2)$$

The small wavelength waves described above are termed as capillary waves or quite often as ripples whereas the waves which are longer in wavelength are called gravity waves. At the limit of small wavelength, the dispersion relation is $\omega = \sqrt{(\sigma/\rho)} k^{3/2}$, and that for long wavelengths, reduces to $\omega = \sqrt{gk}$ (Landau & Lifshitz, 1987). The phase velocity (c) of the surface wave is given by Equation (2.3).

$$c = \frac{\omega}{k} = \sqrt{\frac{g}{k} + \frac{\sigma}{\rho} k} \quad (2.3)$$

The plot of phase velocity of gravity and capillary waves for water and oil as the surface material can be visualized in Figure 1.

2.2. Oil spills over the sea surface

The roughness of the sea surface is influenced by various internal and external factors. Some of the internal factors are the motion of internal waves under the surface of the sea and eddy currents (Kanevsky, 2009). It is also interesting to notice the external effects which cause changes in the sea surface. They include spillage of mineral oil spills, development of biogenic oil films, sea up-welling, wind velocity, temperature, movement of objects (such as ships) over the surface, etc. (Alpers et al., 2017). Owing to their low density, oil spills and other surface films generally form a film over the sea surface. The presence of oil over the sea surface changes the geometrical and physical properties of the surface.

The properties of the sea surface change in the presence of surface films over it. This is because of the change in the surface tension, density and viscosity of the fluid present at the surface. If the thickness of the surface film is large, it also changes the dielectric constant of the sea surface, which impacts the backscatter of the radar waves from such locations. This change in the surface tension and density of the surface causes the capillary waves to dampen (Equation 2.2) and therefore, the surface roughness decreases. The relative density and relative surface tension of mineral oil with respect to water are in the approximate ranges of 0.8 – 0.9 and 0.35 – 0.5 respectively (Harvey, 1925).

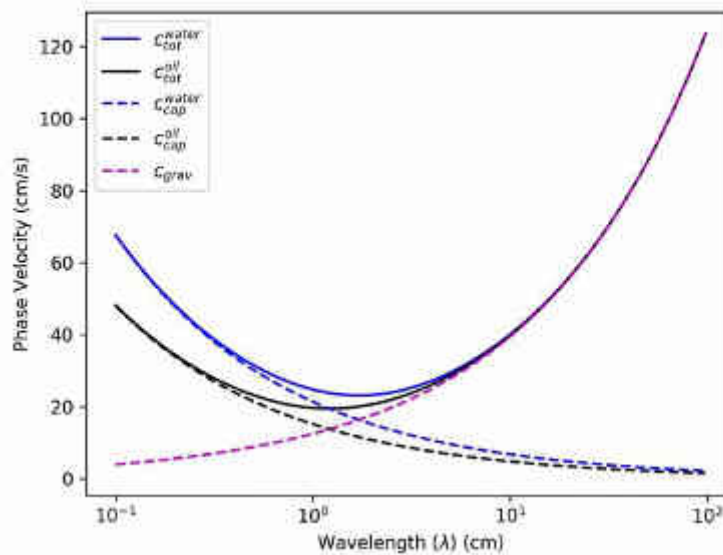


Figure 1: Phase velocity of gravity and capillary waves over sea and ocean surfaces. The total phase velocity of water with $\rho = 1\text{g/cm}^3$ and $\sigma=72.8$ dynes/cm is represented by solid blue line, and that of oil with $\rho = 0.9\text{g/cm}^3$ and $\sigma = 33$ dynes/cm is shown by solid black line. The long gravity waves, which are not affected by change in surface tension is represented by dashed magenta line. The dashed blue and black lines show the phase velocities of capillary waves for water and oil respectively (Minchew et al., 2012).

The large gravity waves theoretically do not change their behaviour in the presence of surface slicks (Equation 2.2). This dependence of the gravity-capillary waves on the type of fluid can be visualised in Figure 1 where the phase velocity of the surface waves are plotted against the wavelength (Equation 2.3). However, there have been evidences that the presence of surface films also affect the large gravity waves. This change in the large wavelength ocean wave spectrum is caused directly due to the surface tension gradients (Marangoni effect) and indirectly due to non-linear wave-wave interactions (Alpers & Hühnerfuss, 1989; Gade, Alpers, Hühnerfuss, Masuko, et al., 1998; Gade, Alpers, Hühnerfuss, Wisman, & Lange, 1998). Another reason for damping of the sea surface waves is viscous damping. The kinematic viscosity of mineral oils are much higher than that of water. The variation in the thickness and chemical composition of surface slicks can result in varying kinematic viscosity across the slick film. The viscous damping is directly proportional to the wavelength of the surface wave. A theoretical investigation of the damping of short surface gravity-capillary waves, performed by Jenkins & Dysthe, (1997) and Jenkins & Jacobs, (1998) revealed that thin oil spills cause damping of short scale capillary waves. However, for thick oil slicks, kinematic viscosity of oil majorly affects this damping.

Oil spills over the sea surface constantly undergo weathering which includes physical, chemical and biological processes. They include, evaporation, dissolution, emulsification, oxidation, bio-degradation and dispersion. With the passage of time, a surface slick evaporates and thereby changes the density and viscosity of the oil slick on the surface (Brebba, 2001). Oil also has a property to form emulsions with water. The density and viscosity of oil increases with increasing proportion of oil in the emulsion. Moreover, the oil spills disperse over time due to the film's interaction with turbulent waves which break the spill into multiple smaller oil slicks (Skrunes, Brekke, & Eltoft, 2014).

A big challenge in the application of radar remote sensing of oil spills is the fact that multiple look-alike features on the sea surface give similar backscatter as oil spills. They include natural biogenic films, low wind areas, upwelling of cold water from the depths of the sea, ship wakes, rainfall areas, amorphous ice present over the sea surface, discharge of waste-water from sewage plants, floating micro and macro algae, plant oil spilt on the sea during oil tanker cleaning, fish oil and fish sperms, etc. (Alpers et al., 2017; Fingas & Brown, 2014; Gens, 2008). Therefore, it is difficult to separate mineral oil spills from natural biogenic slicks and other look-alike features (Brekke & Solberg, 2005).

In order to develop an efficient methodology for oil slick characterization it is important to understand the basics of light-matter interaction, in the paradigm of sea surface waves and microwave electromagnetic waves. This is briefly explained in the next section.

2.3. Interaction of radar waves with ocean surface

2.3.1. Factors responsible for radar backscatter from rough surfaces

The backscatter of the radar waves from the objects on the ground is dependent on the geometrical and physical properties of the objects, as well as on the imaging geometry (Van Zyl & Kim, 2011). The backscatter from the ocean surfaces depends upon the sea surface roughness i.e. the orientation and wavelength of the gravity wave facets and on the wavelength of surface capillary waves. It also depends on the dielectric constant of the material present on the sea surface and on the solubility of the oil in sea water (Skrunes et al., 2014). Moreover, the look angle (θ) and the local incidence angle (θ_i) also influence the radar backscatter off the sea surface. (Equation 2.8-2.12).

In case of oil spills or other surface films, the capillary waves over the sea surface are dampened (Section 2.2), and the relative dielectric constant of the surface is also changed (Minchew, 2012). This results in a reduction in backscatter from oil spill regions as compared to the open water surfaces (Brekke et al., 2016; Fingas & Brown, 2014; Gade, Alpers, Hühnerfuss, Wismann, et al., 1998; Valenzuela, 1978; Wright, 1966). The reduction in backscatter is manifested in the SAR images captured by airborne and spaceborne SAR sensors, where oil spill regions appear as dark spots in wind-roughened backgrounds. Wind speed is also indirectly responsible for the variation in radar backscatter over surface films and water surface as wind causes the formation of the capillary waves. Figure 2 in Valenzuela (1978) shows the variation of Fresnel reflection co-efficient, as defined in Equation 2.11 & 2.12, with wind speed. At very low wind speeds (< 1.5 m/s), the ocean surface generally remains calm which results in lower backscatter from both oil spilled and open water regions. Moreover, at very high wind speeds (>15 m/s), capillary waves are formed over both oil spills and open water surfaces. Therefore, detection of oil spills becomes difficult at the two extremes of wind speeds. The optimum wind speed range for oil spill radar remote sensing is defined as 3 – 10 m/s (Espeseth et al., 2016; Fingas & Brown, 2014)

The incidence angle causes a variation in the radar backscatter from sea surface due to two major reasons. Firstly, because of the spread of the surface across the range direction of the SAR sensor. The radar equation indicates that the backscattered power is inversely proportional to the sine of the incidence angle (Van Zyl & Kim, 2011). Secondly, the radar cross section of the sea surface also depends on the incidence angle. A thorough study on the sea surface waves and is explained and illustrated in Valenzuela (1978). Various theoretical scattering models have been developed which dominate in different ranges of the incidence angles. It is concluded from the findings that Bragg scattering model explains the surface scattering of radar waves in the approximate incidence angle range of 20° to 75° and wind speed range of 3-12m/s (Valenzuela, 1978; Wright, 1966). The response of the radar wave is also dependent on the polarization of transmitted radar wave also the received radar wave. This is theoretically explained by the Bragg scattering model, as described in the next section.

2.3.2. Theoretical Bragg Scattering Model

The theoretical foundations for the use of radar for ocean and sea surface monitoring had been laid out by Valenzuela (1978). Bragg scattering occurs when the size of the objects on the scattering surface are similar to the wavelength of the electromagnetic wave. The backscatter response from these scatterers on the ocean surface are usually co-polarized and the ocean surface waves have the wave number

$$k_B = 2 k_r \sin(\theta_i) \quad (2.4)$$

where k_B is the Bragg wave-number, k_r is the radar wave-number, and θ_i is the local incidence angle. Each facet, or crest, of the ocean surface caused by the long gravity waves can be modelled using the 2-D tilted Bragg model. The geometry of these facets can be explained by two angles ψ and ζ . ψ is the angle between the projection of the titled facet's normal on the scattering plane and the vertical, whereas ζ is the angle between the vertical and the projection of the titled facet's normal onto the plane perpendicular to the scattering plane (Figure 2). The local incidence angle (θ_i) can be derived in terms of ψ and ζ using Equation 2.5.

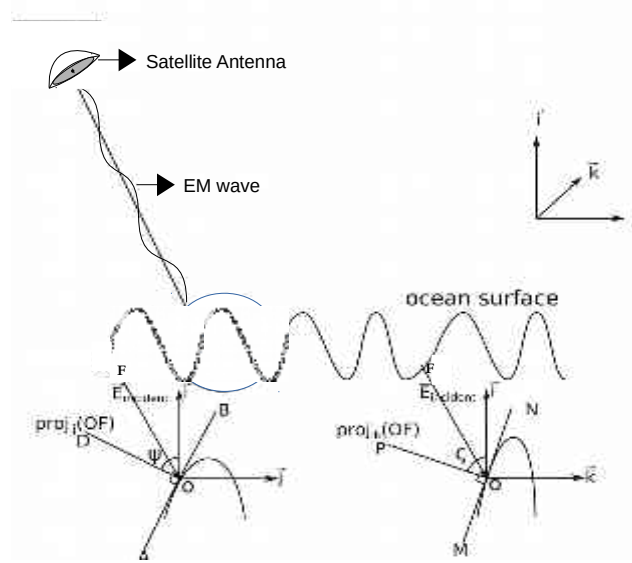


Figure 2: Geometry of interaction between radar waves and sea surface waves, with reference to 2-D tilted Bragg scattering model.

$$\theta_i = \cos^{-1}[\cos(\theta + \psi)\cos(\zeta)] \quad (2.5)$$

In the above formula, θ is the look angle. The co-polarized normalized radar cross section (NRCS) is given by the following equation

$$\sigma_{pp}^0 = 4\pi k_r^4 \cos^4 \theta_i \Gamma_{pp} W ; \quad PP \in \{HH, VV\} \quad (2.6)$$

where $W(\cdot)$ is the 2D wavenumber spectral density of ocean roughness spectrum and it describes the shape of the radar signal scattered from the sea surface. Γ is the integral of radiated power over all reflection angles. The reflectivity at each of the two co-polarization channels is described as a function of facet tilt (ψ and ζ), look angle (θ), local incidence angle (θ_i), and dielectric constant (ϵ_r) in the following equation

$$\Gamma_{PP} = \left| \left(\frac{(\sin(\theta + \psi)\cos\zeta)}{\sin(\theta_i)} \right)^2 R_{PP}(\theta_i) + \left(\frac{\sin\zeta}{\sin\theta_i} \right)^2 R_{QQ}(\theta_i) \right|^2 ; \quad PP, QQ \in \{HH, VV\} \quad (2.7)$$

R_{HH} and R_{VV} are Bragg scattering coefficients or Fresnel reflection coefficients and are given Equations (2.11) and (2.12) respectively. The theoretical backscatter for each polarization is given by the following equations,

$$\begin{aligned} \sigma_{HH}^0 = & 4\pi k_r^4 \cos^4 \theta_i \left| \left(\frac{(\sin(\theta + \psi)\cos\zeta)}{\sin(\theta_i)} \right)^2 R_{HH}(\theta_i) + \left(\frac{\sin\zeta}{\sin\theta_i} \right)^2 R_{VV}(\theta_i) \right|^2 \\ & \times W(2k_r \sin(\theta + \psi), 2k_r \cos(\theta + \psi)\sin\zeta) \end{aligned} \quad (2.8)$$

$$\sigma_{VV}^0 = 4 \pi k_r^4 \cos^4 \theta_i \left| \left(\frac{\sin(\theta + \psi) \cos \zeta}{\sin(\theta_i)} \right)^2 R_{VV}(\theta_i) + \left(\frac{\sin \zeta}{\sin \theta_i} \right)^2 R_{HH}(\theta_i) \right|^2 \quad (2.9)$$

$$\times W(2 k_r \sin(\theta + \psi), 2 k_r \cos(\theta + \psi) \sin \zeta)$$

$$\sigma_{HV}^0 = 4 \pi k_r^4 \cos^4 \theta_i \left(\frac{\sin(\theta + \psi) \sin \zeta \cos \zeta}{\sin^2(\theta_i)} \right)^2 |R_{VV}(\theta_i) - R_{HH}(\theta_i)|^2 \quad (2.10)$$

$$\times W(2 k_r \sin(\theta + \psi), 2 k_r \cos(\theta + \psi) \sin \zeta)$$

where ϵ_r is the relative dielectric constant (Valenzuela, 1978). The ocean wave spectral density is independent of polarization and therefore can be cancelled out in the ratio of radar cross sections. Therefore, a ratio of any two of the radar cross sections can be used to calculate ψ and ζ . Determination of the two angles can be useful in estimating the slope of the adjacent slick.

$$R_{HH} = \frac{\cos(\theta_i) - \sqrt{\epsilon_r - \sin^2(\theta_i)}}{\cos(\theta_i) + \sqrt{\epsilon_r - \sin^2(\theta_i)}} \quad (2.11)$$

$$R_{VV} = \frac{(\epsilon_r - 1) \left\{ \sin^2(\theta_i) - \epsilon_r [1 + \sin^2(\theta_i)] \right\}}{(\epsilon_r \cos(\theta_i) + \sqrt{\epsilon_r - \sin^2(\theta_i)})^2} \quad (2.12)$$

Moreover, if the relative dielectric constant is represented as a weighted sum of the dielectric constants of oil and water, it can be used to estimate the amount of water-oil mixing in an oil emulsion spilled over the sea surface. The equation for the relative dielectric constant is described in Equation 2.13, where w_0 is the weight factor for oil, ϵ_r^{oil} and $\epsilon_r^{\text{water}}$ are the relative dielectric constant of oil and water respectively (Minchew, 2012). Lower values of w_0 indicate higher concentrations of oil in an oil-water mixture, whereas higher values of w_0 suggest that a slick is diluted and has more water than oil in the mixture. Therefore, after estimating the spectral density of ocean surface, $W(\cdot)$, R_{HH} and R_{VV} can be used to estimate the proportion of oil and water in the sea surface emulsions.

$$\epsilon_r = \epsilon_r^{\text{eff}} = w_0 \epsilon_r^{\text{oil}} + (1 - w_0) \epsilon_r^{\text{water}} \quad (2.13)$$

After this brief introduction about the interaction between radar waves and sea surface waves, we can now move on to next section which briefly describes the analysis of gathered radar data for oil spill detection and characterization.

2.4. Oil spill detection and characterization using SAR images

Oil spills can be detected and characterized by using ancillary data, existing knowledge about the information of evolution of slicks, statistical information of the images, contextual and polarimetric features derived from radar images, or by the estimation of dielectric constant and mixing in the oil spill. Using all the above information, data segmentation and classification methods can be used to delineate the oil-water boundaries and classify oil and water pixels. Some of the methods stated above are described in the following subsections.

2.4.1. Techniques of Detection and characterization using Ancillary Data

The presence of slicks over sea or ocean surfaces causes a reduction in the radar backscatter in both co-polarized and cross-polarized channels. Basic segmentation approaches are useful in differentiating these slicks from the ocean surface (Migliaccio, Gambardella, et al., 2007). However, it is difficult to distinguish between mineral and biogenic slicks on the bases of their radar backscatter. The shape of the slick and its position relative to spill causing objects are influential in determining marine oil spills from other look alike. For instance, a linear dark strip following an extremely bright object suggests higher chances of the dark region being caused due to ship wakes on the water surface. In some cases, the dark areas in SAR images appear feather shaped. This happens due to the movement of strong winds over the sea surface. Heavier oils such as mineral oils interact more with wind at the interface as compared to monomolecular biogenic slicks. Espedal (1999), cited in Alpers et al. (2017) concludes that such an appearance indicates higher chances of the surface slick being a mineral oil slick rather than biogenic oil slick. Marine oil spills can also be distinguished from rain cells by integrating ancillary information such as weather radar data and sea charts (Alpers et al., 2016). Cold upwelling zones can be distinguished by using sea surface temperature (SST) information (Clemente-Colón, 2004).

The variation in the texture of the image has also been exploited in detecting oil spills. Contextual features extracted using grey level co-occurrence matrix (GLCM) (Haralick, Shanmugam, & Dinstein, 1973) and used as inputs to data classification algorithms. Brekke & Solberg (2005) concluded that homogeneity was the most useful GLCM features to extract oil spills. Lopez & Moctezuma (2005) used contextual features extracted using GLCM and used Markov Random Field (MRF) based segmentation method to delineate oil spills. The use of GLCM features in oil spill detection has also been explored by Espeseth et al. (2017) and Liu, Zhao, Li, He, & Pichel (2010).

2.4.2. Stats of SAR images and characteristics of SAR sensor:

Every SAR sensor is characterised by an internal system noise. This internal noise determines the system's normalised equivalent sigma zero (NESZ). It is preferable to use a SAR sensor which has system noise floor much lower than the signal from oil spills such that the noise doesn't corrupt the signal from the oil slicks. UAVSAR is known to have one of the lowest system noise floor out of all presently functioning SAR sensors with its NESZ ~ 53 dB at its minimum (Minchew et al., 2012). The system noise floor of UAVSAR and also other sensors varies with incidence angle (Fore et al., 2015). Other satellite based radar sensors have slightly higher NESZ. For instance, X band TerraSAR-X have NESZ of -26.4 dB to -23.7 dB and C-band RadarSat-2 has an NESZ range -37.2 dB to -26.2 dB (Skrunes et al., 2016).

Theoretically, as discussed in Sections 2.2 and 2.3, radar backscatter varies according to the shape and dielectric properties of the scatterer. However, it is difficult to extract the true backscatter value of each pixel due to speckle, which is an innate property of SAR sensors. Speckle is caused by the constructive and destructive interference of coherent backscatter responses from the scatterers in a single resolution cell (Goodman, 1976). In case of a large cell size and homogeneous nature of scatterers, the real and imaginary parts of the scattering amplitude are normally distributed, whereas its magnitude follows a Rayleigh distribution. The phase of the signal is uniformly distributed over a range $(-\pi, \pi)$. The intensity of the signal is negative exponentially distributed. However, for inhomogeneous and spatially small scenes, the distribution of signal may vary from their description mentioned above (Alpers et al., 2017). Attempts have been made to model the speckle in the SAR images captured over sea surfaces by using a generalized K-probability distribution function by Migliaccio, Ferrara, Gambardella, Nunziata, & Sorrentino (2007). Moreover, a scalar product model has been used by Skrunes, Brekke, & Doulgeris (2015) to model the normally distributed speckle and non-Gaussian radar cross section.

2.4.3. Using Polarimetric Features

Fully Polarimetric Features

Equations 2.6 and 2.7 indicate that the radar backscatter from a surface is dependent upon the polarization channel. Multiple polarimetric features extracted using the covariance, coherency and scattering matrices, have been used to detect and characterize oil spills. Skrunes et al. (2016) concluded that intensity of VV channel, geometric intensity, real part of co-polarization cross product, eigen values of coherency matrix and span of the covariance matrix provided the best separability between oil spill and water regions. The separability was calculated on the basis of Fisher discriminant ratio (FDR). Espeseth et al. (2017) and Minchew et al. (2012) have also investigated the efficacy of damping ratios in distinguishing oil from water. Damping ratio is a function of Bragg coefficients and 2-D wave-number spectral density. Therefore, damping ratio (Minchew et al., 2012) is dependent upon the dielectric constant of the material present on the surface. The co-polarization power ratio is independent of ocean wave spectrum and is therefore only dependent upon the facet tilt, dielectric constant and incidence angle. The real and imaginary part of co-polarization cross product have also been used to detect oil spills. There is a decrease in correlation of the co-polarization channels when we move from open water to slick covered areas (Skrunes et al., 2014).

The phase difference between the co-polarization channels is used in terrain classification. The statistical properties of co-polarized phase difference (CPD) vary with radar wavelength, surface roughness, incidence angle, physical properties of the target, and homogeneity of the scene (Lee & Pottier, 2009). The variance of the probability density function (PDF) of CPD increases with increasing inhomogeneity of the scene. This occurs because of the reduction in coherence between phases of the two polarized channels. Migliaccio, Nunziata, & Gambardella (2009) concluded that the variance of CPD is larger for mineral slicks as compared to open water surface and biogenic oil slicks. Another polarimetric feature used for oil spill detection is the magnitude of co-polarization correlation coefficient. This feature is a function of surface roughness, the dielectric constant and incidence angle (Skrunes et al., 2014). It has been found to have low values for oil covered areas. The determinant of the covariance matrix has also been investigated and has been found to have lower values for oil slicks as compared to open water. The derivative features from the eigen-values of the covariance and coherency matrix i.e. entropy (H), anisotropy (A), mean alpha angle (α),

polarization fraction and pedestal height have also been studied. The entropy relates to the degree of randomness of the process of scattering, and its value varies between 0 and 1. Lower values suggest the presence of a single dominant scatterer whereas higher values indicate presence of random scattering in the scene. Anisotropy measures the relative values of the second and third eigen-values. The measure of the mean alpha angle relates to the type of scattering. For $\alpha = 0^\circ$, the surface scattering dominates, and as its value increases, the irregularity of the scattering increases until $\alpha = 45^\circ$ when volume scattering dominates. Furthermore, in the range of $\alpha \in (45^\circ, 90^\circ)$, double bounce scattering dominates (Kumar et al., 2016). These features are a function of large scale roughness of the sea surface, dielectric constant, and incidence angle (Espeseth et al., 2017).

Hybrid Polarimetric Features

Hybrid polarimetric architecture is defined on the basis of the circular polarization of transmitted wave and coherent dual linear received polarizations (CTLR). The objective of using this specific architecture for SAR data acquisition is to use the advantages of both dual polarization radar data and quad-polarized radar data without the limitations provided by quad-polarized (quad-pol) acquisitions such as halved swath coverage and doubled average transmitted power. Although this architecture is not a substitute for fully polarimetric architecture, this method can be used for monitoring larger ocean areas for oil spills, both spatially and temporally, as compared to fully polarimetric datasets (Raney, 2007).

Most of the hybrid polarimetric features are extracted using the elements of the Stokes vector (\mathbf{s}). The elements of the Stokes vector, s_0 represent the trace of the covariance matrix and the total power, s_1 represents the power in linear horizontal or vertical polarization, s_2 represents the power of the tilted linearly polarized components 45° and 135° , and s_3 is the power of the circularly polarized components (Espeseth et al., 2017). According to the two-scale Bragg model, s_0 and s_3 are dependent upon the wave spectrum, incidence angle and dielectric properties, similarly, s_1 and s_2 is a function of both terms in addition to the rotation angle. These features include degree of polarization (m), ellipticity angle (χ), circular polarization ratio, relative phase and alpha angle.

2.4.4. Data segmentation and classification methods:

There are various segmentation and classification algorithms which make use of polarimetric and contextual features to detect oil spills. Segmentation of oil slicks has been reported using a threshold based approach in Migliaccio, Gambardella, & Tranfaglia (2007). The choice of the threshold value is dependent upon the nature of surface films and the state of the sea at the time of data acquisition. More complex multi-stage unsupervised segmentation algorithms have also been reported to delineate oil spills (Espeseth et al., 2017). An example of a multi-stage algorithm is Extended Polarimetric Feature Space (EPFS) (Doulgeris, 2013; Espeseth et al., 2016). This image clustering method is based on Expectation Maximization (EM) of Gaussian Mixture Models (GMM). There are many classification methods which can be used to classify oil spills. They include maximum likelihood classifier (MLC), support vector machine (SVM), and Markov Random Fields (MRF) based classification methods. Moreover, PolSAR classification methods, such as Wishart classification have also been used in detecting oil spills (Kumar et al., 2016) and in classifying SAR data in general (Wu, Ji, Yu, & Su, 2008). The multilooked covariance matrix of multi-polarimetric SAR data follows a multivariate Wishart distribution. This is the basis for Wishart classification.

MRF based classification methods have been applied in the past to detect oil spills but only using hard classifiers (Lopez & Moctezuma, 2005; Moctezuma, Parmiggiani, & Lopez, 2014; Morales, Moctezuma, & Parmiggiani, 2008). One of the applications of surface modelling in feature detection was in the research conducted by Ardila, Tolpekin, Bijker, & Stein (2011). In this research, tree crowns were modelled as probability surfaces using class membership values from a fuzzy classification method. The modelling was performed by first defining tree regions using region growing method and then modelling the regions by fitting Gaussian models to the regions. This method was useful for the research because contextual information was able to capture and overcome large within-class spectral variation prevalent in vegetated areas in very-high resolution(VHR) images. A similar approach can be used to model oil spills over sea surfaces. This is because oil spills appear dense dark spots in the centre of the slick due to large damping effect of oil over the sea surface. This damping effect reduces in regions near the oil-water boundary which reflects in the gradual increment of radar backscatter. This gradual variation in spectral information is similar in cases of both oil spills and tree crowns.

The next chapter presents an overview of the chosen study area and datasets used for this research.

3. STUDY AREA AND DATASETS

The chosen study area is located in the Frigg Oil Field in the North Sea, approximately 150 kilometres to the west of Bergen, Norway. The approximate geographic co-ordinates of the top left corner of the bounding box encapsulating the study area is 2.07° E, 60.21° N (Figure 3) (Skrunes et al., 2016). The area comprises of oil spills which were intentionally spilled in the region as part of a joint exercise between Jet Propulsion Laboratory (JPL)-National Aeronautics and Space Agency (NASA), University of Tromsø (UiT) and The Norwegian Clean Seas Association for Operating Companies (NOFO). The name of the exercise was Norwegian Radar Oil Spill Experiment (NORSE)-2015 and was held on 10th June, 2015. The details of the experiment are described in Section 3.1, with details of the types of oil spilled in the sea, the sensors which acquired the data and the data about the conditions of the sea during the course of this exercise. Section 3.2 describes the details of the SAR datasets which were used in this research.

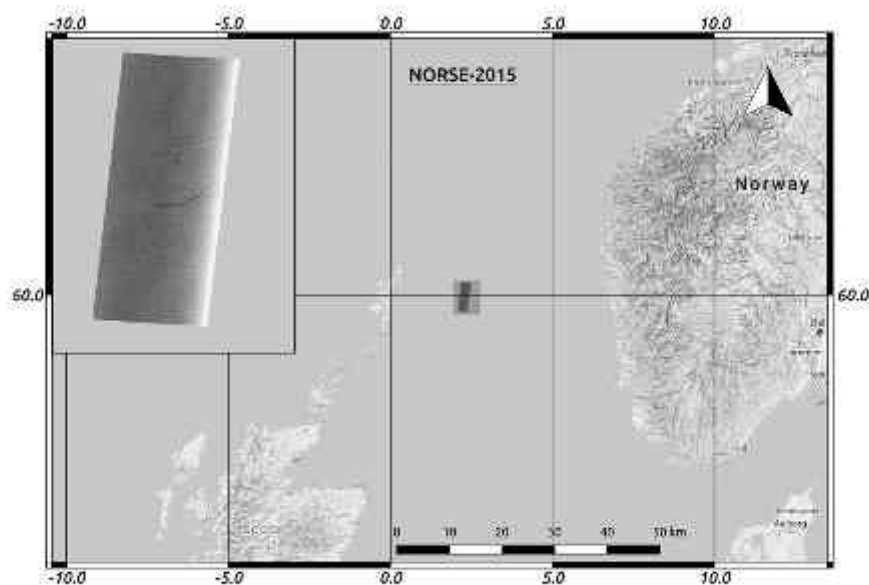


Figure 3: Location of the study area: Frigg oil Field in North Sea, approximately 150 kilometres to the west of Bergen, Norway. The geographic co-ordinates of the top left corner of the study area is 2.07° E, 60.21° N. The inset image shows the Pauli RGB image of one of UAVSAR's acquired datasets.

3.1. NORSE-2015

During the oil spill exercise, 4 different type of oil spills were spilled into the sea. Three of these spills were emulsions of sea water and mineral oils with varying concentration of oil in the spills, i.e. 80% (E80), 60% (E60), 40% (E40). The fourth spill was plant oil (PO), a monomolecular compound used to simulate natural biogenic slicks (Figure 4). The mineral oil emulsions were prepared using Troll crude oil, Oseberg crude oil and one-mul emulsifier (Exxon Mobil, 2018a, 2018b). The simulated Plant oil was prepared using Radiagreen

EBO, which is a biodegradable lubricant. The details of the slicks with the information of the oil type which was spilt is described in Table 2 and the relevant physical properties of the crude oils is described in Table 4.

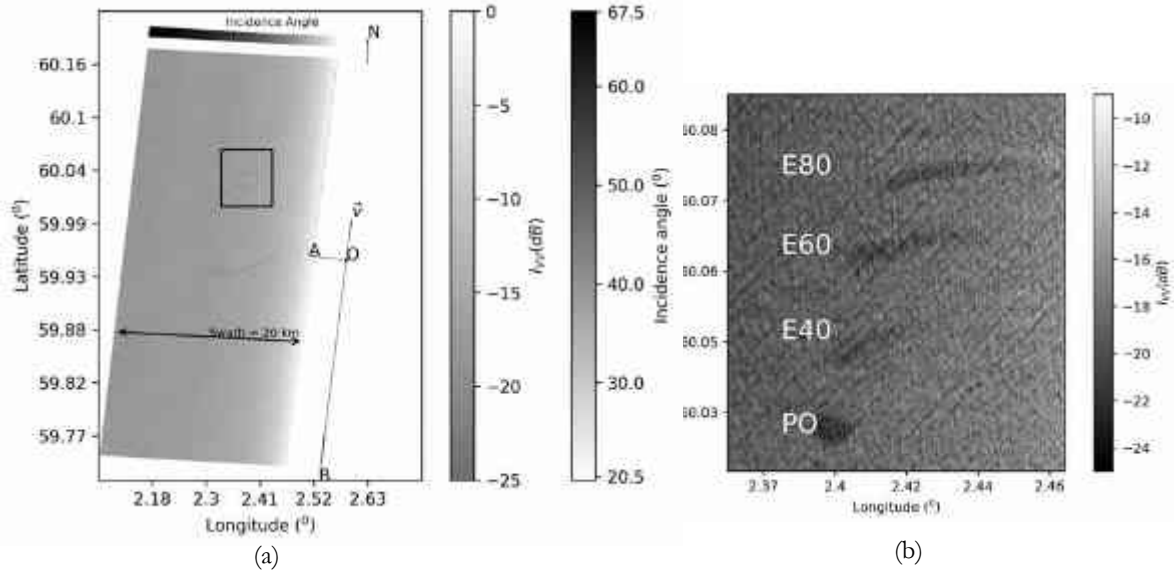


Figure 4: Depiction of flight acquisition geometry (a) and 4 distinct oil spills spilled in the area (b) as visualised in the VV intensity image of the GRD product of UAVSAR scene acquired at 11:45 AM UTC (a). The zoomed image (b) focuses on the 4 oil slicks. These slicks are E80, E60, and E40, and PO (Table 2). In (a), vector v denotes the velocity of the aircraft = 220 m/s with heading angle = 7° clockwise from north direction. OA and OB represent the row and column offsets respectively of the top left pixel of the acquired SLC image.

The location of the spills and the timing of the release was chosen as such that the slick area intersected with the swath widths of multiple satellite sensors. The release of spills were closely separated in time and the spills had at least one hour to evolve before the pass of the first satellite (TerraSAR-X) over the region (Table 3). Moreover, the spills were released such that their location was aligned in the direction parallel to the azimuth direction of the sensors. It was also ensured that the spill location fell in the middle of the scenes, such that the signal to noise ratio (SNR) was maximised. The spatial separation between the slicks was approximately 0.5 nautical miles (nmi). The datasets were captured using UAVSAR, an airborne SAR sensor operated by NASA, RISAT-1, TerraSAR-X, RadarSat-2, and ALOS-2 (Table 3).

The environment conditions during the oil spill exercise were relatively rough. The wind speed varied in a range of 9-12 m/s. The direction of the wind ranged from 248° to 264° (measures clockwise from North-South direction) during the course of the exercise, with the wind coming from west-southwest direction. The swell of the sea, which is the direction of motion of surface-gravity waves of the sea surface, was from the north-west to the south-east direction i.e. oblique to the wind direction. The height of the sea waves varied between 2-2.5 meters (Table 5). More details are described in Table 2 and Section 2.2 in Jones et al. (2016) and in Section C in Skrunes et al. (2016). During the exercise, 2 types of drift buoys, namely, iSphere drifter, which is specifically designed to track oil spills, and self locating datum marker buoy (SLDMB)) were

also employed. Each of the two buoys were placed at the PO slick and the other at the E80 slick. The motion of the iSphere drifter was influenced by surface currents, winds and sea surface waves, whereas SLDMB mostly moved along the direction of the surface current only. The trajectory of the buoys can be visualized on Figure 1 of Jones et al. (2016).

Table 2: Description of the experimental oil spills in NORSE2015 (Brekke et al., 2016).

Oil Slick	Time of release (UTC)	Composition of spill	Volume (liters)
PO	04:48	Plant Oil: Radiagreen ebo	200
E40	04:59	Emulsion (40% oil): 300 L water + 100 L Troll + 100 L Oseberg + 0.2 L One-Mul	500
E60	05:15	Emulsion (60% oil): 200 L water + 150 L Troll + 150 L Oseberg + 0.2 L One-Mul	500
E80	05:30	Emulsion (80% oil): 100 L water + 200 L Troll + 200 L Oseberg + 0.2 L One-Mul	500

Table 3: List of SAR datasets acquired during NORSE-2015 (Skrunes et al., 2016)

Sensor	Time(UTC)	Mode	Freq. Band	Polarization
UAVSAR (22scenes)	5:32 – 13:18	PolSAR	L-band	Quad-pol
TerraSAR-X (2 scenes)	06:24, 17:12	Stripmap	X-band	Dual-pol (HH, VV)
RADARSAT-2	06:28	Wide fine quad	C-band	Quad-pol
RISAT-1	07:19	Fine Resolution Stripmap	C-band	Hybrid-pol (RH, RV)
ALOS-2	23:53	High sensitive	L-band	Single-pol (VV)

Table 4: Relevant physical properties of components used in oil emulsions (Exxon Mobil, 2018a, 2018b)

Oil Type	Specific Gravity	Kinematic Viscosity at 40°C (centi-Stokes)
Troll Crude	0.846 (at 15.5°C)	3.5
Oseberg Crude	0.827 (at 15.5°C)	2.7
Radiagreen ebo	0.95 at 25°C	8

Table 5: MetOcean data of Frigg Oil Field on 10th June, 2015 (Jones et al., 2016)

Time (UTC)	Wind Velocity (m/s) (from °N)	Wave height (m)	Temperature (°C)
04:50	11	2.5	9 ^o
07:15	12 (263 ^o)		
09:00	9	2.5	11 ^o
13:00	12	2.5	10 ^o
15:30	10 (264 ^o)		

The advantage of choosing this study area was that it allowed an investigation of three different types of mineral oil spills which were quite similar in their radar backscatter responses. This exercise also allowed us to study the differences between mineral and biogenic oil spills. There was an opportunity to study the oil spills with multi-frequency datasets which were acquired during this exercise. Moreover, the acquisition of data for a period of 8 hours allows a multi-temporal study of the evolution of oil spills. The exact knowledge of the type of oil spilt into the sea also allows a study on the estimation of physical properties of oil. Furthermore, the registration of the met-ocean data during the course of this exercise also allows studies which try to relate the effects of met-ocean data such as wind velocity and sea surface current velocity to the dynamics of the oil spill.

3.2. SAR dataset Description

The oil slicks were mapped using both space-borne SAR sensors as well as UAVSAR airborne sensor (Table 3). UAVSAR collected data in 2 separate flights (flight numbers: 091 and 092) and acquired a series of 22 scenes. One of these scenes is used for developing the detection and characterization methodology and the remaining scenes are used for testing the effectiveness of the detection method. Moreover, RISAT-1 hybrid polarimetric dataset (RH, RV (Raney, 2007)) and TerraSAR-X dual polarimetric (HH, VV) dataset have also been used for this research, but only to the extent of testing the detection algorithm.

3.2.1. UAVSAR

UAVSAR is an airborne SAR sensor operated by NASA-JPL which acquires linear quad polarized SAR datasets. It has been used to conduct various studies in the field of SAR polarimetry, interferometry and polarimetric SAR interferometry which can be explored on the UAVSAR publications page (NASA, 2015). This SAR platform participated in the NORSE-2015 exercise and collected 22 scenes during two separate flights over the course of the day. The details of the datasets used for this study can be found in Table 6. The data acquisition geometry for the 17th scene acquired at 11:45 UTC is explained in Figure 4(a). This scene is used for the majority of the analysis in further chapters. The advantage of using this scene is that we can analyse the scene after the oil slicks have stretched due to the effects of wind and water surface, and have been on the sea surface for approximately 6 hours. The figure 4(a) shows the direction of flight while acquiring the dataset. Due to this particular flight geometry, the orientation of the oil slicks in SLC and MLC products appears to be inverted (Figure 8) in both azimuth and range directions, as compared to the GRD

product. The other two datasets: RISAT-1 and TerraSAR-X have been used in this study only to compare relevant polarimetric features with UAVSAR's polarimetric features and to test the oil spill detection algorithm.

3.2.2. RISAT-1

RISAT-1 is a spaceborne SAR satellite operated by the Indian Space Research Organization (ISRO) which acquires SAR data in compact polarimetric mode i.e. circularly transmitted and linearly received (CTLR). This satellite also captured the data of the oil spills spilt during NORSE-2015 on 10th June, 2015 while making a descending pass over the study area at time 07:19 UTC. The details of the dataset is represented in Table 6. The dataset is cropped to the extent of the oil spills as shown in Figure 5.

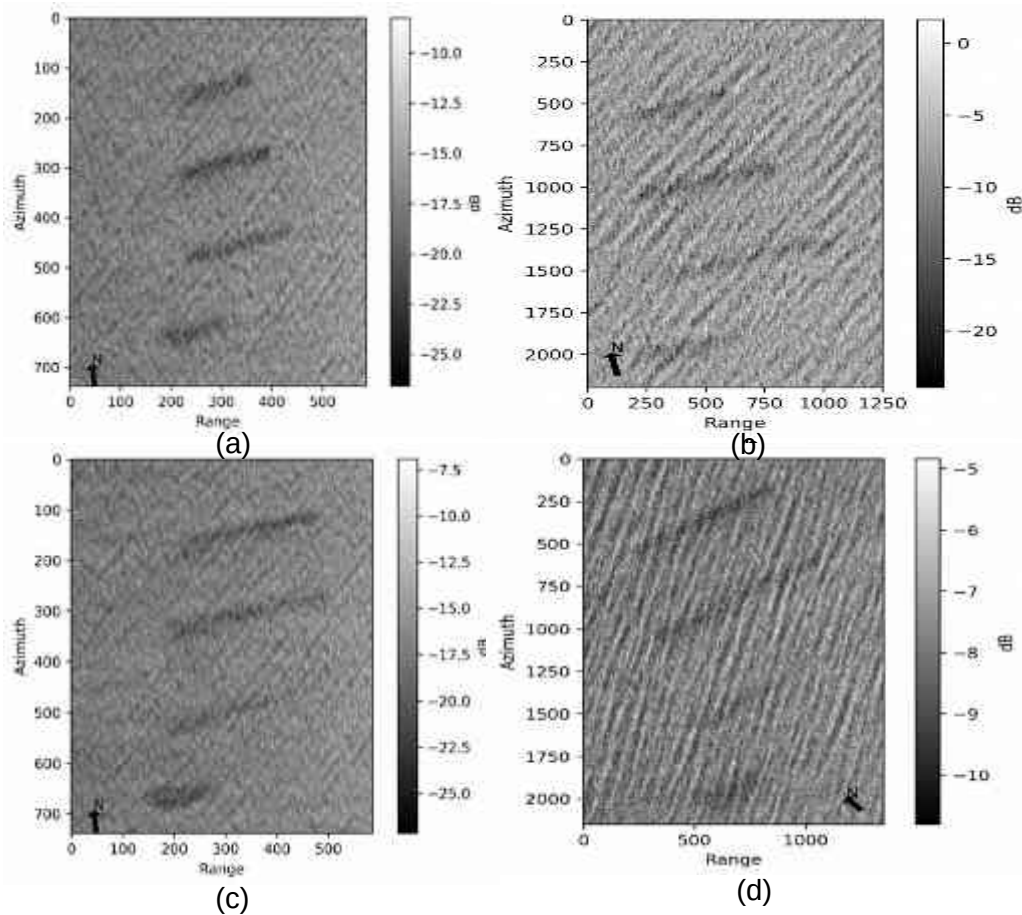


Figure 5: Intensity VV images of UAVSAR (a,c) and TerraSAR-X (b) and Intensity RV image of RISAT-1 data (d). The number of looks, time of acquisition, and image resolutions are mentioned in Table 6. The UAVSAR data (a) corresponds to TerraSAR-X data (b), and UAVSAR data (c) corresponds to RISAT-1 data (d). The northern direction is represented by an arrow at the bottom of each image.

Table 6: Metadata of UAVSAR, RISAT-1 and TerraSAR-X datasets

Sensor	UAVSAR (mlc)	RISAT-1(slc)	TerraSAR-X (SSC)
Product-Id	UA_norway_00709* UA_norway_18709*	1515551004	TSX1_SAR__SSC____ __SM_D_SRA_2015 0610T062401_201506 10T062409
Frequency	L band (1.2175 – 1.2975 GHz)	C band (5.35 GHz)	X-band
Product type	MLC	SLC	SSC
Polarization	Quad-Pol	Hybrid-Pol (RH, RV)	Dual-Pol (HH, VV)
Incidence angle range	21 ⁰ – 65 ⁰	43.184 ⁰ – 44.836 ⁰	27.3 ⁰ – 29 ⁰
Slant Range Resolution	4.99 m	1.17 m	2.48 m
Azimuth Resolution	7.2 m	3.33 m	6.66 m
No. of Looks	Range looks=3 Azimuth looks=12	Single look	Single look
Swath width	20 km		15 km
Noise Equivalent Sigma Zero (NESZ)	-48 to -33 dB		-26.4 to -23.7
Incidence Angle Range	19.5 ⁰ – 67.5 ⁰	43.2 ⁰ – 44.8 ⁰	27.3 ⁰ - 29 ⁰
Date and Time acquisition (UTC)	10-06-2015, 05:32 – 13:18	10-06-2015, 07:19	10-06-2015, 06:24
No. of Scan-lines	7201	13561	23319
No. of samples	3300	9821	8736
Pass	Ascending	Descending	Descending
Look Direction	Left	Right	Right
Heading Angle	7 ⁰ , 187 ⁰	222 ⁰	193 ⁰

Key: *all products with product id's beginning with this string

3.2.3. TerraSAR-X

As mentioned in Table 2, the TerraSAR-X satellites were able to capture the dataset at two instances. The first of the set of two acquisitions was used for analysis in this work. The second of the TerraSAR-X data acquisition occurred late in the evening and therefore is outside the scope of this work. The metadata of the dataset is mentioned in Table 6. Both channels of the dataset (HH and VV) were initially cropped to the extent of the oil slicks (Figure 5). The dataset is calibrated using the Radiometric calibration tool in sentinel-1 toolbox which applies the methodology given in Infoterra GmbH, 2008.

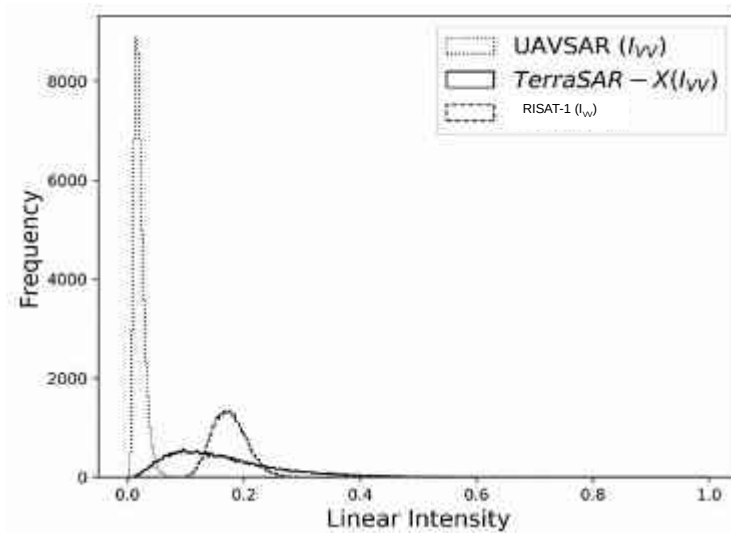


Figure 6: Histograms showing data distribution of UAVSAR, TerraSAR-X and RISAT-1 as shown in Figure 5(a), (b), and (d).

The data distributions of all the three datasets are compared in Figure 6 using 50000 randomly selected points. From an initial observation, the distributions of UAVSAR and TerraSAR-X are skewed towards the left. However, the distribution of RISAT-1 seems to follow a Gaussian distribution.

The next chapter describes the use of the above datasets in developing an oil spill detection methodology.

4. METHODOLOGY

This chapter describes the methods adopted for detection, characterization and probability surface modelling of the oil spills captured in UAVSAR, RISAT-1 and TerraSAR-X datasets. The methods include initial preprocessing, feature extraction, slick segmentation, oil slick analysis, feature comparison, image categorization and probability surface modelling. An overview of the methodology followed for this research is depicted in Figure 7.

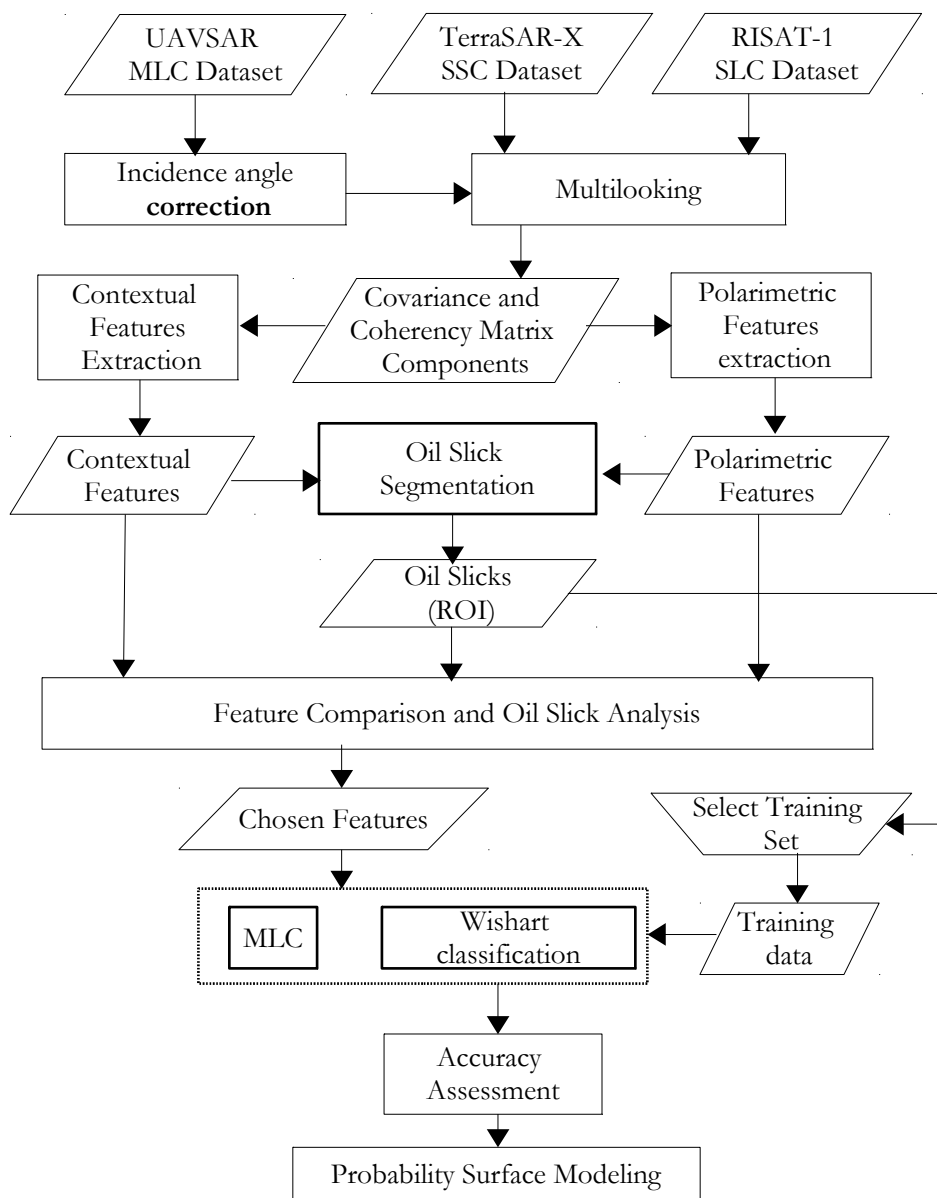


Figure 7: Methodological Flow Diagram

Before beginning this chapter thoroughly, it should be understated that most of the processing of the datasets was performed in python. The python libraries which were extremely crucial for the analysis were matplotlib, numpy, scipy, and scikit-learn (Hunter, 2007; Oliphant & E., 2007; Pedregosa et al., 2011).

4.1. Data Extraction

UAVSAR

The SLC image for the data product with product identity 'UA_norway_00709_15092_000_150610_L090_CX_01' was chosen for analysis. The SLC and MLC datasets of the product were considered for analysis. The MLC product was manually cropped to the region which contains the 4 oil slicks (Figure 8). The extent of the cropped image was 1185 rows * 1025 columns (row – 521:1543; columns – 4049:5233). This was done to reduce the computation time for further algorithms and also to focus more on the oil slicks. Location of the slicks were identified using manual observation. The location of the oil slick region in the MLC product was used to calculate the corresponding locations in the SLC product using the knowledge of the number of looks in both range and azimuth directions. The VV intensity component of the cropped MLC image and its corresponding SLC image of the area can be observed in Figure 8. The incidence angle of the image along the range direction varies between 40 degrees in the near range (left) and 56 degrees in far range (right).

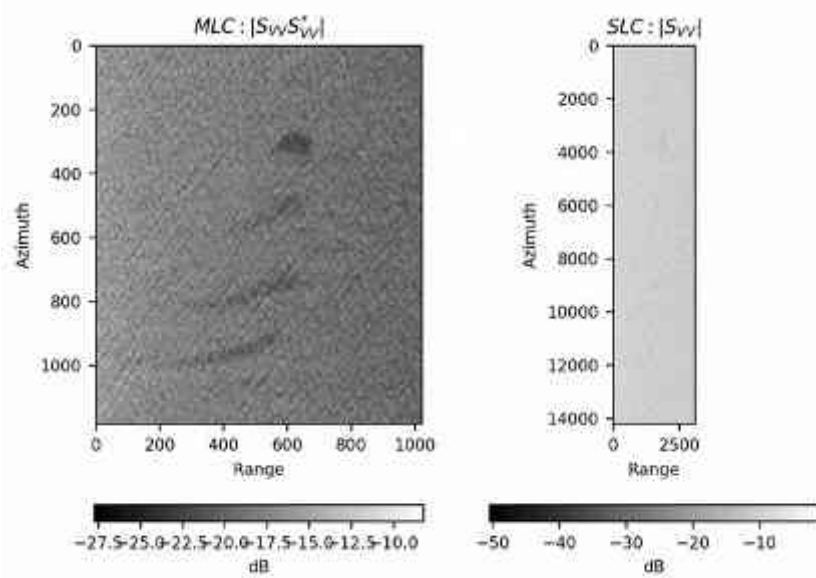


Figure 8: VV intensity images of multi-looked (left) and single look (right) images of cropped region containing oil slicks. The number of looks in the multilooked image is 12 and 3 in azimuth and range direction respectively.

RISAT-1 and TerraSAR-X data extraction

The RISAT-1 SLC data was read and extracted using PolSAR-pro. Both TerraSAR-X and RISAT-1 datasets were cropped to the extent of oil spills. The differences between the UAVSAR airborne data, and spaceborne TerraSAR-X and RISAT-1 datasets were observed.

4.2. Scattering mechanism of sea surface

The UAVSAR dataset is fully polarised and therefore provides an opportunity to explore the scattering mechanism of the electromagnetic waves from the surface of the sea. The scattering mechanism was studied using coherent and incoherent polarimetric decomposition methods. The coherent and incoherent decomposition methods studied were Pauli decomposition and Freeman & Durden decomposition respectively. The results from the decomposition were analysed and thereby the scattering mechanism was analysed. This analysis is carried out while considering that there was a high incidence angle variation in the UAVSAR dataset. Similarly, $m\text{-}\chi$, $m\text{-}\delta$ and $m\text{-}\alpha$ decompositions (Tomar, 2015) were carried out on compact polarised RISAT-1 dataset for the area. The results were then analysed to understand the nature of scatterers in the region surrounding the oil spills.

UAVSAR polarimetric analysis

Pauli Decomposition

The polarimetric decompositions express the scattering matrix in a particular basis. The scattering matrix is expressed as in Equation 4.1 (Lee & Pottier, 2009).

$$S = \begin{bmatrix} S_{hh} & S_{hv} \\ S_{vh} & S_{vv} \end{bmatrix} \quad (4.1)$$

The measured scattering matrix expresses the scattering matrix in the Pauli basis. The Pauli basis in the orthogonal linear basis are $\{[S]_a, [S]_b, [S]_c, [S]_d\}$, as shown in Equation 4.2 (Lee & Pottier, 2009).

$$[S]_a = \frac{1}{\sqrt{2}} \begin{bmatrix} 1 & 0 \\ 0 & 1 \end{bmatrix}; [S]_b = \frac{1}{\sqrt{2}} \begin{bmatrix} 1 & 0 \\ 0 & -1 \end{bmatrix}; [S]_c = \frac{1}{\sqrt{2}} \begin{bmatrix} 0 & 1 \\ 1 & 0 \end{bmatrix}; [S]_d = \frac{1}{\sqrt{2}} \begin{bmatrix} 0 & -1 \\ 1 & 0 \end{bmatrix} \quad (4.2)$$

Due to the reciprocity condition in the present monostatic case, $S_{hv} = S_{vh}$. Therefore, the Pauli basis reduces to $\{[S]_a, [S]_b, [S]_c\}$. The scattering matrix can be expressed as in Equation 4.3, where α , β , and γ are expressed in Equation 4.4.

$$S = \alpha [S]_a + \beta [S]_b + \gamma [S]_c \quad (4.3)$$

$$\alpha = \frac{S_{hh} + S_{vv}}{\sqrt{2}}; \beta = \frac{S_{hh} - S_{vv}}{\sqrt{2}}; \gamma = \sqrt{2} S_{hv} \quad (4.4)$$

The UAVSAR SLC product was used for the calculation of Pauli decomposition components α , β , and γ . The components are then multilooked with 3 looks in the range direction and 12 looks in the azimuth direction. The resulting components of the Pauli decomposition and RGB codified image was generated using the colour code - Red: $|\beta|$, Green: $|\gamma|$, Blue: $|\alpha|$ are reported in Section 5.1.

Freeman-Durduin Decomposition

Incoherent target decompositions, as opposed to coherent decompositions, are used to characterize distributed targets. Such target are highly influenced by speckle and therefore, second order polarimetric representation such as covariance matrix and coherency matrix ($\langle [C_3] \rangle$ and $\langle [T_3] \rangle$ respectively) are used to analyse such targets. In case of incoherent decompositions, $\langle [C_3] \rangle$, or $\langle [T_3] \rangle$ matrices are separated into a superposition of second order matrices describing canonical objects. The decomposition theorems using the $\langle [C_3] \rangle$ can be described as

$$\langle [C_3] \rangle = \sum_{i=1}^k p_i [C_3]_i \quad (4.5)$$

The responses of the canonical targets are represented by $[C_3]_i$, with p_i denoting the coefficients of the components $[C_3]_i$. The covariance matrix is modelled as a contribution of three scattering mechanisms in Freeman decomposition (Freeman & Durden, 1998). These are

- Single bounce scattering, which is modelled by a first order Bragg surface scatterer.
- Double bounce scattering, which is modelled by a dihedral corner reflector
- Volume scattering, modelled as a set of randomly oriented dipoles (Van Zyl & Kim, 2011).

PolSAR-Pro software was used to calculate the components of Freeman decomposition.

RISAT-1 polarimetric analysis

Hybrid polarimetric decomposition model can be used to understand the scattering mechanism in the RISAT-1 image. The three decomposition models used in this study were m- χ , m- δ , and m- α decomposition. The four child parameters of the stokes vector, i.e. degree of polarization (m), relative phase (δ), ellipticity angle (χ) and polarization alpha angle (α) (Section 2.4.3) were used in the decomposition models mentioned above (Tomar, 2015). The RGB composites of m-chi, m-alpha and m-delta decompositions are reported in Section 5.1.

4.3. Preprocessing

UAVSAR Incidence Angle Correction

The incidence angle range of UAVSAR, an airbourne sensor, is much larger than space-bourne sensors (eg. TerraSAR-X) (Table 6) for the same swath width. This large variation in incidence angle manifests in UAVSAR datasets. Consequently, there is a large variation in backscatter values along the range direction in UAVSAR dataset. To reduce the effect of this variation, an incidence angle normalization is required before further processing of the dataset. In literature there are various methods tested for incidence angle normalization. They include sine/cosine based methods, regression based methods and advanced histogram

equalization based methods (Mladenova, Jackson, Bindlish, & Hensley, 2013). For this study sine based incidence angle normalization was chosen because of its simplicity and effectiveness in normalizing the radar backscatter in the range direction. The correction can be expressed through Equation 4.6.

$$\sigma_{PQ}^0(\theta_i) = \sigma_{PQ}^{0'}(\theta_i) \frac{\sin^n(\theta_i)}{\sin^n(\theta_{ref})}; \text{ where } P, Q \in \{H, V\} \quad (4.6)$$

In the above formula, $\sigma^0(\theta_i)$ represents the radar cross section after incidence angle normalization, $\sigma^{0'}(\theta_i)$ represents the radar cross section of the original image. Both σ^0 and $\sigma^{0'}$ are represented as functions of local incidence angle (θ_i). The reference angle to which the normalized radar cross section is normalized, is represented by θ_{ref} . The value of θ_{ref} was chosen to be that of the incidence angle at the centre of the image. The degree n , is the power index which characterizes the surface roughness. Its value was chosen to be 1. However in existing research, it has been reported that the efficiency of the cosine/sine based method can be improved by using an adjusted value of n using linear regression model (Ardila, Tolpekin, & Bijker, 2010). Slick detection and characterization was performed with and without applying incidence angle correction and the results were compared.

4.4. Feature Extraction

This section describes the details of the features used in detecting and characterizing oil spills. These features are fully polarimetric, extracted from UAVSAR data as well as hybrid polarimetric features extracted from RISAT-1 data.

UAVSAR

The UAVSAR polarimetric and GLCM contextual features introduced in Section 2.4.3 were used for oil spill detection and classification in this study. The features, which were specifically used in slick detection and characterization, have been listed in Table 7. Other polarimetric features used for the analysis have been described and shown in Appendix-B. The window size used for computing the features was 9×9 , the GLCM features were extracted using a lag of 1 along both axes, and direction of 0 degrees. The association of these polarimetric parameters to physical parameters is discussed in Section 2.4.3.

RISAT-1

The hybrid polarimetric features used in this study are mentioned in Table 8. The details of the polarimetric features and their relation to the physical parameters of radar wave and oil/water surface is mentioned in Section 2.4.3.

Table 7: Fully Polarimetric Features extracted from UAVSAR data. The MLC dataset was spatially averaged using a 9×9 window size. The contextual features were extracted using the same window size, a lag of 1 along both axes, and direction = 0 degrees.

<u>Name</u>	<u>Formula</u>
Polarimetric Features	
Co-polarization and cross-polarization intensities	$I_{HH} = \langle S_{HH} S_{HH}^* \rangle $, $I_{HV} = \langle S_{HV} S_{HV}^* \rangle $, $I_{VV} = \langle S_{VV} S_{VV}^* \rangle $
Co-polarization cross product (Skrunes et al., 2014)	$r_{CO} = \Re(\langle S_{HH} S_{VV}^* \rangle) $, $i_{CO} = \Im(\langle S_{HH} S_{VV}^* \rangle) $
Determinant of covariance matrix (Skrunes et al., 2014)	$det(C_{FP})$
Co-polarization difference (Kudryavtsev, Chapron, Myasoedov, Collard, & Johannessen, 2013)	$PD = \langle S_{HH} ^2 \rangle - \langle S_{VV} ^2 \rangle$
Eigen-values of coherency matrix	$\lambda_1 > \lambda_2 > \lambda_3$
GLCM Features (Haralick et al., 1973)	
Contrast	$f_{con} = \sum_{i,j=0}^{N-1} (i-j)^2 P_{i,j}$
Dissimilarity	$f_{dis} = \sum_{i,j=0}^{N-1} i-j P_{i,j}$
Angular Second Moment (ASM)	$f_{ASM} = \sum_{i,j=0}^{N-1} P_{i,j}^2$
Energy	$f_{Ener} = \sqrt{\sum_{i,j=0}^{N-1} P_{i,j}^2}$
Homogeneity	$f_{Hom} = \sum_{i,j=0}^{N-1} \frac{P_{i,j}}{1+(i-j)^2}$

Key: For all the GLCM features, N represents the window size, P_{ij} represent the (i,j)th entry in a normalized gray-tone spatial dependence matrix; i and j represents the gray tones of neighbouring pixels.

Table 8: Hybrid polarimetric features extracted using hybrid polarized RISAT-1 data

Name	Formula
Stokes vector (Raney, 2007)	$\mathbf{s} = \begin{bmatrix} s_0 \\ s_1 \\ s_2 \\ s_3 \end{bmatrix} = \begin{bmatrix} \langle S_{RH} ^2 + S_{RV} ^2 \rangle \\ \langle S_{RH} ^2 - S_{RV} ^2 \rangle \\ 2 \Re \langle (S_{RH} S_{RV}^*) \rangle \\ -2 \Im \langle (S_{RH} S_{RV}^*) \rangle \end{bmatrix}$
Degree of Polarization (Salberg, Rudjord, & Solberg, 2014)	$m = \frac{\sqrt{s_1^2 + s_2^2 + s_3^2}}{s_0}$
Ellipticity angle (Cloude, Goodenough, & Chen, 2012)	$\chi = \frac{1}{2} \sin^{-1} \left(\frac{-s_3}{m \cdot s_0} \right)$
Relative Phase (Charbonneau et al., 2010) and alpha angle (Espeseth et al., 2017)	$\delta = \frac{1}{2} \tan^{-1} \left(\frac{s_3}{s_2} \right), \quad \alpha = \frac{1}{2} \tan^{-1} \left(\frac{s_1 + s_2}{s_3} \right)$

The extracted features are presented in Appendix-B. These features were used for oil spill detection, as presented in the next section. Furthermore, these features and the oil slick regions are used to analyse properties of the oil slicks, and in computing the slick separability for each of the features (Section 4.6). Thereafter, a subset of these features are used to classify oil spills using Wishart and Gaussian based MLC methods (Section 4.7).

4.5. Dark Spot detection

In order to compare the detectability of oil slicks in different polarimetric features, the slicks were segmented from the image. An unsupervised segmentation method called extended polarimetric feature space (EPFS) was chosen for the segmentation (Doulgeris, 2013; Doulgeris & Eltoft, 2010). This segmentation method uses polarimetric and contextual information and segments the pixels with similar statistical information into identical clusters. An unsupervised method was suitable for oil spill segmentation because of little or sometimes no prior available information regarding the oil slicks in the SAR dataset.

Extended Polarimetric Feature Space (EPFS) segmentation

Segmentation was performed with and without applying incidence angle correction over the components of the covariance and coherency matrix, as mentioned in Section 4.3. There were three steps carried out in the EPFS segmentation method. In the first step, polarimetric features were selected on the basis of their data distribution and contrast between oil spills and water. It was ensured that the chosen features were normally distributed using the Shapiro-Wilk test for normality (Shapiro & Wilk, 1965). For this test, 5000 random data samples (without repetition) were used from each feature. A similar test of normality was conducted with the hybrid polarimetric features of RISAT-1 and dual polarimetric features TerraSAR-X datasets.

The second step involved clustering of the dataset using expectation maximization (EM) of Gaussian Mixture Models (GMM) method on the dataset. The theoretical details of the EM of GMM is described in

Appendix-A (Bishop, 2006). It was assumed that the features were described by a mixture of multivariate Gaussian models. The number of classes is a crucial input parameter of the algorithm. The details of the input parameters can be seen in Table 9. The number of classes (n) was chosen to be 3. This number was chosen after experimenting with various values of this parameter. It was ensured that the value of n remained closer to 2, signifying the two classes: oil and water.

Table 9: Input parameters for EPFS segmentation of UAVSAR, RISAT-1 and TerraSAR-X datasets

Parameter	UAVSAR (1)	UAVSAR (2)	RISAT-1	TerraSAR-X
Feature extraction window size	9×9	9×9	9×9	9×9
Incidence angle correction	Yes	No	No	No
Degree of sin correction function	1	-	-	-
Majority smoothening window size	35	35	50	10
Number of classes (n)	3	3	3	3
Maximum number of iterations	200	200	200	200
Tolerance	0.0001	0.0001	0.0001	0.0001

In the last step, a majority smoothening operator was applied to the dataset. This method improved the connectivity of the segments. Thereafter, the oil slick patches were manually chosen from the segmented output. The results of the segmentation can be seen in Figure 16.

4.6. Slick analysis and Feature Comparison

After the areas of the slicks were identified, the slicks were analysed and compared on the basis of their shape, size, their extent in the range direction, their dilution in the sea water and their response to the wind velocity. The motivation for doing so was to study the impact of wind and the occurrence of regular dark and bright linear in the datasets which suggested high surface gravity waves over the waves.

Moreover, the polarimetric features were compared on the basis of their ability to distinguish between oil slicks and water, and also amongst the four oil slicks. The features values for each slick were extracted using a mask of oil slick regions extracted from dark spot detection. Three regions (W_{near} , W_{mid} , W_{far} in Figure 17) in the water areas were selected and used for this comparison. These three regions of water were situated in the near range: W_{near} , mid-range: W_{mid} and far range: W_{far} . The basis for comparison was a class separability measure called Jeffries-Matusita (JM) (Equation 4.7) distance. The JM distance is derived using Bhattacharya distance ($B_{a,b}$). The symbols μ_α and C_α in Equation 4.7 represent the mean vector and covariance matrices of each class α respectively. This is in cases where the number of dimensions in the dataset are 2 or more. However, in this work, only one dimensional data (for each feature) was used for calculating the separability distance. Therefore, mean and variance of the ROI's for each features were used in the comparison of features instead of mean vector and covariance matrix. The values of JM distance ranges between 0 and 2, whereas the Bhattacharya distance varies between 0 and ∞ . For identical classes the value of JM and B are 0, which indicates that it is very difficult to distinguish between the two classes. However, larger

values of the similarity measures indicate towards higher potential of the feature to differentiate between the two classes.

$$B_{a,b} = \frac{1}{8}(\mu_a - \mu_b)^T \left(\frac{\mathbf{C}_a + \mathbf{C}_b}{2} \right)^{-1} (\mu_a - \mu_b) + \frac{1}{2} \ln \frac{\left| \frac{\mathbf{C}_a + \mathbf{C}_b}{2} \right|}{\sqrt{|\mathbf{C}_a| \cdot |\mathbf{C}_b|}}; \quad JM_{a,b} = 2(1 - e^{-B_{a,b}}) \quad (4.7)$$

The method chosen for comparison was Jeffries-Matusita (JM) distance, which is a measure of class separability (Tolpekin & Stein, 2009). The measure of JM distance were calculated by transforming the feature values from linear scale to log scale and hence calculating the JM distance between the slick feature values. The JM separability distance was then compared by changing the number of looks. The slicks, as seen in Figure 16 were used to mask out the pixels for various features as described in Section 4.4. A stack of masked features was created and used to calculate mean and variance of masked feature data values.

4.7. Oil Spill Classification

In this section, the UAVSAR MLC data was classified using supervised Wishart Maximum Likelihood Classifier (W-MLC) and Gaussian MLC (G-MLC). The aim of classification was to use the variation in the oil slicks and water areas to distinguish between the oil slicks. The method adopted for this purpose was to assign two classes in the training data and then use it in the algorithm to classify the image. The results from the two methods are reported in Section 5.6.

Training data for classification

The training areas used in the classification are depicted in Figure 9. For the oil class, a patch from each of the four oil slicks was chosen to be a part of the training set. The patches for water were taken on either side of the oil slicks, both in near range and far range so as to account for the variability of the water class due to incidence angle effect.

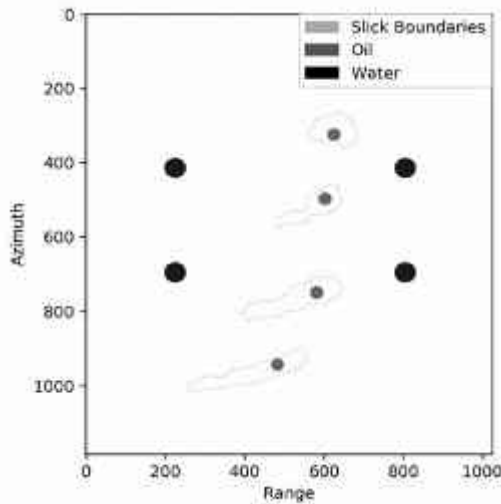


Figure 9: Training data for classes: Oil and Water

MLC with Gaussian likelihood term (G-MLC)

For comparison, results from a maximum likelihood classifier using a Gaussian likelihood term was used. The G-MLC result was calculated using the following equation.

$$\hat{x}_a = \arg \max \left\{ \frac{1}{\sqrt{2\pi}^\rho \sqrt{|\mathbf{C}_j|}} \exp \left(-\frac{1}{2} \times (\mathbf{x}_i - \boldsymbol{\mu}_j)^T \times \mathbf{C}_j^{-1} \times (\mathbf{x}_i - \boldsymbol{\mu}_j) \right) \right\} \quad (4.8)$$

where $\boldsymbol{\mu}_j$ and \mathbf{C}_j are the means and covariance matrices of the features values of the pixels overlapping in the training dataset. The features used in this classification were most suitable features derived from the feature comparison step.

MLC with Wishart likelihood term (W-MLC)

The complex Wishart distribution can be described by the following equation (Wu et al., 2008).

$$p^{(L)}(\mathbf{C}) = \frac{L^{qL} |\mathbf{C}|^{L-q} \exp(-L \text{Tr}(\boldsymbol{\Sigma}^{-1} \mathbf{C}))}{R(L, q) |\boldsymbol{\Sigma}|^L} \quad (4.9)$$

In the above equation, \mathbf{C} is the complex covariance matrix of the quad-pol SAR dataset, $\boldsymbol{\Sigma}$ is the ensemble average of \mathbf{C} , q is the number of polarimetric channels, $R(L, q) = \pi^{q(q-1)/2} \prod_{i=1}^{i=q} \Gamma(L-i+1)$ is the normalizing factor, $\Gamma(\cdot)$ is the gamma function and L represents the number of looks. The statistical model described by the training data is used for supervised ML. The estimation of the class labels of individual pixels was done using the following method.

$$\hat{x}_a = \arg \max \left\{ \frac{L^{qL} |C_a|^{L-q} \exp(-L \text{Tr}(\boldsymbol{\Sigma}_{x_a}^{-1} C_a))}{R(L, q) |\boldsymbol{\Sigma}_{x_a}|^L} \right\} \quad \text{where } x_a \in \{1, \dots, D\} \quad (4.10)$$

In the above equation, a represents a region over which the ensemble average of the covariance matrix is performed. These regions (a) were defined as squares of $m \times m$ pixels spanning over the entire image; \hat{x}_a denotes the class label calculated using Equation 4.10, D is the number of classes, C_a is the average covariance matrix of region a , and $\boldsymbol{\Sigma}_{x_a}$ represents the average covariance matrix of training data of class labelled by x_a . The initial parameters values of the Wishart classification algorithm are shown in Table 10.

Table 10: Input parameter values for Wishart Classification of UAVSAR dataset

Parameter	Value
Incidence angle normalization	No
Degree of sine function in incidence angle normalization	1
Number of classes	2 (Oil, Water)
$m \times m$ (size of square of region a)(unit: # of pixels)	5×5
Number of Looks	12 (azimuth) \cdot 3 (range) = 36
q (number of polarimetric channels)	3

Accuracy Assessment

The objective of performing accuracy assessment is to assess the credibility of the classified output. The overall accuracy (OA) was calculated from the confusion matrices from G-MLC and W-MLC classification outputs. The accuracy was calculated by comparing the classified output to the reference data. Moreover, the user's accuracy (UA) and producer's accuracy (PA) were also calculated. UA signifies the error of incorrect assignment of a label to a particular class. PA signifies the error of failure of assignment of a correct label to a class. Moreover, the classified outputs are also analysed visually to compare the results of the methods used.

4.8. Probability Surface Modelling

The soft probability output from Wishart based MLC was used for fitting the Gaussian probability surfaces to the regions of oil spill. The soft probability output was generated by normalizing modulus of the Wishart distance by the maximum distance in the entire scene. The probability image was spatially averaged using various window sizes. The probability of the occurrence of oil class for each of the 4 slicks was extracted from the above output using the masks PO, E40, E60 and E80, which were computed using EPFS segmentation.

Surface Model

The oil spills were modelled as elliptical objects with the parameters of the ellipses computed by fitting two dimensional Gaussian surfaces (Equation 4.11) to the probability values of pixels lying within the extent of the slicks (Ardila, 2012). The equation used for this Gaussian fitting is

$$\text{Prob}(x, y) = I \exp \left[-\frac{1}{2} \left(\left(\frac{x'}{\sigma_x} \right)^2 + \left(\frac{y'}{\sigma_y} \right)^2 \right) \right] \quad (4.11)$$

where, $\text{Prob}(x,y)$ is the pixel-wise probability of oil class calculated using Wishart classification, I is the maximum height of the Gaussian surface, σ_x and σ_y are the standard deviations along the two axes of the Gaussian surface. The axes (x', y') are rotated about the horizontal and vertical axes (x, y) axes by an angle θ in the anticlockwise direction, and are defined as:

$$x' = (x - x_0) \cos(\theta) - (y - y_0) \sin(\theta) \quad (4.12a)$$

$$y' = (x - x_0) \sin(\theta) + (y - y_0) \cos(\theta) \quad (4.12b)$$

The centre of the Gaussian was chosen to be at the point with maximum probability within each slick region. The regions were defined using oil slick regions extracted using EPFS segmentation (Figure 16). The oil probabilities were spatially averaged with five different window sizes in order to smoothen the image and reduce the value or the counts of local minima. This smoothened oil probability data was then used for estimating the parameters of the Gaussian model. The initial values for the parameters were kept constant for all slicks and for all window size operations. The window sizes were chosen by taking into account that they were odd in number and by ensuring that they didn't oversmoother the image. The oversmoothering of the oil probability image was judged by comparing its spatial extent with the extent of the slick boundaries.

The next chapter presents the results derived after executing the above methods and also presents the analysis of the results.

5. RESULTS AND ANALYSIS

5.1. Scattering mechanism of sea surface

UAVSAR polarimetric analysis

Pauli Decomposition

The Pauli decomposition of the UAVSAR dataset mentioned in Section 4.2 is displayed in Figure 10. The modulus of the coefficient α represents the amplitude of the backscatter of targets characterised by odd or single bounce scattering. The coefficient β represents the backscattered amplitude of targets which are characterized by double or even bounce scattering, since the polarization of the received wave from such targets is mirrored with respect to the incident wave. The coefficient γ characterizes the targets which return backscatter with polarization orthogonal to the incident wave. This type of scattering is termed as volume scattering. In the RGB composite of the Pauli decomposed image (Figure 10), a gradually varying trend of scattering mechanism can be observed. This variation is from odd bounce scattering in the near range to volume scattering in the far range. This gradual change may be caused either due to change in the scattering mechanism of targets situated in the near and far range, or due to the changing imaging geometry from the near range and the far range. The gradual change indicates that this variation may be due to the high incidence angle difference between the near range and the far range. However, the oil spill regions can be observed as dark patches which show relatively low backscatter for all the three components of the Pauli decomposition.

Interestingly, similar dark response were observed in regular wave-like small patches running obliquely from the top right to the bottom left of the image. These dark patches may be due to the swell of the ocean. As mentioned in Section 3.1, the conditions of the sea were rough, because of which the height of the sea waves was relatively high, ranging from 2 to 2.5m (Table 2 in Jones et al. (2016)) during the course of the day. The swell of the ocean was from the north-west direction. These dark patches are aligned in the direction of the ocean swell. Therefore, these aligned dark patches may have resulted from troughs of the ocean waves. These patterns cause confusion between and oil slicks and water areas, as shown in the later sections.

Freeman-Durdan Decomposition

The result of the Freeman decomposition is displayed in Figure 11. The RGB composite suggests that the surface scattering is dominated in the near range. The nature of scattering gradually varies from surface scattering in the near range towards volume scattering in the far range. The dark patches caused due to oil slicks and ocean swell are also clearly visible in the result. These dark patches are also observed in Figure 10, which represents Pauli decomposition of the SAR image. On a closer look on the decomposition components of the image, we can observe very low double bounce scattering as compared to surface and volume scattering. This result is in agreement with the results of Pauli decomposition which also suggest higher single bounce scattering in the near range of the scene.

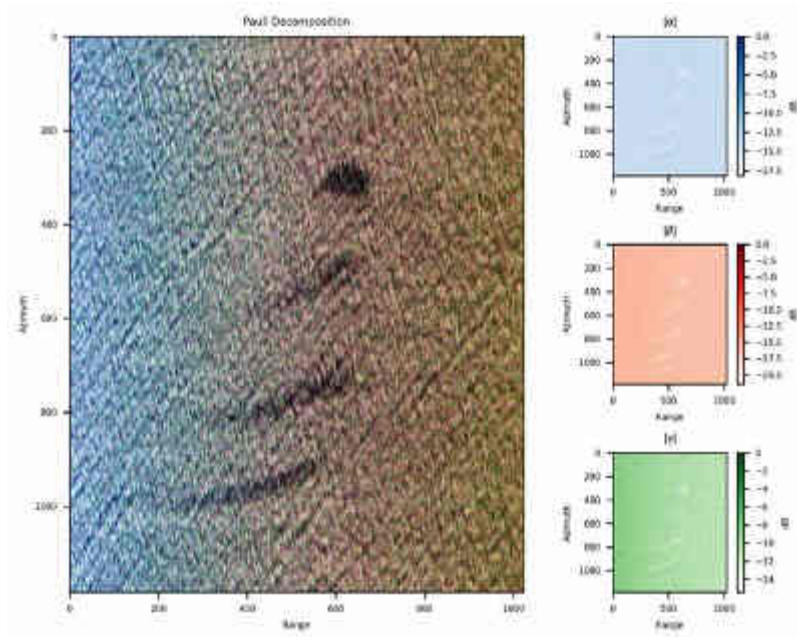


Figure 10: Pauli Decomposition: RGB composite (left) of the components of the scattering matrix decomposed in Pauli basis as mentioned in Section 5.1. Colour code – Red : $|\beta|$, Green: $|\gamma|$, Blue: $|\alpha|$. Near range is to the left of the image.

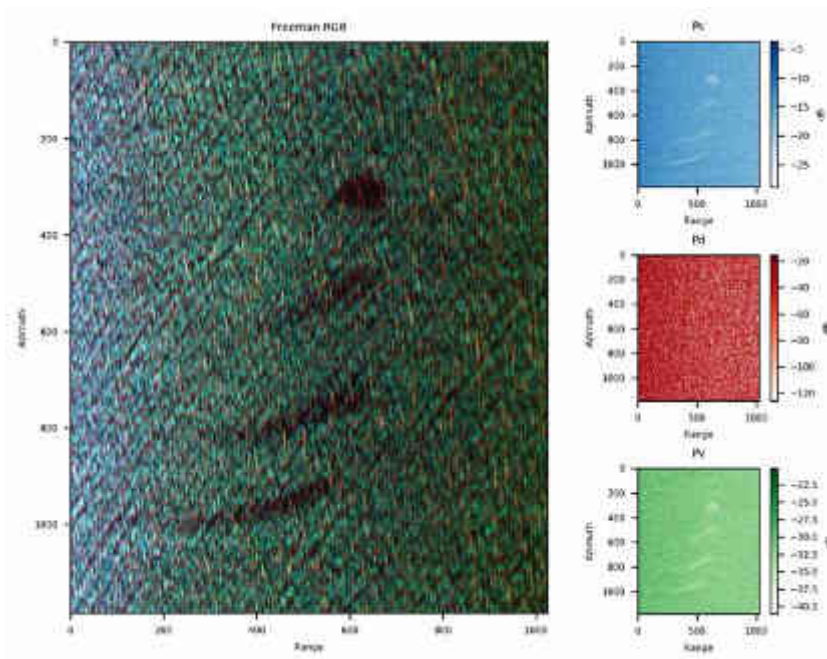


Figure 11: Freeman decomposition of UAVSAR dataset. The RGB composite (left) of the components of the decomposition as described in Section i.e. P_s , P_D , P_V (right) is displayed. Colour code - Red: P_D , Green: P_V , Blue: P_S

RISAT-1 polarimetric analysis

The results of $m\text{-}\chi$, $m\text{-}\delta$ and $m\text{-}\alpha$ decomposition methods are displayed in Figure 12. The $m\text{-}\chi$ and $m\text{-}\alpha$ decomposition suggest dominant double bounce scattering in the far range, and double bounce scattering in the near range. However, the result from the $m\text{-}\delta$ decomposition suggests that there is dominant surface

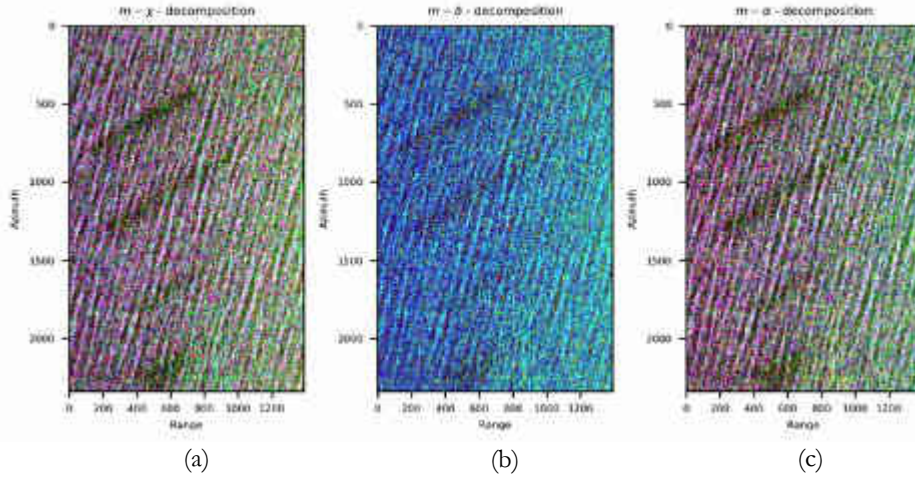


Figure 12: RGB composites from $m\text{-}\chi$ (a), $m\text{-}\delta$ (b) and $m\text{-}\alpha$ (c) decomposition of RISAT-1 RH and RV channels. Color code: Blue: Surface scattering, Red: Double bounce scattering, Green: Volume scattering.

scattering over the oil and water surface. This result from the $m\text{-}\delta$ decomposition seems more plausible because of dominating surface scattering over water. Interestingly, the oil slicks appear as dark spots in all the three images indicating the smooth nature of scatterers over the surface of oil spills. Moreover, radar shadows due to high sea surface gravity waves can be observed in the RGB composites of $m\text{-}\chi$, $m\text{-}\delta$ and $m\text{-}\alpha$ decompositions.

5.2. Preprocessing

UAVSAR incidence angle correction

Incidence angle normalization was performed in order to counter large variations between the backscatter values of similar scatterers situated in near and far range. The methodology adopted for this method is described in Section 4.3. Transects along 10 rows about scan line number 500 of the MLC image (Figure 8) before and after the application of incidence angle normalization is depicted in Figure 13. The method is able to reduce the backscatter for incidence angle less than the mean incidence angle (θ_{ref}) (42° - 48°) and increase it for incidence angles larger than θ_{ref} . The effectiveness of incidence angle correction in oil spill detection and characterization is studied in Section 5.4. On a closer look, this method of incidence angle correction brings down the dependence of backscatter to a little degree but not to a very large extent.

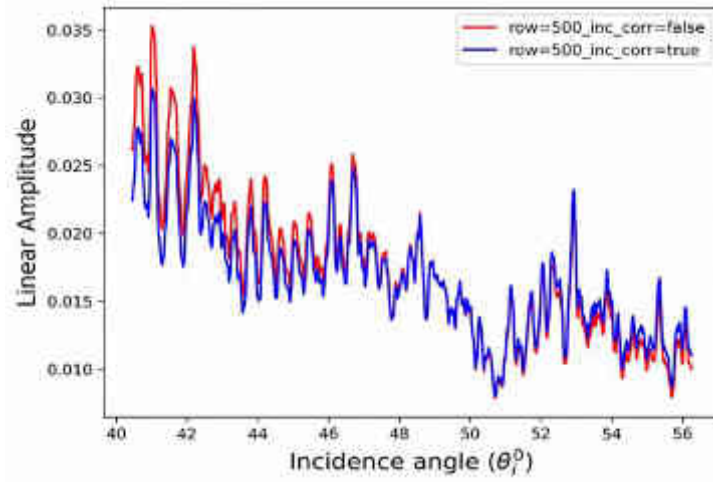


Figure 13: Incidence angle normalization. A transect plot of row number 500 of UAVSAR MLC image (Fig. 8) before (red), and after (blue) applying incidence angle normalization.

5.3. Feature Extraction

The extracted UAVSAR fully-polarimetric features, RISAT-1 compact polarimetric features and TerraSAR-X dual-polarimetric features are displayed in Appendix-B. It was observed that only a few features provided a reasonably good contrast between oil slicks and open water. From the set of UAVSAR features, λ_1 , λ_2 , λ_3 , PD, $\det(C_{FP})$, I_{HH} , I_{VV} , I_{HV} , r_{CO} and i_{CO} clearly distinguish oil slicks from open water. From RISAT-1 data, λ_1 , $\det(C_{HP})$, H, S_0 , DoP, power ratio, and conformity coefficient were the best chosen features for further analysis. The span of covariance matrix, λ_1 , λ_2 , $\det(C_{DP})$, I_{HH} , I_{VV} , GI, and PD provided good identification of oil slicks from the TerraSAR-X dataset. A summarized view of the above information can be seen in Table 11.

Table 11: UAVSAR, RISAT-1 and TerraSAR-X polarimetric features (Appendix-B) with high contrast between and water (on the basis of manual inspection of features)

	λ_1	λ_2	λ_3	PD	$\det(C)$	I_{HH}	I_{VV}	I_{HV}	r_{CO}	i_{CO}	GI	S_0	DoP	H	μ_{CO}	$\mathcal{Y}_{RV/RH}$
UAVSAR	✓	✓	✓	✓	✓	✓	✓	✓	✓	✓						
RISAT-1	✓			✓								✓	✓	✓	✓	✓
TerraSAR-X	✓	✓		✓							✓					

5.4. Dark Spot detection

This section summarizes the results of EPFS segmentation method over the UAVSAR dataset. The first step of this procedure was to analyse and choose the features which were distributed normally. The histograms of 10 polarimetric features, λ_1 , λ_2 , λ_3 , PD, $\det(C_{FP})$, I_{HH} , I_{VV} , I_{HV} , r_{CO} and i_{CO} and 5 GLCM contextual features

(Table 7), whose values are normalized between $[0,1]$ are displayed in Figure 14. These features provide the best contrast between the oil slicks and open water, as described in the previous section. Each of the features were passed through the Shapiro-Wilk test of normality. The test statistic of the test is tabulated in Table 12. It can be observed from Figure 14 and Table 12 that λ_3 , PD and $g_{\text{LCM}_{\text{DIS}}}$ are closer to a Gaussian distribution as compared to the other features. Therefore λ_3 , PD and $g_{\text{LCM}_{\text{DIS}}}$ were chosen for the next stage of the segmentation algorithm. For the segmentation of the RISAT-1 dataset, the determinant of the covariance matrix and entropy were selected for segmentation.

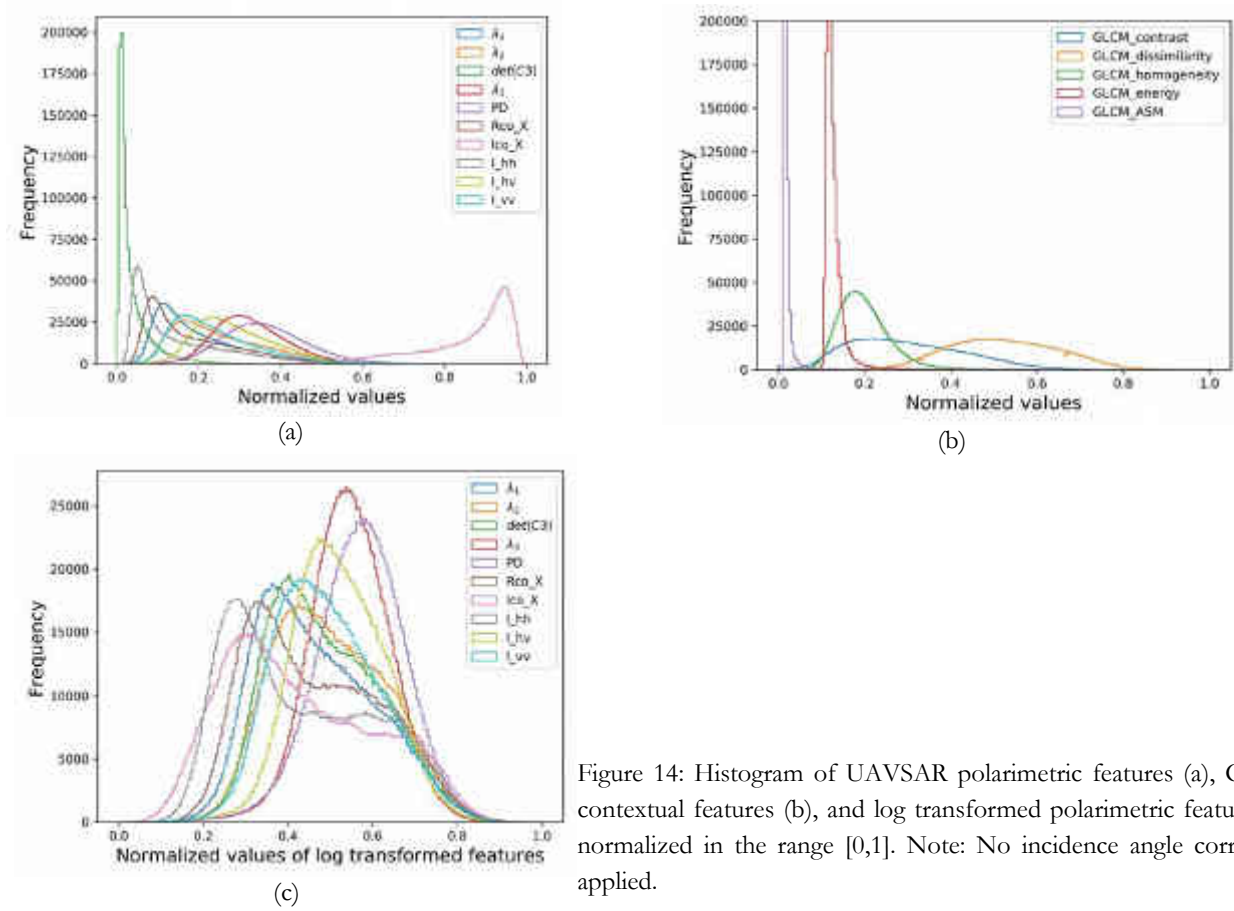


Figure 14: Histogram of UAVSAR polarimetric features (a), GLCM contextual features (b), and log transformed polarimetric features (c) normalized in the range $[0,1]$. Note: No incidence angle correction applied.

Table 12: Results from Shapiro-Wilk test of normality for each of the linear UAVSAR polarimetric feature (a) and GLCM features (b) (5000 data points per feature). W represents the test statistic

(a)	Features	λ_1	λ_2	λ_3	PD	$\det(C)$	r_{CO}	i_{CO}	I_{HH}	I_{HV}	I_{VV}
	W	0.92	0.96	0.99	0.99	0.73	0.92	0.87	0.87	0.98	0.95

(b)	Features	$g_{\text{LCM}_{\text{CON}}}$	$g_{\text{LCM}_{\text{DIS}}}$	$g_{\text{LCM}_{\text{Hom}}}$	$g_{\text{LCM}_{\text{Energy}}}$	$g_{\text{LCM}_{\text{ASM}}}$
	W	0.97	0.99	0.88	0.45	0.24

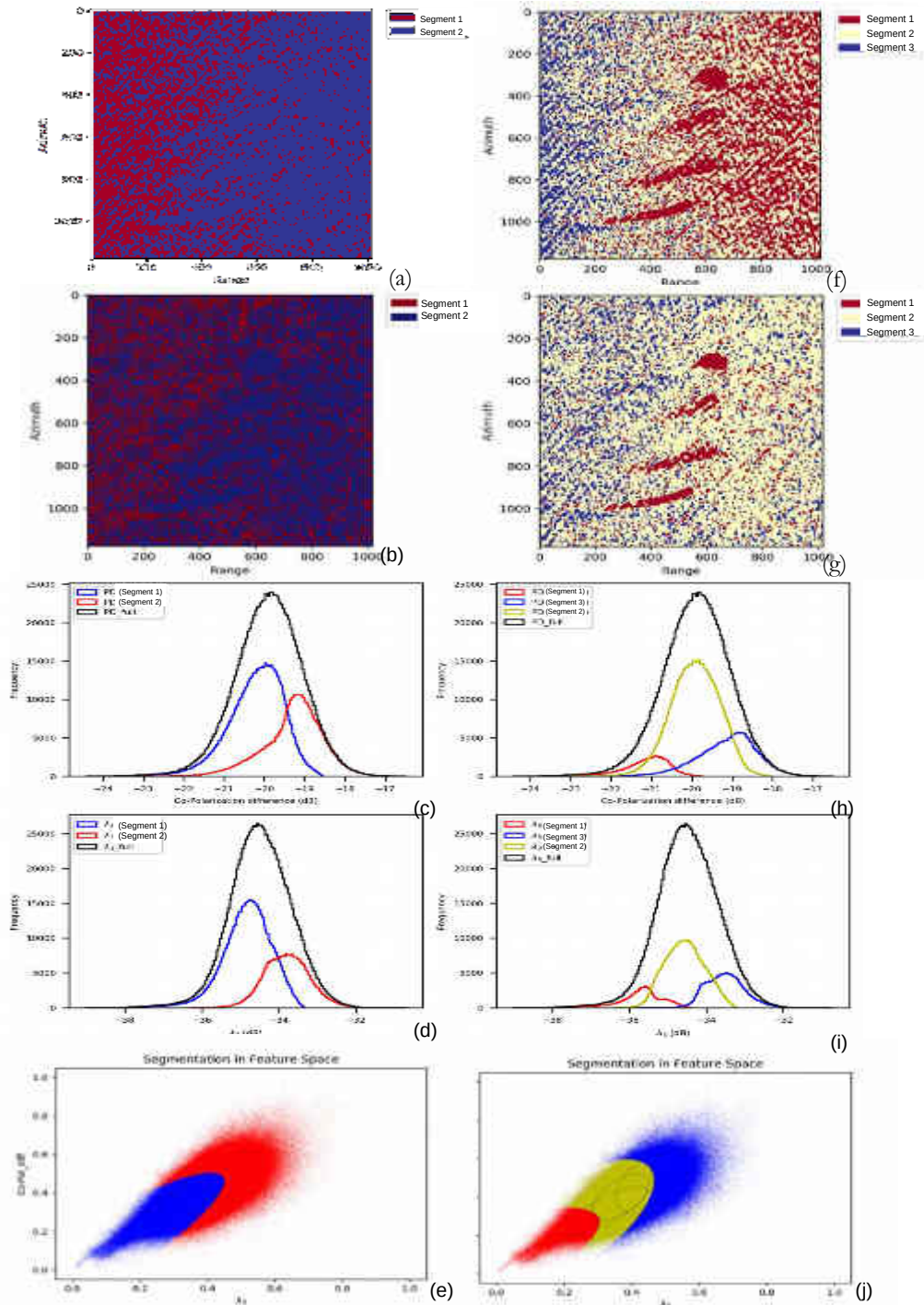


Figure 15: Segmented outputs for number of segments = 2 (left column) and segments = 3 (right column). (b) and (g) depict an improvement in the quality of oil spill detection over (a) and (f) respectively. An incidence angle normalization is applied to the features in case of (b) and (g). (c) and (h) represent the class-wise and the full-feature histogram of PD. (d) and (i) represent the class-wise and the full-feature histogram of λ_3 . (e) and (j) represent the scatter-plot between λ_3 and PD with the colours representing the segments after segmentation.

Figure 15 shows the results after the second stage of EPFS segmentation using number of segments (n) = {2, 3} (left and right column respectively). The effect of IAC can be observed from the first row (IAC not applied) and the second row (IAC applied). The IAC reduced the number of false identifications of oil segment in the far range where the radar backscatter was lower in comparison to the near range for the same water class. The third and the fourth rows represent the full-feature and class-wise histograms of IAC corrected PD and λ_3 features respectively. After visualizing Figure 15 (a) and (b), it was hypothesized that the segment represented by blue could further be subdivided into two sub segments. This hypothesis was developed on the basis that the condition of the sea during image acquisition was rough, which led to high sea waves. The slant imaging geometry of the sensor might have led to the shadowing due to high sea surface gravity waves. These shadows might have mixed with the dark oil slick regions. Therefore, n was further chosen to be $n = 3$. Figure 15 (d and i) depict further subdivision of segment 2 (for $n = 2$) into 2 separate segments (segment 1 and 3 for $n = 3$). Figure 15 (e and j) represent the feature space plots between PD and λ_3 for $n = 2$ and $n = 3$ respectively. The colours in the scatter-plot represent the corresponding segments in the images Figure 15 (a, b, f and g). The plot suggests that lower feature values or dark spots characterize the oil spill segments. This plot also shows that $n = 3$ is more suitable than $n = 2$ to segment oil slicks from open water, especially in the presence of rough sea conditions. Therefore, for further analysis, the result with $n = 3$ is chosen.

In the final step, a majority smoothing convolution operation is applied on the segmented image. Multiple window sizes are tried in order to connect the region, by carefully avoiding over-smoothing of the image. Finally a window size of 35×35 is chosen for the smoothing operation. The output of the segmentation is displayed in Figure 16. The 4 oil slicks are clearly segmented in the case of UAVSAR dataset. However, application of the same algorithm on the RISAT-1 dataset (with chosen features for EPFS as DoP and H) and TerraSAR-X dataset doesn't return results as good as in the case with the UAVSAR dataset. This could be due to the difference in the frequency of the L band UAVSAR, X-band TerraSAR-X and C-band RISAT-1 dataset. In Appendix-A, the result of applying the same algorithm on a time series of UAVSAR datasets with different number of components is reported.

For slick analysis and feature selection, the oil slick region and oil slick boundaries are extracted.

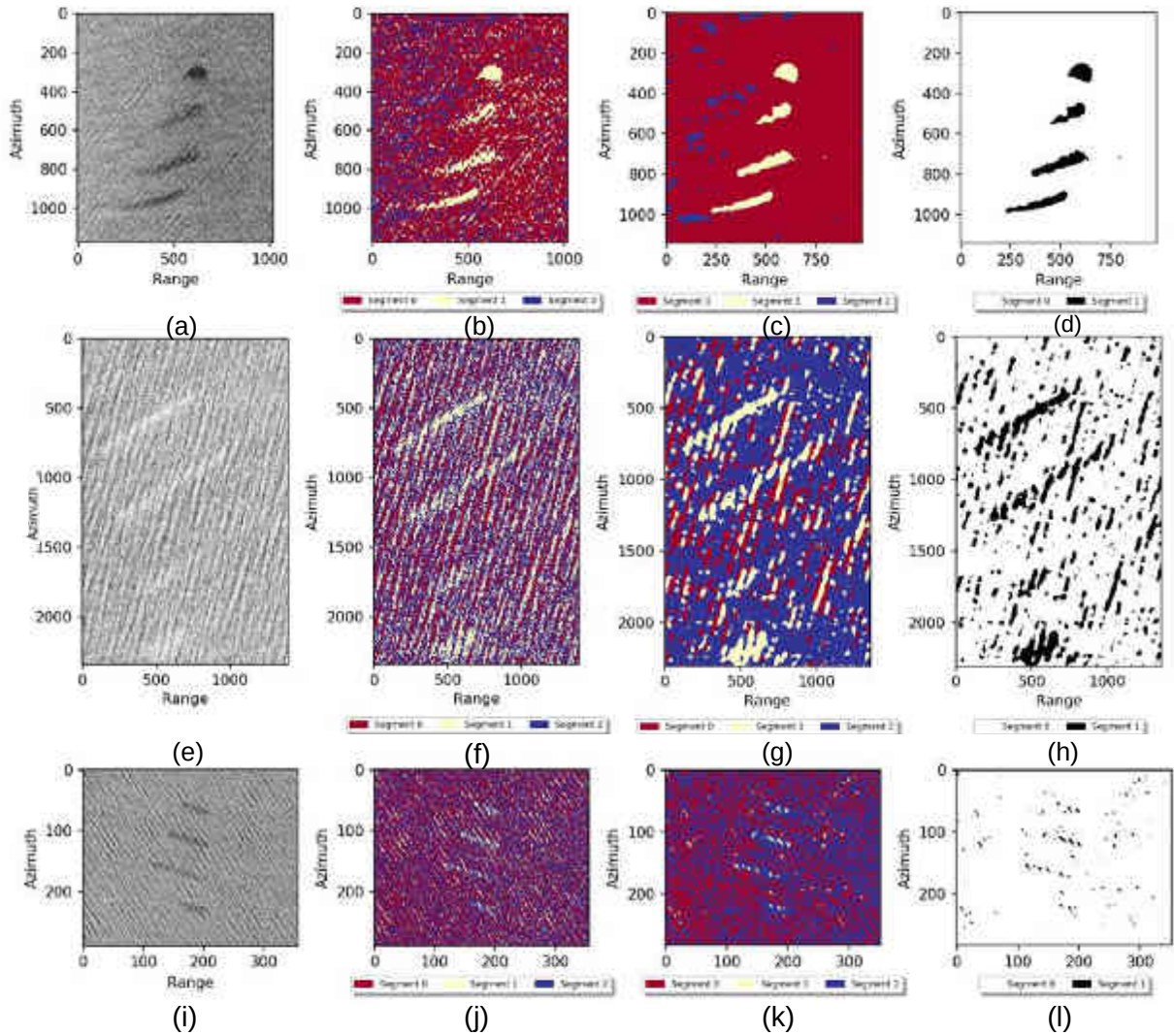


Figure 16: Slick segmentation: The results of slick segmentation on the UAVSAR (first row), RISAT-1 (second row) and TerraSAR-X (third row) images. The first column shows a polarimetric feature for reference, the second column shows segmented images after applying EPFS, the third column shows the segmented slicks after applying majority smoothing, and the last column shows the oil slick and water regions displayed in black and white.

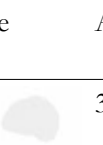
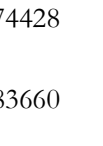
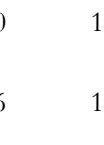
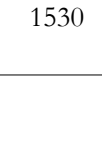
5.5. Slick analysis and Feature Comparison

Slick Analysis

The four oil slicks extracted from the UAVSAR image after performing EPFS segmentation are displayed in Figure 17. This figure also represents three more open water regions which are manually drawn so as to compare feature values between oil spill and open sea regions. The shape of the slicks has been affected by various factors, but mostly by their interaction with wind. As mentioned in Section 2.4.1, mineral oils are more influenced by the flow of wind over their surface as compared to biogenic oils. Table 13 describes the

shape, area and extent in the range direction and the proportion of the extent of mineral oil relative to slick E40. It can be observed that the extent of the slicks increases from E40 to E80 and are also proportional to the concentration of oil in the slicks. As the concentration of oil in the emulsions increases, the slicks become more susceptible to move over the water surface in the direction of wind (Alpers et al., 2017). However, simulated plant oil (PO) shows a smaller spread in the direction of wind.

Table 13: Shape, drift, size and extent of oil slicks. The last column shows the relative extent of oil mineral oil spills with respect to the E40 slick.

Slick name	Shape	Area (m ²)	Slant range extent (m)	Mineral oil extent proportion (to E40)
PO		300312	615	-
E40		274428	800	1
E60		483660	1315	1.64
E80		454356	1530	1.91

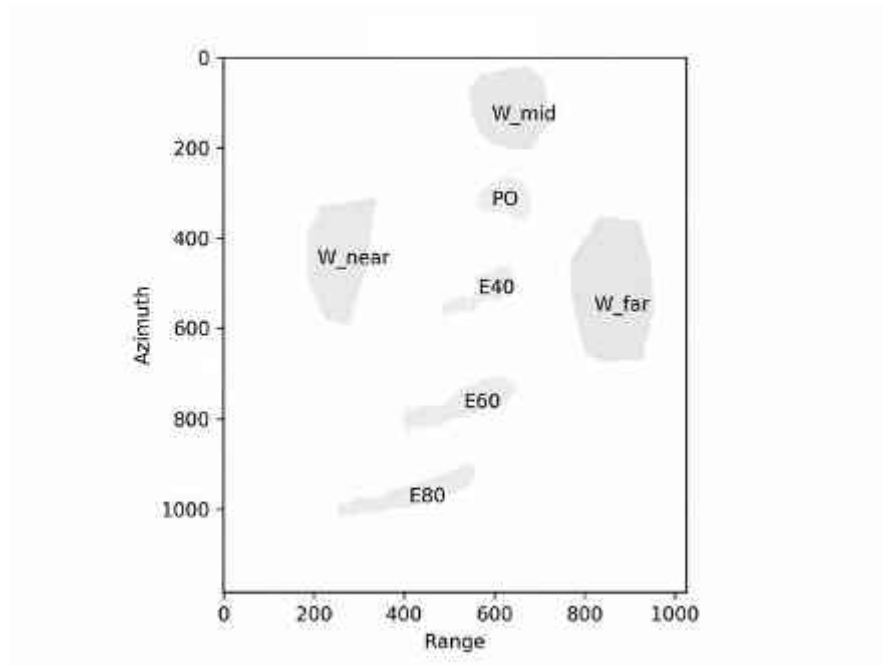


Figure 17: Oil slicks and 3 other water regions used for comparison of polarimetric features

Feature Comparison

The mean and variance of the slicks for number of looks equal to 1, is displayed in Figure 18. A general trend visible from the figure is that the water region in the near range i.e. 'W_near' has the highest value for each of the features except for PD, which is something to be expected because of higher backscatter from near range and from water regions. It can also be observed that the water regions have higher features values as compared to the oil slick regions, with the only exception being the feature I_{hh} which shows values for water in far range even lower the values of few oil slicks. It is also important to notice the relatively low feature values for $\det(C3)$. It also shows the largest difference between oil and water regions. These regions were also used to calculate and compare the separability between slicks for different features. The separability between slicks can be seen in Figure 19. The plots indicate that the determinant of covariance matrix stands out as the best feature in distinguishing oil slicks from open water.

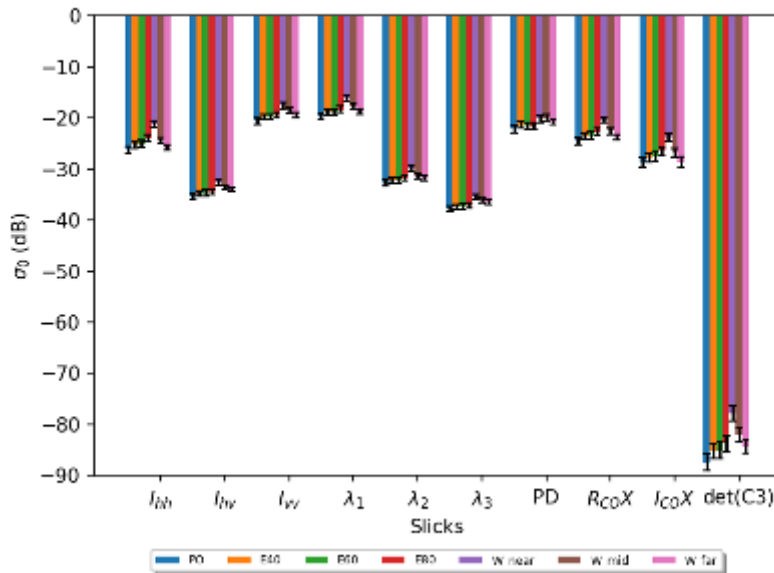


Figure 18: Mean and variance of features for the oil slicks and water regions as shown in Figure 17. The data has been plotted with number of looks for features = 1.

The eigen-values of coherency matrix, which showed good contrast between oil slicks and open water while performing slick segmentation, provide moderate separability between oil slicks and water. The separability increases from λ_1 to λ_3 for water regions in the near range and from λ_3 to λ_1 in the far range. Moreover, it can be seen that the separability generally reduces as we move from the near range to the far range. In each of the three subplots in Figure 19, PO is the best separable slick from water regions as compared to E40, E60 and E80. It is very interesting to note that in Figure 20, where the plot between class separability between plant oil PO and open water class in the near range, and number of looks over the MLC product of UAVSAR has a maximum for number of looks = 1. This trend is similar for almost all features

except for $\det(C_{FD})$. This finding suggests that speckle may hold information to distinguish oil slicks from open water.

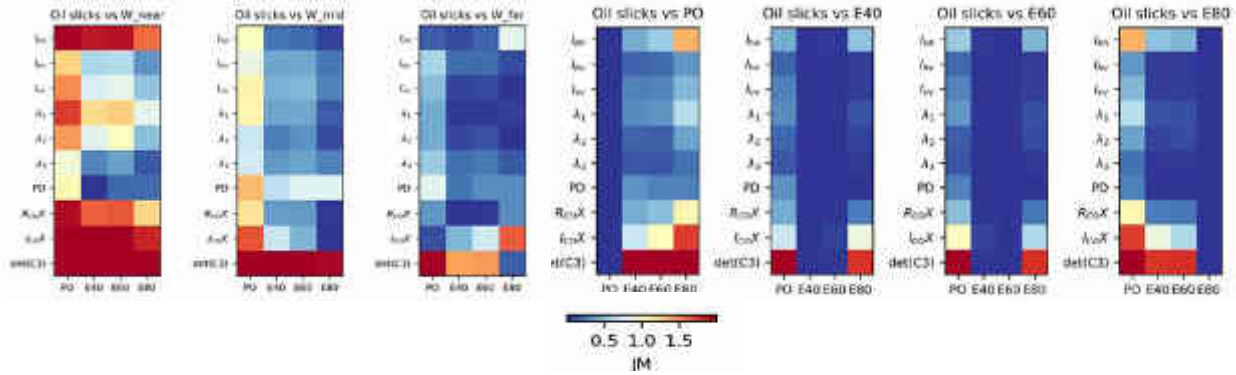


Figure 19: Class separability between oil slicks and open water regions for 10 different polarimetric features. JM = Jeffries Matusita distance. Number of looks = 1. The first three figures depict the separability of oil slicks with the three water regions, whereas the latter four figures show the separability of each oil slick from all oil slicks.

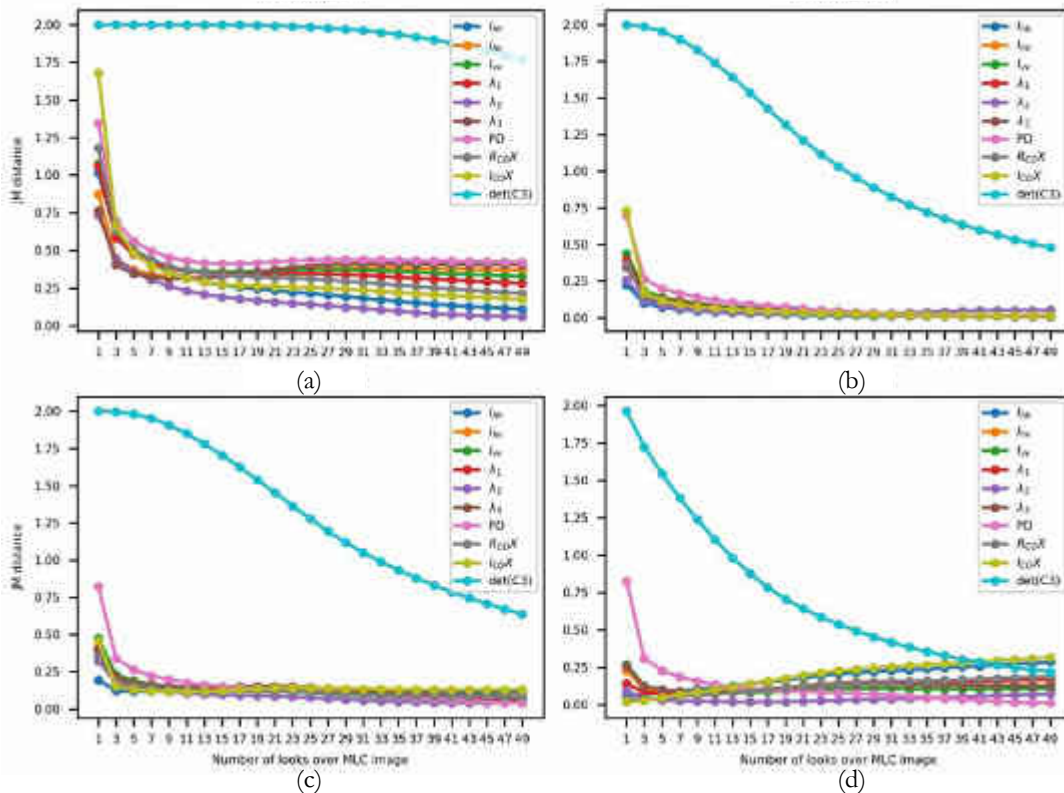


Figure 20: Jeffries-Matusita distance between W_mid and (a) PO, (b) E40, (c) E60 and (d) E80 as a function of edge of spatial averaging window. This averaging window is used to spatially average the features. The figure shows that class separability is higher for smaller window sizes, indicating that speckle noise may be useful for oil spill detection.

5.6. Oil Spill Classification

The results of Wishart-MLC classification and Gaussian-MLC are depicted in Figure 21. It can be seen from Figure 21(f) that in W-MLC, there are no misclassifications in the near range for the water class area, and fewer misclassifications in the far range water class areas as compared to the G_MLC result in Figure 21(c). However, on a closer look of the W-MLC result, a trade-off between accurate predictions of Water class in the near range and Oil class in the areas of oil slicks can be observed (Figure 21(f) and 23). The Gaussian-MLC predicts the Oil class accurately for the oil slick regions, but with large number of misclassification of Water class in both near and far range. The oil probability output (Figure 23) from W-MLC is used to plot a two dimensional (2D) Gaussian surface by fitting 2D Gaussian models to the probability values for each slicks.

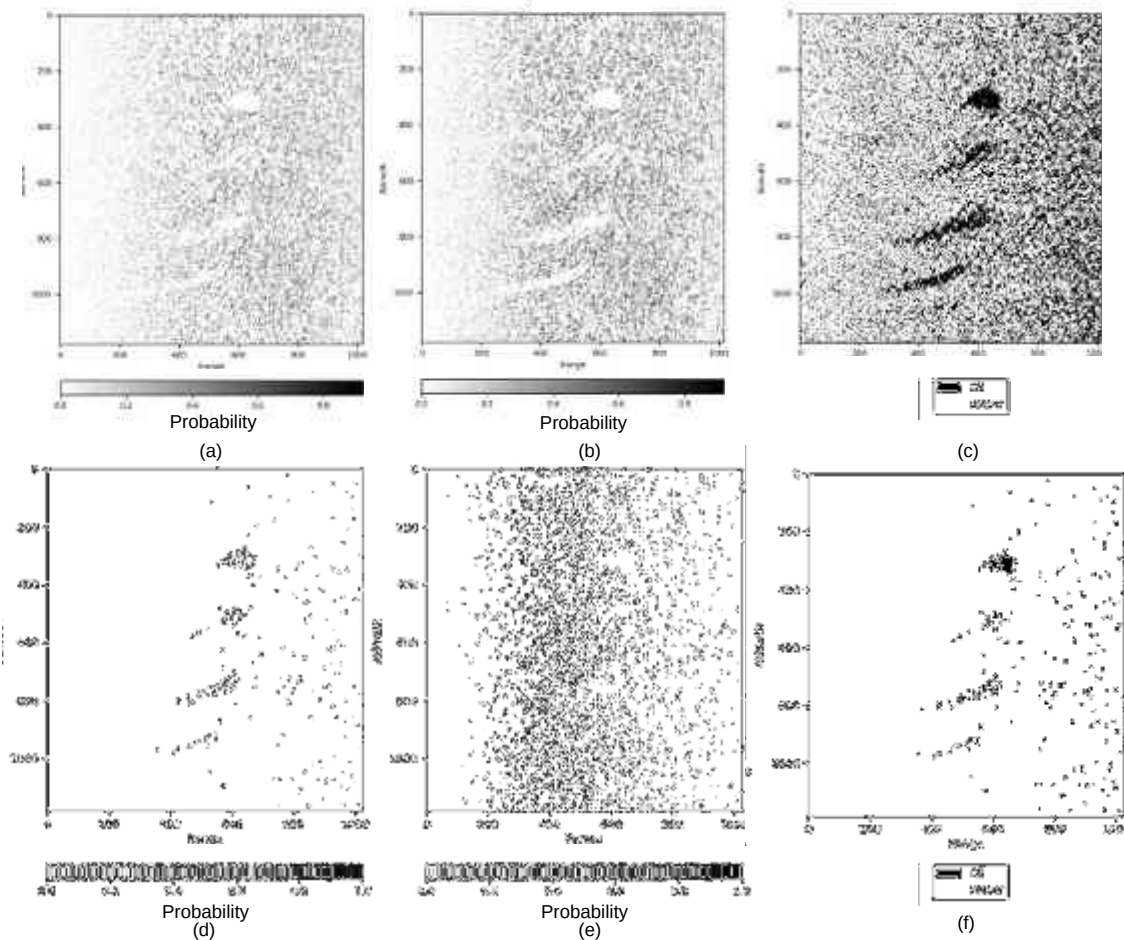


Figure 21: Gaussian-MLC (1st row) and Wishart MLC (2nd row): (a,d) Soft MLC - Oil, (b, e) Soft MLC - Water, (c, f) Hard MLC output.

Accuracy Assessment

After analysing the classified outputs from Figure 21, it can easily be concluded that the result from Wishart-MLC is more accurate than the result from G-MLC. The overall accuracy (OA) of W-MLC was found to be 78.89% whereas the OA of G-MLC by using all features mentioned in Table 12 (a) except co-polarization cross product, is found to be 62.17%. Furthermore, G-MLC using only $\det(C3)$ as a single feature resulted in the OA of 44.14%.

5.7. Probability Surface Modelling

The results from probability surface modelling of the oil probability map are reported in this section. The oil probability image is spatially averaged using various window sizes in order to reduce the local minima, and improve the results of Gaussian fitting. This smoothing effect can be observed in Figure 22 (smoothing window size = 41×41) where the probability values are spread much more evenly as compared to the case of no spatial averaging (Figure 21(d)). It can be observed from Figure 24, that increasing the window size of the smoothing operator on the oil probability image results in better estimation of the shape of the slicks.

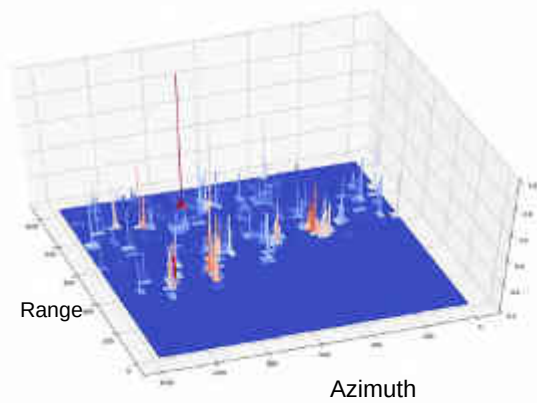


Figure 23: Probability Surface of probability for oil class from W-MLC classification

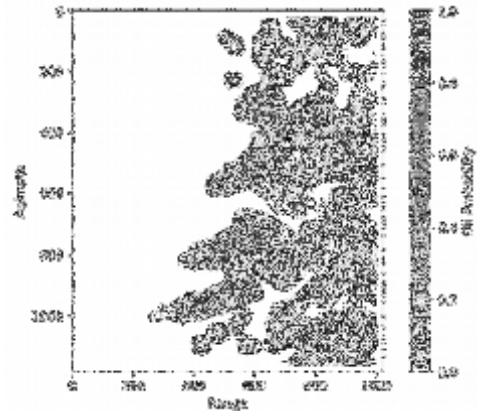


Figure 22: Oil slick masks and oil probability used for Gaussian surface Fitting (window size: 41×41)

Table 14: Parameters of Gaussian surface fitting for no spatial averaging and spatial averaging with window size = 31×31 of the oil probability output from Wishart MLC classification

Slick Type	Max Probability	Center of Gaussian Model (X,Y)	I	θ (radians)	σ_x, σ_y
No spatial averaging					
Initial Values			0.5	0.04	1, 1
PO	0.37	614, 323	0.09	3.27×10^6	54.07, 10.6
E40	0.32	542, 562	0.45	1.90×10^6	2.12, 1.77
E60	0.49	526, 782	0.68	1.61×10^6	1.81, 1.90
E80	0.36	512, 928	0.44	2.13×10^6	1.83, 3.99
Window Size = 31×31					
Initial values			0.5	0.04	1, 1
PO	1	618, 319	0.84	1.11×10^6	46.07, 27.93
E40	0.78	610, 493	0.63	8.87×10^5	39.06, 17.46
E60	0.64	546, 760	0.54	7.37×10^5	98.4, 22.4
E80	0.60	472, 948	0.46	6.70×10^5	15.2, 72.1

Probability contours:

The oil spill regions and the Wishart probability regions are displayed in Figure 24. The estimated values of the parameters of the Gaussian models (for no spatial averaging and window size 31×31) fitted over each slick regions are listed in Table 14. The areas of the slicks are directly related to the estimated variances of the fitted Gaussian model. An increase in the window size of the spatial smoothing operator results in an increase in the variances of the Gaussian model and thereby result in increase of the estimated area of the slicks (last column of Tables 14).

Orientation of slicks

Another interesting point to notice is that the Gaussian model is able to accurately predict the orientation of the slicks which have developed in the direction of wind over the course of approximately 6 hours.

Relation of probabilities to concentration of slicks

If we consider the output from window size = 41×41 (Figure 24 (f)), the probability of oil detection is highest for PO. In case of mineral oils: E40, E60, and E80, the Gaussian model correctly estimates higher possibility of oil class in E60, rather than E80 which may have been because of fewer number of probability pixels overlapping in E80, as compared to other slicks.

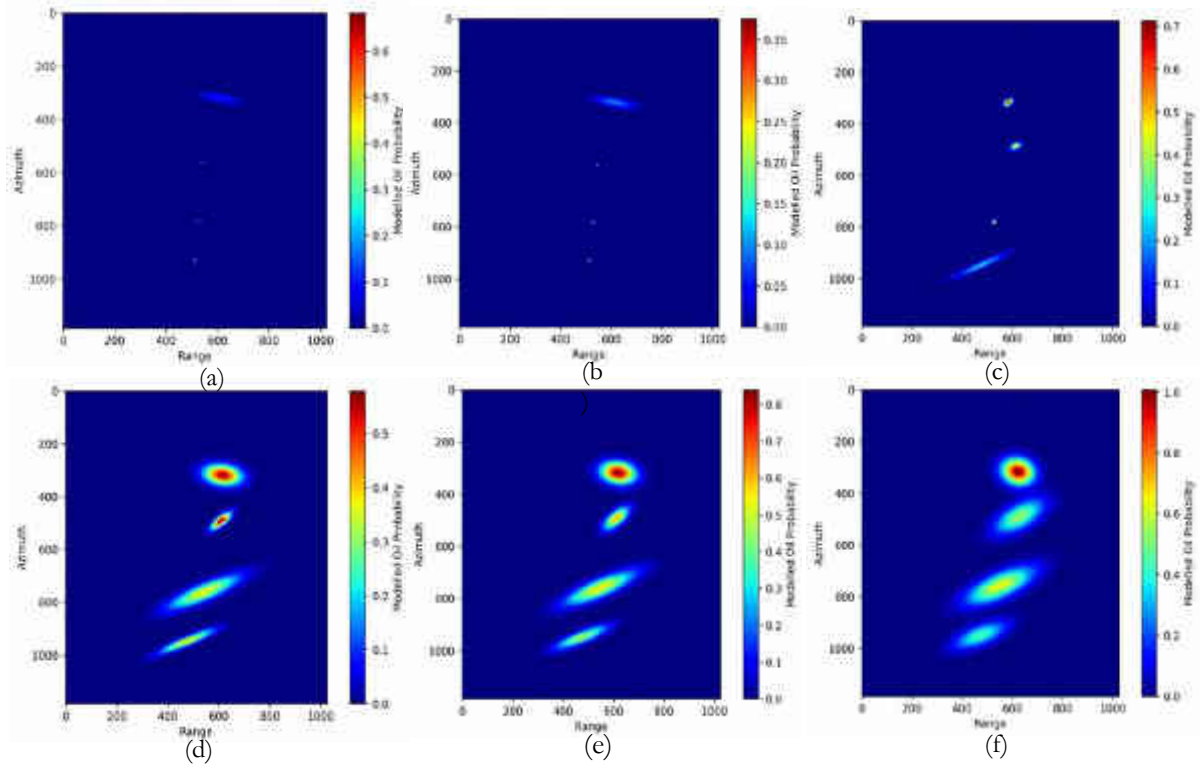


Figure 24: Contour plots depicting the regions of Gaussian models fitted over spatially averaged oil probability data from Wishart classification. The subplots show fitted regions for different window sizes: (a) No spatial averaging, (b) window size of 5×5 , (c) 11×11 , (d) 21×21 , (e) 31×31 , (f) 41×41

A discussion on the results and analysis is presented in the next chapter.

6. DISCUSSION

In this chapter, a discussion on the analysis of the results reported in the previous chapter and a brief summary of the methods used is presented. The findings are compared to existing research in some cases.

Scattering Mechanism

The scattering of radar waves off the surface of water and oil is usually modelled using Bragg scattering, as stated in chapter 2. However, in this study, we have explored the use of fully polarimetric decomposition methods, such as Pauli and Freeman decomposition, and hybrid polarimetric based m - χ , m - δ and m - α decompositions (Section 5.1) to characterize the scattering mechanism of the sea surface. From the results of both Pauli and Freeman decomposition, we can observe that the near range is characterized by dominant surface scattering and as we move from the near range to the far range, volume scattering becomes more dominant than surface scattering, resulting in high volume scattering in the extreme far range of the scene (Figure 10 and 11). It is quite common for surface of water bodies to be characterized by surface scattering (Freeman & Durden, 1998). However, in certain cases, incidents of volume scattering over the sea surface have also been reported. An example of such a situation is presented in Alpers et al. (2016), where wave breaking and rainfall were found to be responsible for volume scattering off the sea-surface. In the NORSE-2015 exercise, the environmental conditions were rough (Table 5), which would have led to the breaking of sea waves and hence, resulting in volume scattering. Moreover, from a satellite's viewing geometry's perspective, the increase in the look angle from the near range and the far range (Figure 4) might have resulted in an increase in the number of interactions of the incident and backscattered EM wave with sea surface gravity waves. Therefore, for higher incidence angles, there may have been more interactions between incident (and backscattered) EM waves and sea surface waves, which would also have been responsible for high volume scattering in the far range.

This gradual variation in the scattering mechanism has also been noticed in the hybrid polarimetric decompositions of RISAT-1 data. An overview of m - χ and m - α decompositions suggest dominant volume scattering in near range and dominant double bounce scattering in far range, whereas m - δ suggests dominant surface scattering in the entire image. However, upon a closer look, it could be observed that even bounce scattering is regular in the entire output whereas volume scattering gradually becomes more dominant as we move from near range to far range. The double bounce scattering in this case could be due the shorter wavelength of C-band RISAT-1 hybrid polarized waves. According to the roughness criteria given by Rayleigh and Peake and Oliver (Van Zyl & Kim, 2011), the threshold height above which a surface becomes rough is directly proportional to the wavelength the EM wave and inversely proportional to the sine of the incidence angle. If we compare the incidence angles of the UAVSAR cropped scene and RISAT-1 scene, they are almost the same (Table 6 and Figure 4). Therefore, C band RISAT-1 waves would be more susceptible to double bounce scattering as compared to L-band UAVSAR data. This might have been the reason for higher double bounce scattering in the RISAT-1 dataset.

As stated earlier, there are two types of dark patches depicted in the datasets, first, caused due to damping of capillary waves due oil spills and secondly, the shadow areas due to the presence of regular high sea surface waves in the oil spill region. The second is also a look alike feature (especially in rough sea conditions) which is not often reported in literature. This research goes on to carefully analyse and differentiate this look alike feature from true oil spills.

Oil spill detection

This research goes on to use the polarimetric information the quadpol, dualpol and hybrid-pol datasets to detect oil spills. In order to detect oil spills from the scenes, a modified version of Extended Polarimetric Feature Space (EPFS), a contextual and polarimetric segmentation method suggested by Doulgeris (2013) and Doulgeris & Eltoft (2010) and used for oil spill segmentation by Espeseth et al. (2017) was used. The modification was in the last stage of the algorithm where a majority smoothing operator was used instead of an MRF based contextual smoothing operator used by Doulgeris & Eltoft (2010). The polarimetric features of all datasets were spatially averaged using a 9×9 window size, similar to what was also done for UAVSAR data in Minchew et al. (2012) and contrary to a 60×15 (azimuth * range) window size in Espeseth et al. (2017). This averaging was performed in order to improve the contrast between the open water and slick areas. The normally distributed polarimetric features used for the segmentation were carefully chosen using the Shapiro-Wilk test of normality (Table 9 and Figure 14). The polarimetric features λ_3 and PD (Table 7) proved to be the most suitable features for UAVSAR data segmentation. For RISAT-1 dataset, DoP and H (Table 8) were the most suitable features. VV-intensity, geometric intensity and determinant of 2×2 covariance matrix proved to be the most useful features for TerraSAR-X dataset.

The input number of classes (n) was one the most fundamental parameters of the algorithm. Two values of n were tried: $n \in \{2, 3\}$. It was observed that choosing n as 3 improved the performance of the algorithm in distinguishing oil slicks from water and from shadow areas created due to high sea surface gravity waves. At this stage, the advantage of incidence angle normalization in improving oil spill detection was demonstrated (Figure 15). A sine based incidence angle normalization was useful in reducing the number of oil-spill false alarms in the far range. The final output shows the segmented oil slicks for all the three datasets. It can be seen that the algorithm with the same input parameters doesn't function as well for RISAT-1 and TerraSAR-X datasets as it does for the UAVSAR dataset. Larger window size for the smoothing operator and lower values for the tolerance of the Expectation Maximization of Gaussian Mixture Model were chosen, resulting in little improvement in the performance of the algorithm. Therefore, only the UAVSAR dataset was used for the slick analysis, feature comparison, and slick classification.

Comparison of Features

The effect of wind, which blew from the top right of the MLC UAVSAR image (Figure 8) to the bottom left (Table 5), was studied. This analysis showed that mineral oils were more susceptible to move in the direction of wind as opposed to natural biogenic films (PO, in this research). Moreover, it was interesting to notice that the movement of mineral oils which was proportional to the concentration of crude oil in the slicks. This result was in agreement with the hypothesis given in a review by Alpers et al. (2017).

The log-transformed feature values of the UAVSAR dataset were used in the comparison of features. Moreover, no spatial averaging was performed over the features in this case. The slick areas were then used for the comparison of features, which would, in turn, help in the choice of algorithms for oil spill classification. The measure for this comparison was chosen to be Jeffries-Matusita (JM) distance, a class separability measure. The motivation for this choice was that the features were normally distributed after log-transformation and that the same measure was used by Espeseth et al. (2017) for feature comparison. It was inferred from Figure 19 that PO was easier to separate from water regions as compared to mineral oils. It was also deduced that the oil slicks were easier to separate from water rather than from amongst themselves.

Moreover, the variation of JM distance with respect to the window size of the spatial averaging window was analysed. The analysis showed that the separabilities were higher in case of smaller averaging window sizes. This result suggests that over smoothing causes a reduction in the distinguishability of slicks. The variation inside the slicks may be useful in the characterization of oil spills. Therefore, speckle may indeed be useful in oil spill classification. Another important takeaway from this analysis was that the determinant of the covariance matrix showed highest separability between oil slicks and water and in some cases, between oil slicks themselves.

Image Classification

Owing to the fact that the $\det(C3)$ showed best class separability between oil-slicks and water, it was chosen as a basis for choosing the probabilistic classification algorithm. Supervised Gaussian based MLC and Wishart based MLC were chosen for the classification. The training data was designed so as to include the variability of the classes within the training set (Figure 9). The features were spatially averaged using a window size of 9×9 . Wishart-MLC classification showed much better results as compared to Gaussian-MLC classification (Figure 21). The Wishart MLC showed absolutely no misclassification in the near range and fewer misclassifications in the far range as compared to Gaussian-MLC. Therefore, the oil probability result from Wishart-MLC classification was chosen for modelling probability surfaces.

Probability Surface Modelling

After classification of oils from water, the result was decided to be used to model oil spills as 2-D Gaussian surfaces which were able to capture the spatial location, their orientation in space and the probability of oil in the slick of interest. The choice of the data used for this modelling and the idea was inspired from (Ardila, 2012), who used Normalized difference vegetation index (NDVI) and membership values from fuzzy classification methods to model Gaussian surfaces to find tree crown boundaries. A spatial averaging of the oil probability result was performed with varying window sizes (Table 14). The spatial averaging reduced the local minima of the oil-probability values or reduced its counts in the confined areas of the slicks. These confined areas were chosen from the oil spill areas delineated using EPFS segmentation. It was interesting to note that for no spatial averaging or for smaller window sizes, the modelled surfaces were small in size (Figure 24 (a), (b), and (c)). This may have been due to the presence of a large number of very low oil spill probability pixels within the confined slick ROI's. which would have resulted in low values of the major and minor axis of the elliptical Gaussian surface. For larger windows, the local maxima decreases, and the local minima either increases or its count decreases. This resulted in the probability values being distributed over an entire slick regions. In this case the modelled oil probability surfaces, show a larger spread as seen in Figures 24 (d), (e), and (f). Moreover, the modelled oil slick surfaces were also correctly oriented in the direction of wind.

The oil slicks showed different peak probabilities, with PO showing maximum probability value for higher window sizes (eg: 31×31). This was expected because the mineral oil emulsions would have started to dissolve over the course of approximately 6 hours. The dissolution would have been more in case of mineral oils slicks as compared to PO because of the presence of water in the emulsions and also because wind would have caused more areal surface interaction with the sea surface water, and thereby increasing the chances of dissolution. These Gaussian models were also able to predict higher probability (peak) oil in E60 as compared to E40. However, the models weren't able to predict higher oil probability for E80 which

actually comprised of 80% crude oil. It would be very interesting to see the application of this algorithm on other datasets of the same sensor and other datasets with different bands of acquisition.

Final remarks

During the course of this research, we have seen the utility of SAR polarimetry in segmenting, analysing the slicks, and classification of slicks using Wishart based MLC classifications. The eventual output of the research was the probability surface map (Figure 24). The performance of this probability surface modelling could not be tested on RISAT-1 and TerraSAR-X datasets. This could certainly be tried out to test the efficiency of the algorithm.

7. CONCLUSION AND RECOMMENDATIONS

The main objective of this research was to detect and characterize oils using multi-polarimetric information from PolSAR datasets. The datasets used for this research were quad-polarized airborne UAVSAR dataset, hybrid-polarized space-borne RISAT-1 dataset and dual-polarized TerraSAR-X dataset. The study area was North, Sea, Norway, where an oil spill exercise, called NORSE-2015 was conducted on 10th June, 2015. We developed methodologies for feature extraction, oil spill detection, feature comparison, image categorization, and probability surface generation. Suitable features were chosen for oil spill detection. The detected regions were used to analyse the slicks, and select appropriate features for oil spill classification. Depending upon the selected features, an appropriate classification algorithm was chosen for the classification. The classified output is then used for modelling the oil slicks as 2 dimensional Gaussian surfaces.

This research showed that the covariance matrix of the quad-polarized UAVSAR data has the potential to differentiate oil slicks from water as well as distinguish between different types of oil slicks. Supervised Wishart-MLC and Gaussian-MLC algorithms were chosen and their results were compared. According to the comparison between the classifiers, Wishart classification outperformed Gaussian based MLC classification. The segmented output and Wishart-MLC oil probability output was used to fit 2-D Gaussian surfaces to the probability values.

Response to Research Objectives and Research Questions

In response to the research objectives and research questions raised in Chapter 1, specific answers were drawn from the research. The first objective was dedicated to a review of literature related to oil spill detection and characterization. A comprehensive review has been reported in Chapter 2 of this document. This chapter specifically describes the polarimetric features (Section 2.4.3) and data segmentation and classification methods (Section 2.4.4) useful for oil spill detection and characterisation. Moreover, the major limitation of using SAR for oil spill categorization was found out to be similarity of information returned from both natural and biogenic slicks, which makes it difficult to characterize oil slicks. The second objective of this research was to detect oil spills in SAR images. A method called expectation maximization of Gaussian Mixture models was used for this purpose. The method describes the criteria for the use of features in the algorithm, as features to be normally distributed and its test as Shapiro-Wilk test of normality (Section 4.5). The results of this analysis (Section 5.4) suggest that the smallest eigenvalue of the coherency matrix and co-polarization NCRS difference were the best features for UAVSAR quad-pol dataset. However, the choice of the features is dependent on their data distribution. The third objective was to analyse the polarimetric features values using the extracted oil spill areas and compare the oil slicks with water areas. The slicks were compared on the basis of their shape, areal extent, and their respective feature values (Section 4.6 and 5.5). Moreover, the polarimetric features were compared on the basis of their potential to distinguish oil spills from water and also amongst themselves. Jeffreies-Matusita distance was found to be the most suitable method for feature comparison. Out of all features, the determinant of covariance matrix ($det(C3)$) was found to be the most suitable feature for separating oils slicks. The fourth objective of this research was to characterize oil spills. This was done using Wishart classification, which is a covariance matrix based classification method (Section 4.7 and 5.6). This method was concluded to be the most suitable algorithm because $det(C3)$ was the most useful features to distinguish various oil classes. The methodology and results of modelling probability surfaces to the oil slicks are mentioned in Sections 4.8 and 5.7 respectively.

Novelty

This research is novel with respect to the following 3 reasons: 1) discovery of radar shadows as false oil spill look-alikes, 2) analysis of trends in movement of oil spills with respect to the wind velocity, and 3) by modelling oil spills as probability surfaces. These points are elaborated in the next three paragraphs.

The shadows resulting from the radar wave interaction with high sea-surface waves act as false look-alikes for wind speed range 10-12 m/s. From Figures 10 and 11, it is clear that shadows which form in the regions of troughs of high sea surface gravity waves, appear as clear dark streaks in SAR images. The influence of such features on oil spill characterization is even more in cases where the wind velocities are high. However, they can be easy to make out in most cases through the naked eye, but may certainly cause confusion with oil spills if the slicks are of same or smaller shape than the average area of the shadow features. In this research these features became the primary reason to cause false oil spill detections. In Figure 15, the slicks were segmented from water and also from these periodically occurring high sea surface wave shadows.

Out of the 4 oil slicks in the datasets, the mineral oils showed more susceptibility to move in the direction of winds. It was observed from Table 13, that the extent of slicks in the direction of wind, which remained almost constant throughout the course of the exercise (Jones et al., 2016), was proportional to the concentration of crude oil in the mineral oil emulsions. This dataset is suitable for drawing this conclusion because, this dataset was acquired approximately 6 hours after the spillage of oils in the sea. The slicks might have had enough time to develop over the sea water.

From the results of probability surface models, it can be concluded that concentrated PO could be separated from mineral oil emulsions on the basis of oil probability in high wind conditions. Therefore, very dark appearing spills may have a higher chance of being plant oils or natural biogenic slicks rather than being emulsions of mineral oil, given that fact that both slicks have been in water for the same time period.

Practical Applicability of the Research

The aim of this work was to contribute to the wider scope research done in the direction of reducing the environmental impacts due to anthropogenic activities. Oil spills occur constantly and cause huge environmental and economic losses. For quick mitigation of adverse ramifications due to oil spills, it is important to know the location of the spill and also have the knowledge about the physical and chemical nature of the oil spill. The methods developed in this research could be useful in the gaining information about both the above stated aspects. Specifically, the maps generated using probability surface models could be very useful for organizations such as coast guard, maritime environmental organizations involved in detecting, containing or clearing oil spills. It would also allow agencies to focus on areas with higher chances of oil spill using the probability maps. The advantage of this method is that it can work in areas with high wind velocities, where detection of oil becomes difficult due to high sea surface gravity waves. Also, the processing speed of oil spill characterization is very fast. Appendix-C highlights the architecture of the oil spill detection tool which is currently under development. However, there would be certain modifications required in the method before it becomes operational. For example, the method needs to take into account that slicks with very high probabilities may be plant oils and hence reduce their probability of mineral oil.

UAVSAR, or in future, drones carrying SAR sensors could be good choices of sensor for gathering data for oil spill identification in an area where an initial alarm has been raised by the concerned ship crew. Moreover, in future, drones could regularly inspect areas which are more vulnerable to oil spill events such as

shipping lanes, oil rig positions and near harbours, where the chances of oil tanker collisions are very high. This could be the future of oil spill monitoring.

Recommendations:

The efficiency of the developed oil spill and characterization algorithm could be tested on other SAR datasets and the variation in the probabilities estimated by the probabilistic model could be used to assess the mixing of oil with water.

MRF based soft classification methods can also be used to classify oil-slicks. The probability of true oil spill detection from SAR data is affected by multiple factors, such as wind speed range, presence of algae in the region, proximity to shipping routes and oil rigs and shape of the slick. These effects are usually represented in a set of different hard classified maps. As an alternative, the factors stated above can be captured by modelling of oil spills as probability surfaces. The data presented in Chapter 3 of this research could be very useful for this purpose.

Future researches should include an in-depth analysis of uncertainty in classification and probability surface modelling into account.

LIST OF REFERENCES

- Alpers, W., Holt, B., & Zeng, K. (2017). Oil spill detection by imaging radars: Challenges and pitfalls. *Remote Sensing of Environment*, 201, 133–147. <https://doi.org/10.1016/j.rse.2017.09.002>
- Alpers, W., & Huhnerfuss, H. (1989). The Damping of Ocean Waves by Surface Films: A New Look at an Old Problem. *Journal of Geophysical Research*, 94(C5), 6251–6265. <https://doi.org/10.1029/JC094iC05p06251>
- Alpers, W., Zhang, B., Mouche, A., Zeng, K., & Wai, P. (2016). Rain footprints on C-band synthetic aperture radar images of the ocean - Revisited. *Remote Sensing of Environment*, 187, 169–185. <https://doi.org/10.1016/j.rse.2016.10.015>
- Ardila, J. P. (2012). *Object-based methods for mapping and monitoring of urban trees with multitemporal image analysis*. Faculty of Geoinformation Science and Earth Observation (ITC), University of Twente. Retrieved from http://www.itc.nl/library/papers_2012/phd/ardila.pdf
- Ardila, J. P., Tolpekin, V. A., Bijker, W., & Stein, A. (2011). Markov-random-field-based super-resolution mapping for identification of urban trees in VHR images. *ISPRS Journal of Photogrammetry and Remote Sensing*, 66(6), 762–775. <https://doi.org/10.1016/j.isprsjprs.2011.08.002>
- Ardila, J. P., Tolpekin, V., & Bijker, W. (2010). Angular backscatter variation in L-band ALOS ScanSAR images of tropical forest areas. *IEEE Geoscience and Remote Sensing Letters*, 7(4), 821–825. <https://doi.org/10.1109/LGRS.2010.2048411>
- Beyer, J., Trannum, H. C., Bakke, T., Hodson, P. V., & Collier, T. K. (2016). Environmental effects of the Deepwater Horizon oil spill: A review. *Marine Pollution Bulletin*, 110(1), 28–51. <https://doi.org/10.1016/j.marpolbul.2016.06.027>
- Bishop, C. M. (2006). *Pattern Recognition and Machine Learning*. (M. Jordan, J. Kleinberg, & B. Scholkopf, Eds.), Springer. Cambridge: Springer.
- Brebbia, C. A. (2001). *Oil spill modelling and processes*. Southampton, UK; Boston: WIT Press. Retrieved from <http://www.worldcat.org/title/oil-spill-modelling-and-processes/oclc/48212085>
- Brekke, C., Jones, C. E., Skrunes, S., Holt, B., Espeseth, M., & Eltoft, T. (2016). Cross-Correlation between Polarization Channels in SAR Imagery over Oceanographic Features. *IEEE Geoscience and Remote Sensing Letters*, 13(7), 997–1001. <https://doi.org/10.1109/LGRS.2016.2558543>
- Brekke, C., & Solberg, A. H. S. (2005). Oil spill detection by satellite remote sensing. *Remote Sensing of Environment*, 95(1), 1–13. <https://doi.org/10.1016/j.rse.2004.11.015>
- Bulgarelli, B., & Djavidnia, S. (2012). On MODIS Retrieval of Oil Spill Spectral Properties in the Marine Environment. *IEEE Geoscience and Remote Sensing Letters*, 9(3), 398–402. <https://doi.org/10.1109/LGRS.2011.2169647>
- Chang, S. E., Stone, J., Demes, K., & Piscitelli, M. (2014). Consequences of oil spills: a review and framework for informing planning. *Ecology and Society*, 19(2). <https://doi.org/10.5751/ES-06406-190226>
- Charbonneau, F. J., Brisco, B., Raney, R. K., McNairn, H., Liu, C., Vachon, P. W., ... Geldsetzer, T. (2010). Compact polarimetry overview and applications assessment. *Canadian Journal of Remote Sensing*, 36(sup2), S298–S315. <https://doi.org/10.5589/m10-062>

- Clemente-Colón, P. (2004). Chapter 9. Upwelling. In C. R. Jackson & J. R. Apel (Eds.), *Synthetic Aperture Radar Marine User's Manual* (pp. 221–244). Washington D.C.: U.S. Department of Commerce, National Oceanic and Atmospheric Administration.
- Cloude, S. R., Goodenough, D. G., & Chen, H. (2012). Compact Decomposition Theory. *International Geoscience and Remote Sensing Symposium (IGARSS)*, 9(1), 5097–5100. <https://doi.org/10.1109/IGARSS.2012.6352464>
- CNN. (2010). Oil Disaster by the numbers. Retrieved June 1, 2017, from <http://edition.cnn.com/SPECIALS/2010/gulf.coast.oil.spill/interactive/numbers.interactive/index.html>
- Dell'Amore, C. (2015, April 18). Why Did “Shocking” Amounts of BP Oil Fall to the Seafloor? Retrieved August 9, 2017, from <http://news.nationalgeographic.com/2015/04/150418-gulf-oil-spill-sea-snot-oceans-environment-energy-deepwater-bp/>
- Doulgeris, A. P. (2013). A Simple And Extendable Segmentation Method For Multi-Polarisation SAR Images. In *Proc. POLINSAR, Frascati, Italy*.
- Doulgeris, A. P., & Eltoft, T. (2010). Scale mixture of Gaussian modelling of polarimetric SAR data. *Eurasip Journal on Advances in Signal Processing*, 2010. <https://doi.org/10.1155/2010/874592>
- Espedal, H. A. (1999). Satellite SAR oil spill detection using wind history information. *International Journal of Remote Sensing*, 20(1), 49–65. <https://doi.org/10.1080/014311699213596>
- Espeseth, M. M., Skrunes, S., Brekke, C., Salberg, A.-B., Jones, C. E., & Holt, B. (2016). Oil spill characterization in the hybrid polarity SAR domain using log-cumulants. In *Proc. of SPIE* (Vol. 10004, p. 1000414(1-19)). <https://doi.org/10.1117/12.2241098>
- Espeseth, M. M., Skrunes, S., Jones, C. E., Brekke, C., Holt, B., & Doulgeris, A. P. (2017). Analysis of Evolving Oil Spills in Full-Polarimetric and Hybrid-Polarity SAR. *IEEE Transactions On Geoscience and Remote Sensing*, 55(7), 4190–4210. <https://doi.org/10.1109/TGRS.2017.2690001>
- Exxon Mobil. (2018a). Oseberg Blend - crude oil. Retrieved March 5, 2018, from <http://corporate.exxonmobil.com/en/company/worldwide-operations/crude-oils/oseberg-blend>
- Exxon Mobil. (2018b). Troll Blend - crude oil. Retrieved March 5, 2018, from <http://corporate.exxonmobil.com/en/company/worldwide-operations/crude-oils/troll-blend>
- Fingas, M., & Brown, C. (2014). Review of oil spill remote sensing. *Marine Pollution Bulletin*, 83(1), 9–23. <https://doi.org/10.1016/j.marpolbul.2014.03.059>
- Fore, A., Chapman, B. D., Hawkins, B. P., Hensley, S., Jones, C. E., Michel, T. R., & Muellerschoen, R. J. (2015). UAVSAR Polarimetric Calibration. *IEEE Transactions on Geoscience and Remote Sensing*, 53(6), 3481–3491. <https://doi.org/10.1109/TGRS.2014.2377637>
- Freeman, A., & Durden, S. L. (1998). A three-component scattering model for polarimetric SAR data. *IEEE Transactions on Geoscience and Remote Sensing*, 36(3), 963–973. <https://doi.org/10.1109/36.673687>
- Gade, M., Alpers, W., Hühnerfuss, H., Masuko, H., & Kobayashi, T. (1998). Imaging of biogenic and anthropogenic ocean surface films by the multifrequency/multipolarization SIR-C/X-SAR. *Journal of Geophysical Research: Oceans*, 103(C9), 18851–18866. <https://doi.org/10.1029/97JC01915>
- Gade, M., Alpers, W., Hühnerfuss, H., Wismann, V. R., & Lange, P. A. (1998). On the reduction of the radar backscatter by oceanic surface films: Scatterometer measurements and their theoretical interpretation. *Remote Sensing of Environment*, 66(1), 52–70. [https://doi.org/10.1016/S0034-4257\(98\)00034-0](https://doi.org/10.1016/S0034-4257(98)00034-0)

- Gens, R. (2008). Oceanographic Applications of SAR Remote Sensing. *GIScience & Remote Sensing*, 45(3), 275–305. <https://doi.org/10.2747/1548-1603.45.3.275>
- Goodman, J. W. (1976). Some fundamental properties of speckle. *Journal of the Optical Society of America*, 66(11), 1145. <https://doi.org/10.1364/JOSA.66.001145>
- Haralick, R. M., Shanmugam, K., & Dinstein, I. (1973). Textural Features for Image Classification. *IEEE Transactions on Systems, Man, and Cybernetics*, SMC-3(6), 610–621. <https://doi.org/10.1109/TSMC.1973.4309314>
- Harvey, E. H. (1925). The Surface Tension of Crude Oils. *Industrial & Engineering Chemistry*, 17(1), 85–85. <https://doi.org/10.1021/ie50181a042>
- Hunter, J. D. (2007). Matplotlib: A 2D Graphics Environment. *Computing in Science & Engineering*, 9(3), 90–95. <https://doi.org/10.1109/MCSE.2007.55>
- Infoterra GmbH. (2008). *Radiometric Calibration of TerraSAR-X Data. TerraSAR-X Services*.
- Jenkins, A. D., & Dysthe, K. B. (1997). The effective film viscosity coefficients of a thin floating fluid layer. *Journal of Fluid Mechanics*, 344, 335–337. <https://doi.org/10.1017/S0022112097006125>
- Jenkins, A. D., & Jacobs, S. J. (1998). Wave damping by a thin layer of viscous fluid. *Physics of Fluids*, 9(5), 1256. <https://doi.org/10.1063/1.869240>
- Jones, C. E., Dagestad, K.-F., Breivik, Ø., Holt, B., Rohrs, J., Christensen, K. H., ... Skrunes, S. (2016). Measurement and modeling of oil slick transport, 7759–7775. <https://doi.org/10.1002/2016JC012113>
- Kanevsky, M. B. (2009). *Radar Imaging of the Ocean Waves* (1st ed.). Oxford: Elsevier.
- Kudryavtsev, V. N., Chapron, B., Myasoedov, A. G., Collard, F., & Johannessen, J. A. (2013). On Dual Co-Polarized SAR Measurements of the Ocean Surface. *IEEE Geoscience and Remote Sensing Letters*, 10(4), 761–765. <https://doi.org/10.1109/LGRS.2012.2222341>
- Kumar, S., Kattamuri, H. P., & Agarwal, S. (2016). Dark spot detection for characterization of marine surface slicks using PolSAR remote sensing. In *Proc. of SPIE* (Vol. 9878, p. 98780K1-17). <https://doi.org/10.1117/12.2224415>
- Landau, L. D., & Lifshitz, E. M. (1987). *Fluid mechanics: Course of theoretical physics. Pergamon Books Ltd* (2nd ed., Vol. 6). <https://doi.org/10.1007/b138775>
- Lee, J.-S., & Pottier, E. (2009). *Polarimetric Radar Imaging: From Basics to Applications*. (B. J. Thompson, Ed.), CRC Press. Boca Raton, FL, USA.
- Liu, P., Zhao, C., Li, X., He, M., & Pichel, W. (2010). Identification of ocean oil spills in SAR imagery based on fuzzy logic algorithm. *International Journal of Remote Sensing*, 31(17–18), 4819–4833. <https://doi.org/10.1080/01431161.2010.485147>
- Longuet-Higgins, M. S. (1963). The generation of capillary waves by steep gravity waves. *Journal of Fluid Mechanics*, 16(1), 138. <https://doi.org/10.1017/S0022112063000641>
- Lopez, L., & Moctezuma, M. (2005). Oil spill detection using GLCM and MRF. In *Geoscience and Remote Sensing Symposium, 2005. IGARSS '05. Proceedings. 2005 IEEE International* (pp. 1781–1784). <https://doi.org/10.1109/IGARSS.2005.1526349>

- Migliaccio, M., Ferrara, G., Gambardella, A., Nunziata, F., & Sorrentino, A. (2007). A physically consistent speckle model for marine SLC SAR images. *IEEE Journal of Oceanic Engineering*, 32(4), 839–847. <https://doi.org/10.1109/JOE.2007.903985>
- Migliaccio, M., Gambardella, A., & Tranfaglia, M. (2007). SAR Polarimetry to Observe Oil Spills. *IEEE Transactions on Geoscience and Remote Sensing*, 45(2), 506–511. <https://doi.org/10.1109/TGRS.2006.888097>
- Migliaccio, M., Nunziata, F., & Gambardella, A. (2009). On the co-polarized phase difference for oil spill observation. *International Journal of Remote Sensing*, 30(6), 1587–1602. <https://doi.org/10.1080/01431160802520741>
- Minchew, B. (2012). Determining the mixing of oil and sea water using polarimetric synthetic aperture radar. *Geophysical Research Letters*, 39(16), 1–6. <https://doi.org/10.1029/2012GL052304>
- Minchew, B., Jones, C. E., & Holt, B. (2012). Polarimetric Analysis of Backscatter From the Deepwater Horizon Oil Spill Using L-Band Synthetic Aperture Radar. *IEEE Transactions on Geoscience and Remote Sensing*, 50(10), 3812–3830. <https://doi.org/10.1109/TGRS.2012.2185804>
- Mladenova, I., Jackson, T. J., Bindlish, R., & Hensley, S. (2013). Incidence Angle Normalization of Backscatter Data. *IEEE Transactions on Geoscience and Remote Sensing*, 51(3), 1791–1804.
- Moctezuma, M., Parmiggiani, F., & Lopez, L. (2014). Measuring marine oil spill extent by Markov Random Fields. In *Proc. of SPIE* (Vol. 9240, p. 92400A1-6). <https://doi.org/10.1117/12.2068325>
- Morales, D. I., Moctezuma, M., & Parmiggiani, F. (2008). Detection of oil slicks in SAR images using hierarchical MRF. *International Geoscience and Remote Sensing Symposium (IGARSS)*, 3(1), 1390–1393. <https://doi.org/10.1109/IGARSS.2008.4779620>
- NASA. (2015). Publications and presentations - UAVSAR. Retrieved November 21, 2017, from <https://uavsar.jpl.nasa.gov/science/publications>
- Oliphant, T. E., & E., T. (2007). Python for Scientific Computing. *Computing in Science & Engineering*, 9(3), 10–20. <https://doi.org/10.1109/MCSE.2007.58>
- Pedregosa, F., Varoquaux, G., Gramfort, A., Michel, V., Thirion, B., Grisel, O., ... Duchesnay, E. (2011). Scikit-learn: Machine Learning in Python. *Journal of Machine Learning Research*, 12, 2825–2830.
- Phillips, O. M. (1957). On the generation of waves by turbulent wind. *Journal of Fluid Mechanics*, 2(5), 417. <https://doi.org/10.1017/S0022112057000233>
- Pinel, N., & Bourlier, C. (2009). Unpolarized Infrared Emissivity Of Oil Films On Sea Surfaces. In *IEEE International Geoscience and Remote Sensing Symposium 2(2)* (pp. 1185–1188). <https://doi.org/10.1109/IGARSS.2009.5418007>
- Raney, R. K. (2007). Hybrid-Polarity SAR Architecture. *International Geoscience and Remote Sensing Symposium (IGARSS)*, 45(11), 2229–2231. <https://doi.org/10.1109/IGARSS.2007.4423282>
- Salberg, A. B., Rudjord, Ø., & Solberg, A. H. S. (2014). Oil spill detection in hybrid-polarimetric SAR images. *IEEE Transactions on Geoscience and Remote Sensing*, 52(10), 6521–6533. <https://doi.org/10.1109/TGRS.2013.2297193>
- Shapiro, S. S., & Wilk, M. B. (1965). An Analysis of Variance Test for Normality (Complete Samples). *Biometrika*, 52(3/4), 591–611. <https://doi.org/10.2307/2333709>

- Skrunes, S., Brekke, C., & Doulgeris, A. P. (2015). Characterization of low-backscatter ocean features in dual-copolarization SAR using log-cumulants. *IEEE Geoscience and Remote Sensing Letters*, 12(4), 836–840. <https://doi.org/10.1109/LGRS.2014.2363688>
- Skrunes, S., Brekke, C., & Eltoft, T. (2014). Characterization of Marine Surface Slicks by Radarsat-2 Multipolarization Features. *IEEE Transactions on Geoscience and Remote Sensing*, 52(9), 5302–5319. <https://doi.org/10.1109/TGRS.2013.2287916>
- Skrunes, S., Brekke, C., Jones, C. E., & Holt, B. (2016). A Multisensor Comparison of Experimental Oil Spills in Polarimetric SAR for High Wind Conditions. *IEEE Journal of Selected Topics in Applied Earth Observations and Remote Sensing*, 9(11), 4948–4961. <https://doi.org/10.1109/JSTARS.2016.2565063>
- Tolpekin, V. A., & Stein, A. (2009). Quantification of the effects of land-cover-class spectral separability on the accuracy of markov-random-field-based superresolution mapping. *IEEE Transactions on Geoscience and Remote Sensing*, 47(9), 3283–3297. <https://doi.org/10.1109/TGRS.2009.2019126>
- Tomar, K. S. (2015). *Hybrid Polarimetric decomposition for Aboveground Biomass Estimation using semi-empirical modeling*. Faculty of Geoinformation Science and Earth Observation (ITC), University of Twente.
- Valenzuela, G. R. (1978). Theories for the interaction of electromagnetic and oceanic waves – a review. *Boundary Layer Meteorology*, 13, 61–85.
- Van Zyl, J., & Kim, Y. (2011). *Synthetic Aperture Radar Polarimetry* (1st ed.). New Jersey: Wiley. <https://doi.org/10.1002/9781118116104>
- Wang, D., Pan, D., Zhan, Y., & Zhu, Q. (2010). Experiment of monitoring oil spill on the base of EOS/MODIS data. In *SPIE – Int. Soc. Opt. Eng.* (Vol. 7831, p. 78311T). <https://doi.org/10.1117/12.864967>
- Weber, H. R. (2010). Blown-out BP well finally killed at bottom of Gulf. Retrieved June 1, 2017, from http://archive.boston.com/news/nation/articles/2010/09/19/blown_out_bp_well_finally_killed_at_bottom_of_gulf/
- Wright, J. (1966). Backscattering from capillary waves with application to sea clutter. *IEEE Transactions on Antennas and Propagation*, 14(6), 749–754. <https://doi.org/10.1109/TAP.1966.1138799>
- Wu, Y., Ji, K., Yu, W., & Su, Y. (2008). Region-Based Classification of Polarimetric SAR Images Using Wishart MRF. *IEEE Geoscience and Remote Sensing Letters*, 5(4), 668–672. <https://doi.org/10.1109/LGRS.2008.2002263>

APPENDIX-A

Expectation Maximization of Gaussian Mixture Models

A univariate Gaussian distribution can be defined as follows

$$\mathcal{N}(x|\mu, \sigma) = \frac{1}{\sqrt{2\pi}\sigma} \exp\left(\frac{-(x-\mu)^2}{2\sigma^2}\right) \quad (1)$$

where, x is a vector of data points, μ and σ are the mean and variance of the data distribution. Similarly, a multivariate Gaussian distribution can be defined by the following equation.

$$\mathcal{N}(x|\mu, \Sigma) = \frac{1}{\sqrt{2\pi}|\Sigma|} \exp\left(\frac{-1}{2}(x-\mu)^T \Sigma^{-1}(x-\mu)\right) \quad (2)$$

where, Σ is the covariance matrix of between the variables.

Gaussian Mixture Models

In order to estimate the parameters of the multi-variate data distribution, we can use maximum likelihood estimation. A Gaussian mixture distribution can be represented as a linear superposition of Gaussians, as described in the following equation:

$$p(\mathbf{x}) = \sum_{k=1}^K \pi_k \mathcal{N}(x|\mu_k, \Sigma_k) \quad (3)$$

Where K represents the number of Gaussians, and π_k is the mixing coefficient which defines the weight of each Gaussian in the mixture model. There are two constraints of positivity and normalization imposed on the mixing coefficients:

$$0 \leq \pi_k \leq 1, \quad \sum_{k=1}^K \pi_k = 1 \quad (4)$$

Considering the log-likelihood (Eq. 5), maximum likelihood cannot be used to calculate the parameters, because there is no close form solution.

$$\ln p(X|\mu, \Sigma, \pi) = \ln(p(x_n)) = \sum_{n=1}^K \ln \left\{ \sum_{k=1}^K \pi_k \mathcal{N}(x|\mu_k, \Sigma_k) \right\} \quad (5)$$

Therefore, the parameters are calculated using Expectation Maximization (EM) technique.

The latent variable or the posterior probability can be calculated by considering the mixing coefficients as prior probabilities. Therefore, for a given value of x , the corresponding posterior probabilities (also called responsibilities) can be calculated using the Bayes rule:

$$y_k(x) = p(k|x) = \frac{p(k)p(x|k)}{p(x)} = \frac{\pi_k \mathcal{N}(x|\mu_k, \Sigma_k)}{\sum_{j=1}^K \pi_j \mathcal{N}(x|\mu_j, \Sigma_j)} \quad \text{where, } \pi_k = \frac{N_k}{N} \quad (6)$$

Where N_k and N are the number of data points of each

Expectation Maximization (EM)

In this step, for a given Gaussian mixture model, the goal is to maximize the likelihood function with respect to the parameters (μ , Σ and π_k). EM is an iterative optimization technique and comprises of two steps:

Expectation step: For a initialized set of parameter values, the expected values of the latent variable are computed (using Eq. 6), and the initial value of log likelihood is calculated (using Eq. 5).

Maximization step: The values of the model parameters are updated based on the values of the latent variable calculated in the expectation step, and hence the value of the log likelihood is calculated (using Eq. 5).

$$\mu_j = \frac{\sum_{n=1}^N \gamma_j(x_n) x_n}{\sum_{n=1}^N \gamma_j(x_n)} ; \Sigma_j = \frac{\sum_{n=1}^N \gamma_j(x_n) (x_n - \mu_j)(x_n - \mu_j)^T}{\sum_{n=1}^N \gamma_j(x_n)} ; \pi_j = \frac{1}{N} \sum_{n=1}^N \gamma_j(x_n) \quad (7)$$

Thereafter, the steps are repeated until a convergence is achieved.

APPENDIX-B

This appendix presents the multi-temporal UAVSAR data acquisitions and the results from the feature extraction processes mentioned in Section 4.4. The features from UAVSAR, RISAT-1 and TerraSAR-X dataset have also been presented. The reader is requested to zoom into the figures to see the details clearly.

1. UAVSAR Multi-temporal data acquisitions

The following figure presents the series of multiple SAR data acquisitions from UAVSAR (Figure B-1).

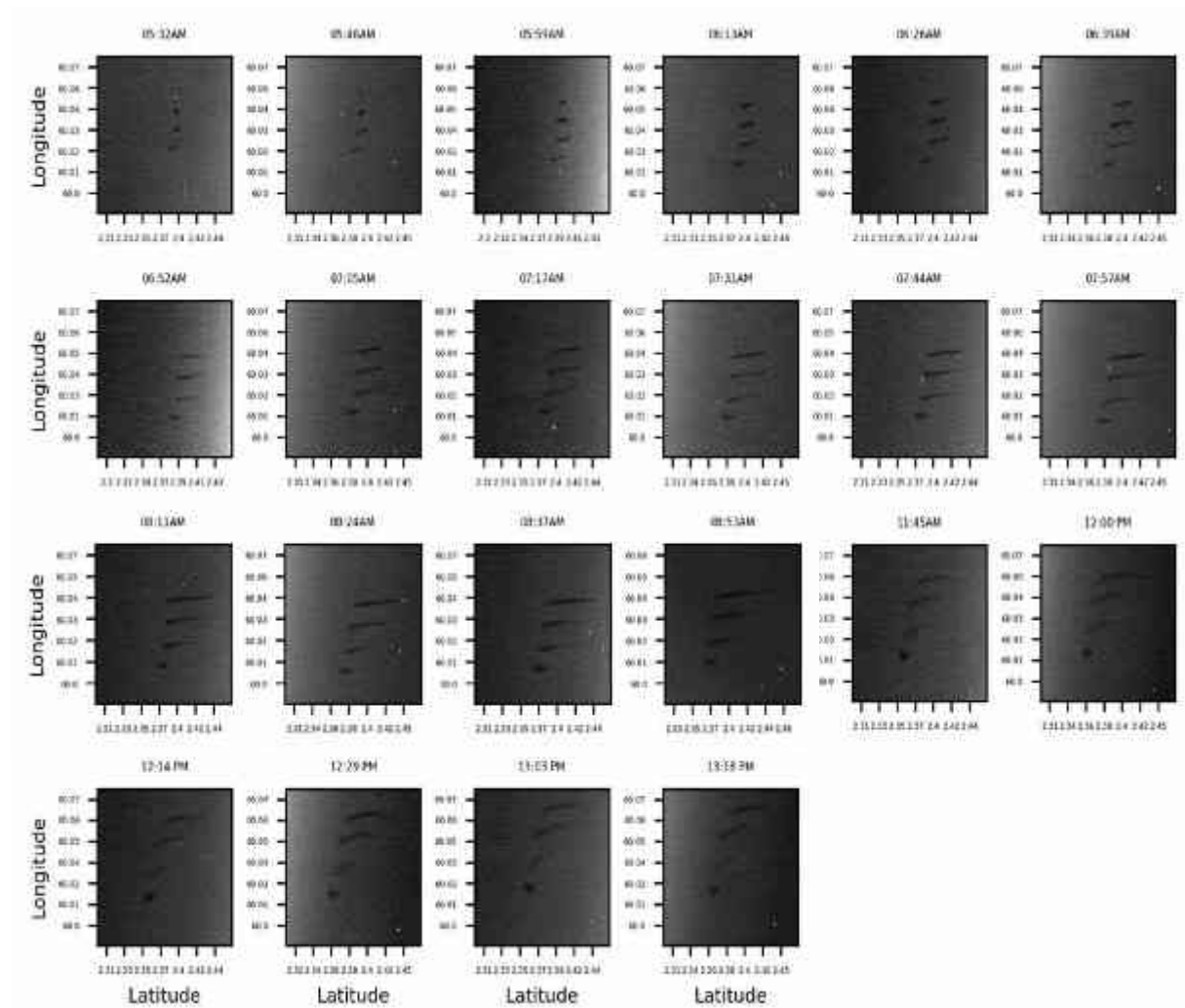


Figure B-1: Intensity VV plots of time series of UAVSAR data acquisitions during NORSE-2015. The time of acquisition is mentioned over the top of the each sub-plot.

2. Application of Image Segmentation on the time series of UAVSAR grd datasets

The oil slick detection methodology described in this work is implemented on UAVSAR grd datasets displayed above.

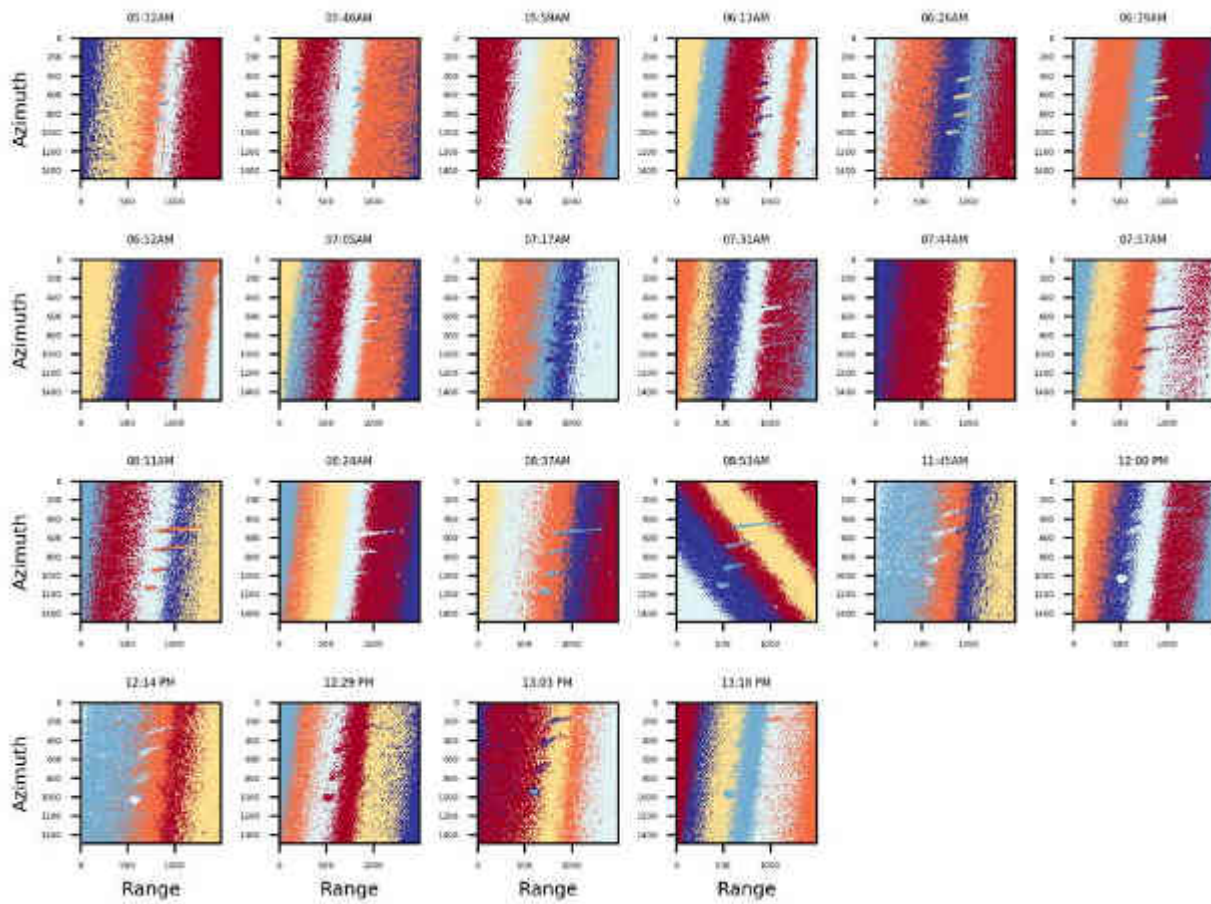


Figure B 2: Slick segmentation using EM of GMM using number of segments = 6.

2. UAVSAR Polarimetric Features

The following table describes all the polarimetric features which were left out from Table 7. Please refer to the 'List Of References' for finding the details of the reference cited in the following table.

Table B-1: Fully polarimetric features.

<u>Name</u>	<u>Formula</u>
Co-polarization power ratio (Minchew et al., 2012)	$\gamma_{CO} = \frac{\langle I_{VV} \rangle}{\langle I_{HH} \rangle}$
Standard deviation of co-polarized phase difference (Alpers et al., 2017)	$\phi_{CO} = \sqrt{\langle (\phi_{HH} - \phi_{VV})^2 \rangle + \langle (\phi_{HH} - \phi_{VV}) \rangle^2}$
Conformity Coefficient	$\mu_{FP} = \frac{2(\Re(\langle S_{HH} S_{VV}^* \rangle)) - \langle S_{HV} ^2 \rangle}{\langle S_{HH} ^2 \rangle + 2\langle S_{HV} ^2 \rangle + \langle S_{VV} ^2 \rangle}$
Co-polarization Coefficient	$\rho_{CO} = \frac{ S_{HH} S_{VV}^* }{\sqrt{\langle S_{HH} ^2 \rangle \langle S_{VV} ^2 \rangle}}$
Cross-pol ratio	$P_x = \frac{\langle S_{HV} ^2 \rangle}{\langle S_{HH} ^2 \rangle + \langle S_{VV} ^2 \rangle}$
Entropy (Skrunes et al., 2016)	$H = \sum_{i=1}^3 p_i \log_3 p_i; p_i = \frac{\lambda_i}{\sum_{i=1}^3 \lambda_i}$
Mean angle α of eigen vectors	$\langle \alpha \rangle = \sum_{i=1}^3 p_i \cos^{-1}(\mathbf{e}_i(1))$
Anisotropy	$A = \frac{\lambda_2 - \lambda_3}{\lambda_2 + \lambda_3}$
Polarization fraction	$PF = 1 - \frac{\lambda_3}{\lambda_1 + \lambda_2 + \lambda_3}$
Pedestal Height	$PH = \frac{\lambda_3}{\lambda_1}$

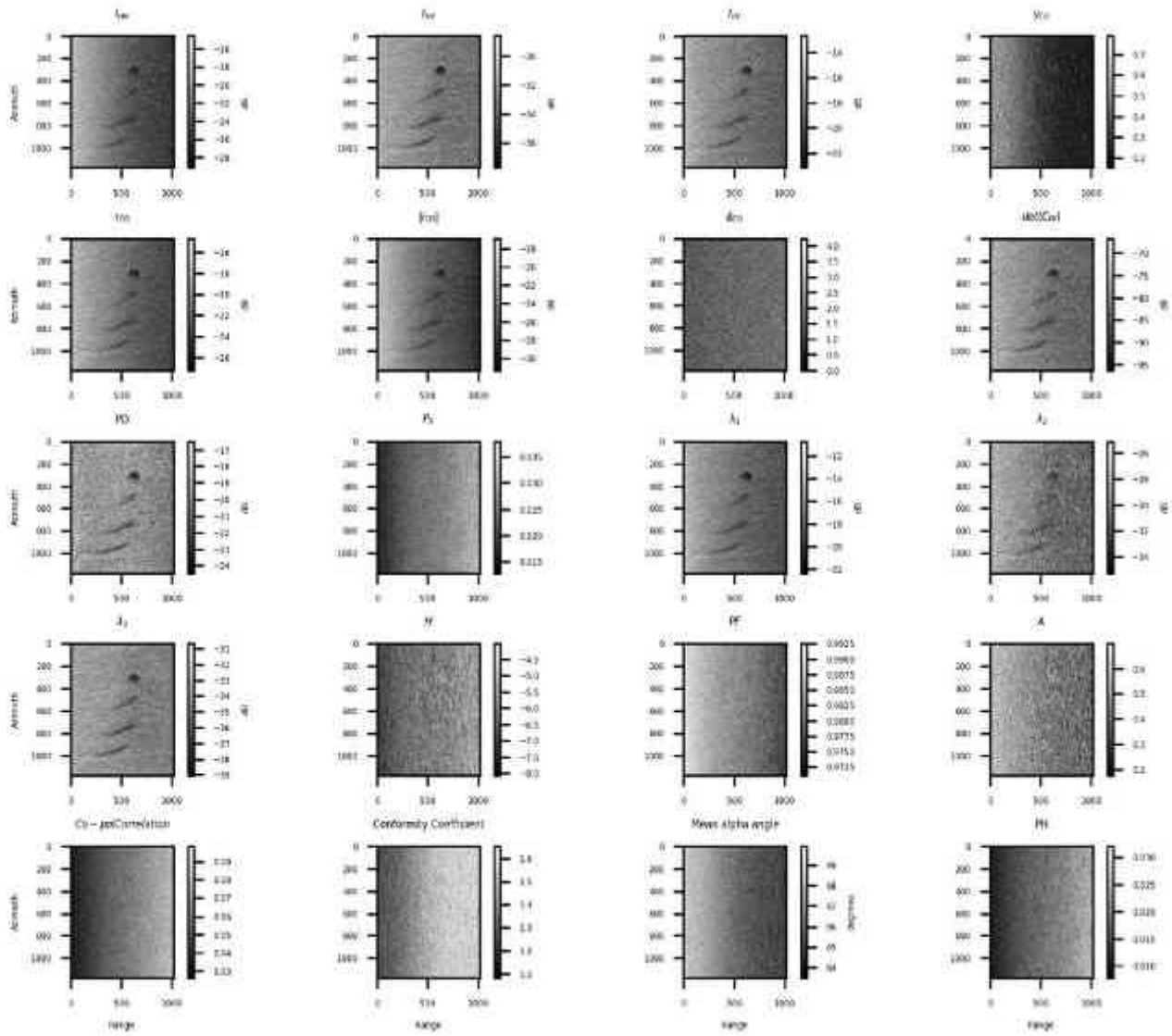


Figure B-3: Plots of most fully polarimetric features which have been cited in literature for useful oil spill detection. The name of the each feature is mentioned as the subtitle of each subplot.

2. TerraSAR-X Polarimetric Features

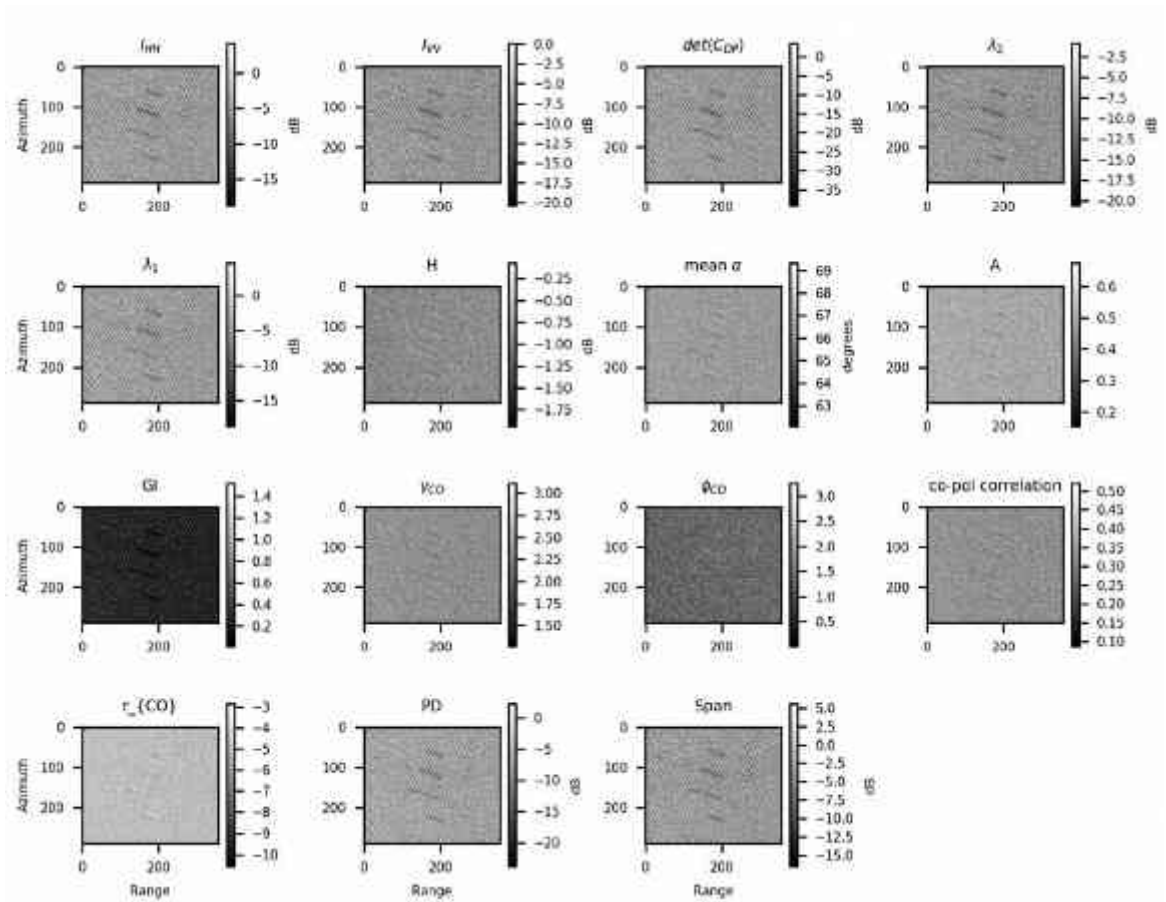


Figure B-4: TerraSAR-X dual polarimetric features. The name of each feature is mentioned on the top of each feature.

3. RISAT-1 Polarimetric Features

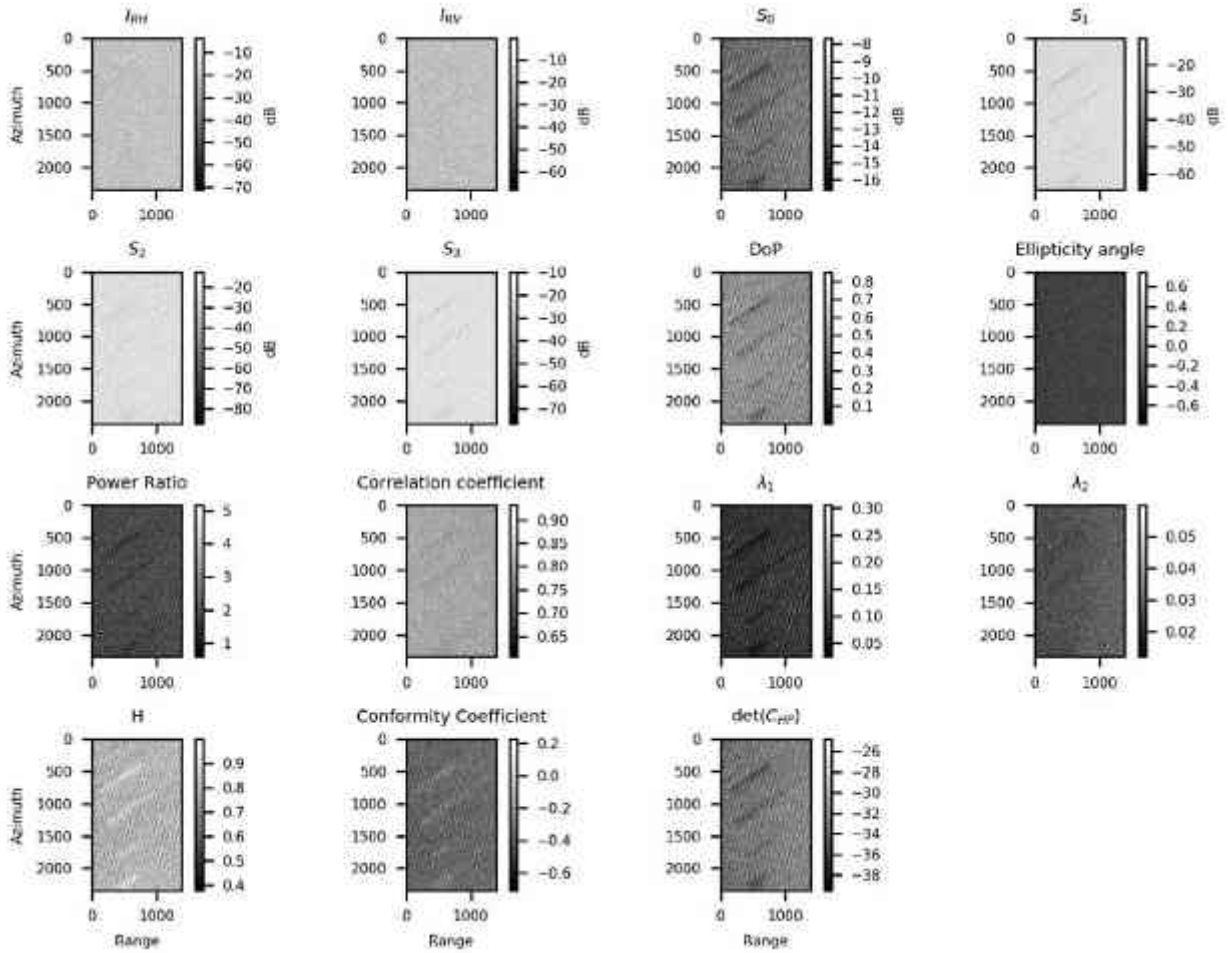


Figure B-5: RISAT-1 hybrid polarimetric features. The names are mentioned as titles of each subplot.

APPENDIX-C

A screenshot of an oil spill detection application which is currently under development and hopes to carry forward this research work.

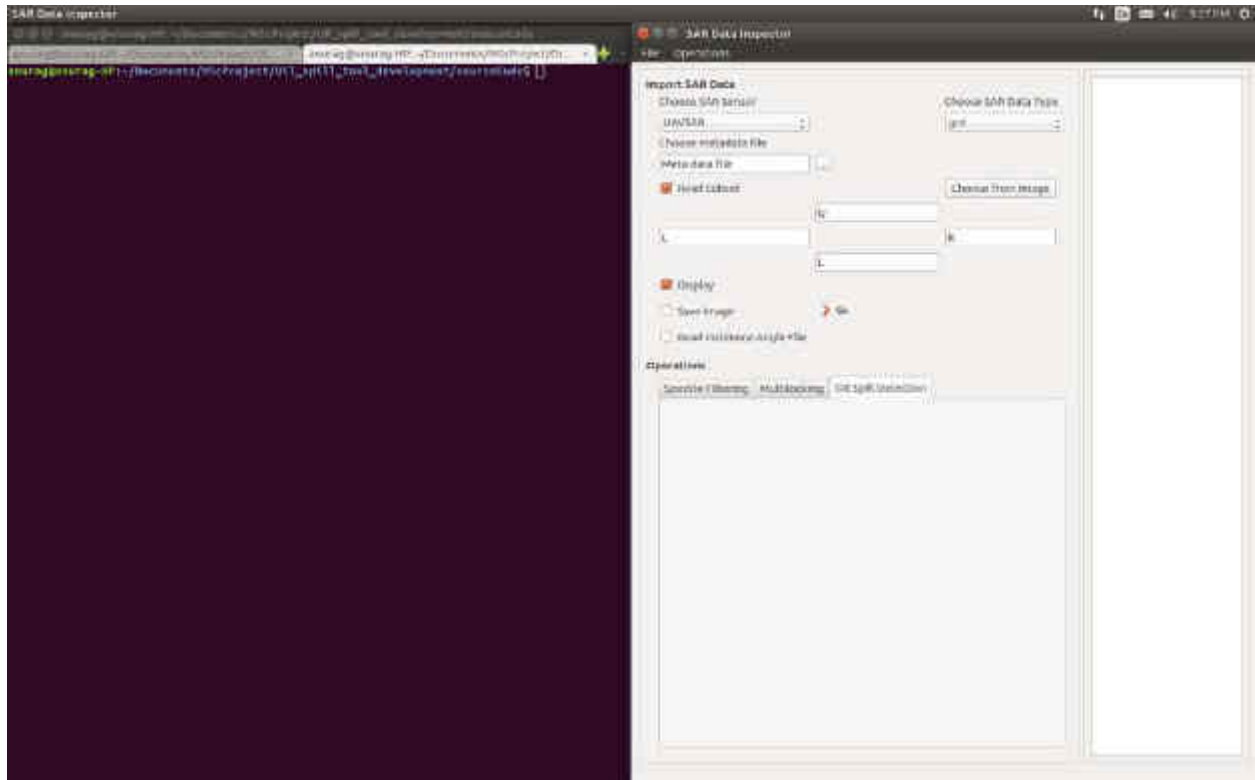


Figure C 1: SAR Data Inspector currently under development